Investigation of a Diagnostic Technique for Measuring Electron Densities via Stark Broadening on the Alcator C-Mod Tokamak

by

Dirk Lumma

Submitted to the Department of Physics
in partial fulfillment of the requirements for the degree of

Master of Science

at the

MASSACHUSETTS INSTITUTE OF TECHNOLOGY

February 1996

Author .....
Department of Physics
November 30, 1995

Certified by .....
Earl S. Marmar
Senior Research Scientist

Certified by .....
Miklos Porkolab
Professor
Thesis Reader

Accepted by .....
George F. Koster
Chairman, Departmental Committee on Graduate Studies

Investigation of a Diagnostic Technique for Measuring Electron Densities via Stark Broadening on the Alcator C-Mod Tokamak

by

Dirk Lumma

Submitted to the Department of Physics
on November 30, 1995, in partial fulfillment of the
requirements for the degree of
Master of Science

Abstract

The broadening of spectral emission lines by the Stark effect has been used to determine electron densities in deuterium plasma discharges on the Alcator C-Mod tokamak. Measurements have been made particularly in the divertor region where electron densities can reach values of the order $10^{21}\,\mathrm{m}^{-3}$. The optical system employed is a fast, multiple-channel spectrometer system for the visible spectrum, and the spectral lines used are high-n transitions in the Balmer series of deuterium.

The hardware configuration of the experiment is described, and both wavelength and intensity calibration are discussed in the appendix. Based on an outline of the underlying theory, the properties of the routine used for the numerical analysis of the spectra are specified. The different causes of measurement inaccuracies are discussed, leading to an estimate of the overall uncertainty.

The final chapter explores the correlations between the results obtained from the Stark broadening method and measurements made by other diagnostic techniques such as H_α tomography and interferometry. An emphasis is put on the combined use of Stark broadening analysis and H_α tomography, leading to the presentation of spatial electron density profiles for a MARFE phenomenon.

Thesis Supervisor: Earl S. Marmar
Title: Senior Research Scientist

Thesis Reader: Miklos Porkolab
Title: Professor

Acknowledgements

I wish to express my sincerest thanks to Bruce Lipschultz, Earl Marmar, and to Miklos Porkolab for giving me the opportunity and the privilege to work in the Alcator C-Mod research group. I would especially like to thank Bruce Lipschultz for his guidance and advice during my time at MIT.

I owe many thanks to Brian LaBombard, Garry McCracken, and Jim Terry for their comments and suggestions as well as for their encouragement which has made writing this thesis a lot easier. I am also very much indebted to Josh Stillerman, who took the time to explain the *grande finesse* of the database to me; he taught me the skills without which the data processing necessary for this thesis could not have been performed. I would like to thank all the members of the Alcator C-Mod group for creating an environment in which it has always been a pleasure to work.

I am grateful to my teachers at the Universität Hamburg, but especially to Dr. R. Blatt, Dr. E. Bönecke, Professor Dr. R. Johnson, and Professor Dr. A. Lindner. Their support has made it possible for me to conduct my studies of Physics at MIT.

I have also been fortunate to be surrounded by an exceptional group of friends at both Harvard and MIT. Throughout the time of my researching and writing this thesis, they have continuously broadened my perspectives. I would like to mention Patrick Chung and Gabriele Migliorini, as well as Sohrab Ismail-Beigi, who took the burden of reading the first drafts of this thesis.

My gratitude to Katharina Drope is boundless. She not only delighted me with her daily correspondence, but also travelled to Spain with me during a time when rest and relaxation was needed most.

Of course, I owe a great deal to my mother for encouraging me to come to MIT, and for her understanding of my decision to leave Hamburg to study Physics in the United States, despite her missing me so much.

Contents

List of Figures

List of Tables

Chapter 1

Introduction

1.1 The Geometry of Alcator C-Mod

This introductory section is aimed at describing the geometric features and the overall parameters of the facility at which the spectroscopic measurements are performed. In addition, the topological terminology used in the later chapters of this thesis will be defined. This section relies substantially on Ref. [12].

A poloidal cross section of Alcator C-Mod is shown in Fig. 1-1; this figure is used to describe the spatial features of the tokamak vessel. The 'inner wall' (1) is the vertical section of the inner vessel boundary that is exposed to the plasma. The region near the bottom of the vessel with the numbered items from (2) to (7) is referred to as the 'lower divertor'. The region near (8), the 'upper divertor', has not been examined with the spectrometer system that will be described in chapter 2. For that reason, the term 'divertor' will always refer to the lower divertor within the context of this thesis. The solid line in Fig. 1-1 is called 'separatrix'. It describes the shape of the plasma boundary in a diverted plasma discharge. The point (7) at which the poloidal magnetic field vanishes will be referred to as 'X-point'. The intersections of the separatrix with the divertor surface are called 'strike points'. There is an 'inner strike point' near (2) and an 'outer strike point' near (6). The points (2) and (3) at the inner and outer divertor plate are the inner and outer 'divertor noses'. The divertor plate sections above the divertor noses will be referred to as the inner and

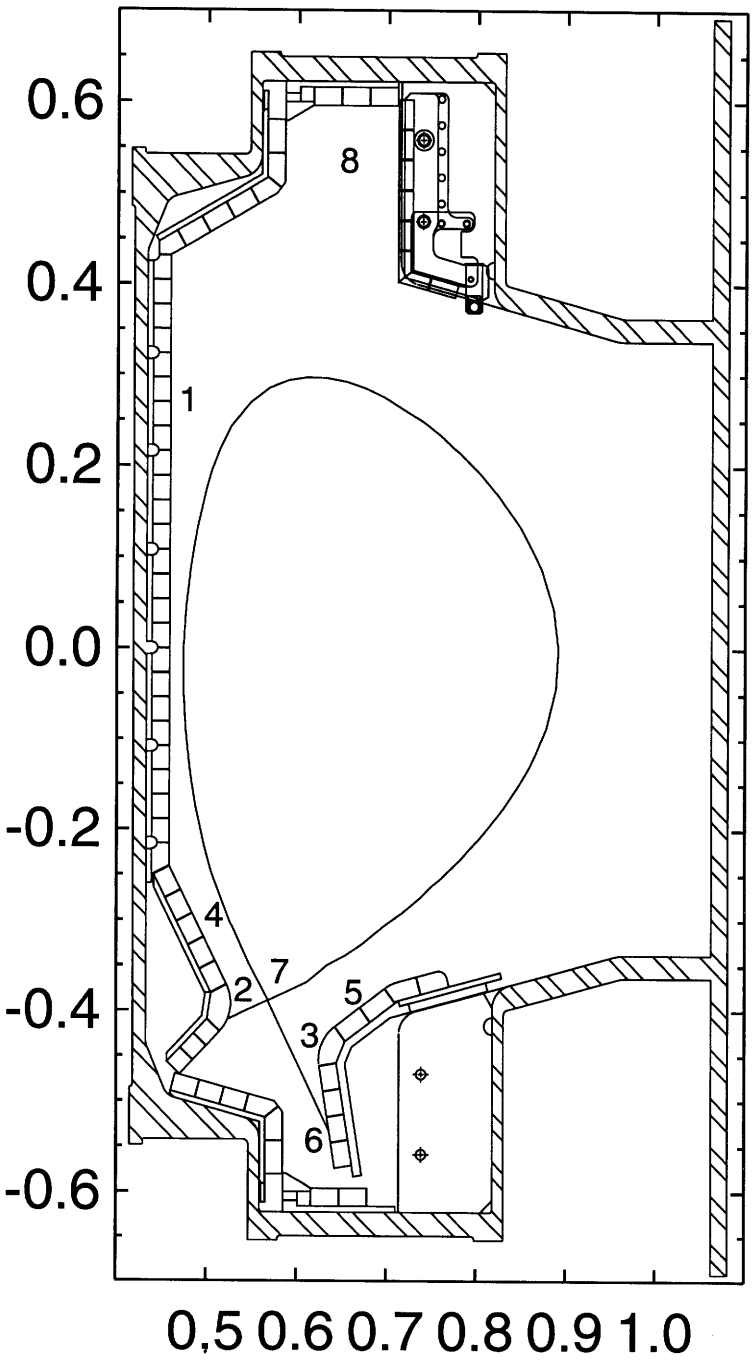

Figure 1-1: Poloidal cross section of Alcator C-Mod. 1: inner wall, 2: inner nose, 3: outer nose, 4: inner ledge, 5: outer ledge, 6: slot, 7: X-point, 8: upper divertor.

outer 'divertor ledges', i.e. (4) and (5). The region at the very bottom of the tokamak vessel, formed by the vertical target plates around (6), is called the 'divertor slot'.

Using the above definition of points within the tokamak and knowledge of the shape of the separatrix, we can distinguish between different plasma regions: the 'private flux region' is formed by the divertor surface and the separatrix connecting the two strike points with the X-point. The term 'common flux region' denotes the whole space not enclosed by the separatrix which does not belong to the private flux region.

The overall parameters of the tokamak are given in Table 1.1 from Ref. [12]. One sees that Alcator C-Mod is a high density tokamak with the capability of producing strongly shaped plasmas.

Parameter	achieved (design)
major radius	0.67 m
minor radius	0.21 m
elongation	1.8 (1.8)
toroidal B-field	8.0 T (9 T)
plasma current	1.1 MA (3 MA)
core electron density	$10^{21}\mathrm{m}^{-3}$
core electron temp.	4 keV
RF power	3.5 MW (4 MW)

Table 1.1: Machine parameters of Alcator C-Mod.

1.2 The Divertor Concept

The term 'separatrix' introduced above denotes the last closed flux surface of the magnetic field. The operation of Alcator C-Mod as a divertor tokamak changes the magnetic geometry in such a way that this last closed field line is defined by a null in the poloidal field.

By using a divertor, the interaction between the hot core plasma and the limiter at the inner wall is reduced. The use of a divertor has two main advantages: tile erosion is minimized and the influx of impurities from the material surfaces into the core plasma is kept at a low level. A functioning divertor leads to a reduction of the

heat load on the limiter, while still allowing for a sensible density control over the plasma system.

In contrast, a 'limiter' configuration is based on a different arrangement of the magnetic field where the last closed flux surface is defined by the physical contact with a limiter attached to the vessel wall. Its main disadvantage with respect to the divertor is that impurities are more likely to enter the hot plasma core where they may lead to high radiation losses, thereby cooling the core plasma.

The 'connection length' is defined to be the length of an open magnetic field line between its two contact points with the material surfaces. By construction, a divertor increases the connection length. This allows for high temperature gradients parallel to the magnetic field, thus allowing one to have a low temperature in the divertor while maintaining a hot plasma upstream.

1.3 Thesis Goal

In order to derive other plasma parameters, detailed knowledge of N_e and T_e, the plasma electron density and temperature, is required. In this thesis, an attempt will be made to examine whether a fast multi-channel spectrometer system, here called the '*Chromex* spectrometer system', is an appropriate tool for measuring the electron density N_e of the plasma.

It will be questioned whether the electron density can be calculated solely on the basis of spectroscopic measurements. Such an investigation will have to rely on the existence of a correlation with results from other diagnostic instruments. The spectroscopic system is set up to take measurements within the divertor region of the tokamak vessel.

Typical spectra used for the calculation of electron densities are presented in Figures 1-2 and 1-3. Figure 1-2 shows a spectrum observed with a chord viewing the inner divertor, whereas Fig. 1-3 presents data from the outer divertor. Both spectra exhibit the same deuterium transitions in the Balmer series, starting with transition 2–7 at 396.90 nm. The series members beyond the transition 2–11 cannot be clearly

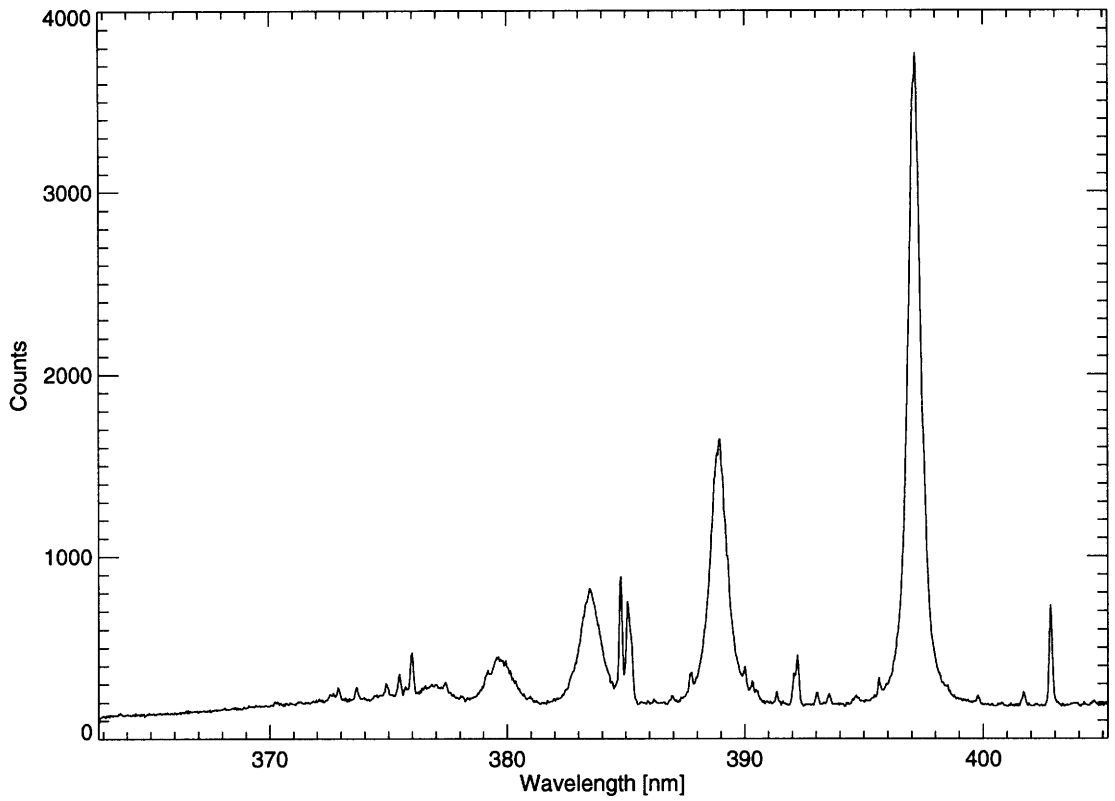

Figure 1-2: A typical spectrum of the high-n Balmer transitions of deuterium, observed with the chord K_{bottom} 12 in the time frame [1.087 s, 1.132s] of discharge 950426025.

identified anymore, an effect which is due to two physical phenomena: the merging of lines close to the *Inglis-Teller limit* and the low intensity of high-n transitions.

The deuterium lines shown have a width which is much larger than the width of the instrumental profile, the Doppler width, or the Zeeman splitting. This strong broadening is caused by the *Stark effect* whose underlying theory allows one to calculate the electron density N_e at the point of the emission, based on the corrected Lorentzian width of the spectral profile describing the deuterium transition. Corrections will be included for all the physical effects mentioned.

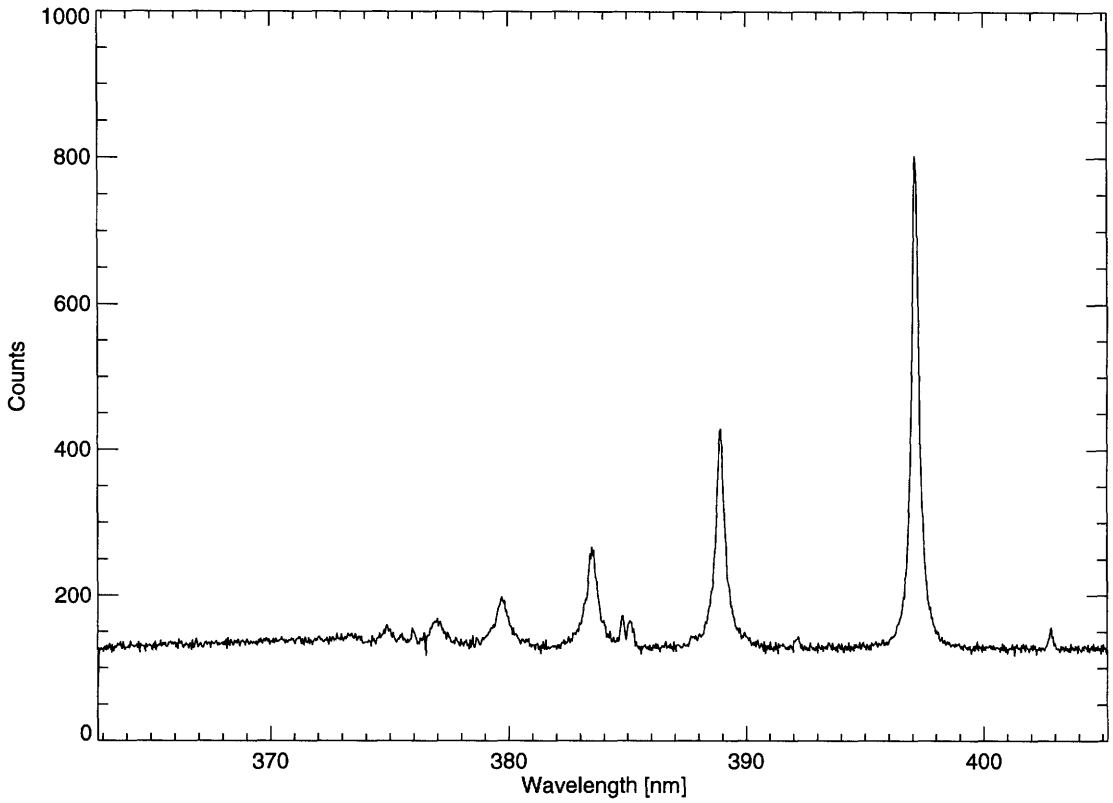

Figure 1-3: A typical spectrum of the high-n Balmer transitions of deuterium, observed with the chord A_{bottom} 18 in the time frame [1.087 s, 1.132s] of discharge 950426025.

The method to calculate the electron density is based on the analysis of only a single transition. In principle, each of the four transitions 2–7, ..., 2–10 could be used separately to calculate an electron density. The results for the electron densities obtained from analyzing different transitions will be compared with each other. Since there are impurity lines present in the spectrum, not all transitions are equally well suited for the electron density calculation. The effect of impurity lines on the measurement will be discussed.

The two spectra presented show the signal on different chords for the same time frame of a specific discharge. Comparing them shows that the Balmer line *intensities* observed on the outer divertor chords are smaller than those on the inner divertor chords by more than a factor of five. It is also apparent that the presence of impurities is reduced in the outer divertor spectrum.

The fact that the lines in the outer divertor spectrum 1-3 have a smaller width

than the lines seen on the inner divertor spectrum 1-2 indicates that the electron density at the spatial location which mainly contributes to the radiation observed with the outer divertor fiber is smaller than the electron density at the corresponding location for the inner divertor fiber. In general, it is a non-trivial task to find the poloidal location whose radiation dominates the input of a specific fiber. For this purpose, the use of H_α tomography will be discussed.

Chapter 2

Experimental Apparatus

2.1 The Apparatus

The *Chromex* spectrometer system was designed to provide visible spectra of the divertor region with high light throughput and high time resolution. The apparatus of the *Chromex* spectrometer system will be described below. The theory of the detector operation will be explained. The fundamental optical features of the spectrograph itself will be outlined as well as the construction of the periscope fiber bundle together with the views of the different periscopes. The hardware characteristics mentioned in this chapter are extracted from Refs. [4, 5, 19].

2.2 The Detector

The device used for the conversion of the incoming photon flux into a count rate is a CCD detector. The acronym 'CCD' stands for 'Charge Coupled Device'. Within one CCD pixel, photons are transduced to electrons, the current is integrated over an effective exposure time, and the result is stored. From there, the data are read and converted into a digital signal.

One observes a thermally induced buildup of charge in CCD pixels. This statistical phenomenon is termed the 'dark charge'. In order to reduce it, the CCD detector is cooled to $-25°$ Celsius. At the operating range of a CCD detector, the dark charge

is reduced by a factor of ~ 2 for every temperature reduction by 7° K. Due to the existence of the dark charge, the 'background count rate' due to the dark charge must be subtracted from every count rate measurement in an experiment.

The detector used for the system to be discussed has 1242x1152 CCD pixels. The 1242 pixels per row are parallel to the spectrally resolving dimension of the instrument, whereas the 1152 pixels per column allow spatial resolution of the signal.

2.2.1 Frame Transfer

The detector is optically and electronically divided into a lower and an upper frame of 576 rows with 1242 pixels each. The lower half of the detector plane is covered so that the count rate of those pixels cannot be increased by radiation influx. The upper half lies in the exit plane of the spectrograph.

The two detector sections are connected via a vertical shift mechanism which allows the system to shift the upper half image into the lower one within 576 shifting steps. Each step is a parallel motion which shifts all pixels in the full image one row downwards. The pixels in the uppermost row of the moving image are set to zero as the charge is shifted downwards. Because the two half frames have separate shifting clocks, the upper half can be exposed to radiation influx without being shifted while the lower half can be read and digitized.

The readout is a combination of parallel row shifts and sequential pixel shifts. The rows of the lower half can be shifted in parallel into a register row. From there, the individual pixels of that register row can be shifted sequentially into a single register. The value of that register can either be discarded or digitized. So after 576 parallel row shifts and 1242 sequential pixel shifts for each row, the whole frame is read out. The overall data acquisition cycle is given by the following chronological steps:

I The upper half of the detector frame is exposed while the lower part is read.

II The upper half is transferred into the lower half. This process results in a 'clear' upper half.

III The cycle starts again.

The advantage of this 'frame transfer mode' of the detector lies in its time economy: the exposure of the next frame and the readout of the previous one are done simultaneously, at the only cost of the time needed for the frame transfer. Since the row shift time is much smaller than the time needed for the digitization of one pixel row, the frame transfer technique is successful.

2.2.2 Hardware Binning

The detector is capable of binning pixels in both dimensions. A 'bin' is defined to be an area of pixels which are not digitized separately. Instead, the data corresponding to a group of pixels constituting the bin are first summed within the detector hardware, and the sum is then digitized. For our purposes, hardware binning in the wavelength direction is not used since that would lead to a loss of wavelength resolution.

On the contrary, binning in the spatial direction is desired since we have 14 independent optical fibers mapped onto the detector plane. The first 574 pixel rows of the image are divided into 14 spatial bin rows with a spatial width of 41 pixels each. The remaining two pixel rows of the detector are discarded. The considerations leading to the choice of this spatial bin width will be described later.

Electronically, the spatial binning is implemented by adding up the appropriate pixel rows to the register row during the parallel shifting process. Once all rows constituting a bin have been added, the register row, now containing the result of a sum over multiple pixel rows, is sequentially shifted and digitized. The discarding of a row is achieved by simply discarding all pixels of that row once they have been shifted into the single register.

The most significant slowing down effect for the entire acquisition process is the digitization. Since hardware binning reduces the number of digitizations needed considerably, it is a detector feature which improves the time resolution of the overall system.

2.2.3 Timing

Two analog to digital converters are implemented in the detector: a 12 Bit/1 MHz ADC and a 16 Bit/430 kHz ADC. Since a high dynamic range is desired, this entire thesis will only be dealing with the 16 Bit converter.

As described in the two sections above, there are a number of different time variables which contribute to the overall time scale of the detector performance:

- t_i: the row shift time.
- t_{sr}: the time needed to shift one pixel from the register row into the single register for discarding or digitization.
- t_v: the time needed by the ADC to convert the single register.
- t_s: the time needed to discard the single register.

Since we are discarding two pixel rows and binning solely in the spatial direction, the readout time $T_{readout}$ is given by:

$$T_{readout} = N_y\, t_i + \frac{N_y - N_{y,discard}}{Y_{group}}\, N_x\, [t_{sr} + t_v] + N_{y,discard}\, N_x\, [t_{sr} + t_s]\,. \qquad (2.1)$$

Here $N_x = 1242$ and $N_y = 576$ are the number of detector pixel columns and rows respectively. $N_{y,discard} = 2$ is the number of pixel rows to be discarded. $Y_{group} = 41$ is the width of the binned group along the spatial direction. The time $T_{transfer}$ for the whole frame transfer can be calculated from:

$$T_{transfer} = N_y\, t_i\,. \qquad (2.2)$$

In addition, the nominal exposure time $T_{exp,nom}$ can be set by the software. It is defined as the length of the time window during which a shutter would be open and

allow the detector to be exposed to light. (Since we are using a system that is capable of operating in frame transfer mode, we do not need a shutter.)

The upper half of the detector will be exposed to radiation influx for a time

$$T_{exp,eff} \equiv T_{transfer} + \min\left[T_{readout},\, T_{exp,nom}\right] \ . \tag{2.3}$$

$T_{exp,eff}$ is the effective exposure time relevant for the calculation of count rates. Since the upper detector half is also exposed to the radiation influx during the frame transfer process, the condition

$$T_{transfer} \ll T_{exp,eff} \tag{2.4}$$

must always be met. When this condition ceases to be true, the spatial information contained in the detector count rates will be smeared out.

Another parameter of the system is the vertical shift time which can also be set by the software. During discharge measurements, the minimum of $3\,\mu$s is always used in order to achieve the highest possible time resolution.

The time variables used in this chapter have been measured, using a high frequency memory oscilloscope, by analyzing TTL reference signals provided by the detector hardware. The frame transfer time $T_{transfer}$ can be read directly from a signal normally used for the shutter control. From $T_{transfer}$, the value of t_i can be calculated easily.

Time Variable	Value	Description of Process
t_i	3.04 μs	Vertical row shift.
$t_{sr} + t_v$	2.31 μs	Sequential shift and conversion.
$t_{sr} + t_s$	0.14 μs	Sequential shift and discarding.
$T_{transfer}$	1.75 ms	Frame transfer.
$T_{readout}$	42.26 ms	Readout.
$T_{exp,eff}$	44.01 ms	Effective exposure.

Table 2.1: Time variables measured for the 16 Bit ADC with 430 kHz. Hardware binning is set to 14 spatial bins with a width of 41 pixels each. 2 pixel rows are discarded. No binning in the wavelength direction. The vertical shift time is set to $3\,\mu$s.

From another TTL signal, the readout time $T_{readout}$ is measured for a number of different binning situations. This allows to set up a system of linear equations which can be solved. From the algebraic structure of equation 2.1 it is clear that the

independent variables t_{sr}, t_v, t_r always appear in pairs. Therefore, one can only solve for these combined variables. The results of the calculations are summarized in Table 2.1.

During the standard discharge measurements, the detector is set to the 'store enable mode': the detector is continuously taking frames. These frames are fully discarded unless the detector receives a trigger during the nominal exposure time. If such a trigger is received, the data are binned and digitized as explained above and sent to the acquisition computer. The trigger signal is provided starting from about 100 ms before the plasma discharge until the end of the discharge. The trigger is a 5 kHz TTL signal, thereby ensuring that during the discharge all subsequent frames are digitized and that the highest possible acquisition frequency is achieved.

Furthermore, the detector signal normally used for shutter control is digitized during the entire time window in which the trigger is provided. From this data, the start time of the first frame taken and the average effective exposure time are derived for each plasma discharge. This information is then used to calculate the count rates for the intensity calibration that will be described later.

2.3 The *Chromex* Spectrograph

The *Chromex* spectrograph has a focal length of $F = 250\,\mathrm{mm}$ and an aperture ratio $f/4$. In general, the f number of an optical instrument with axial symmetry is defined as

$$f \equiv \frac{F}{d}\,, \tag{2.5}$$

where d is the diameter of the entrance aperture as seen from focus. The *Chromex* spectrograph does not have axial symmetry, a fact which requires a generalization of equation 2.5. Using $\pi \left(\frac{d}{2}\right)^2 = A$, one obtains from substitution:

$$f \equiv \sqrt{\frac{\pi F^2}{4A}}\,, \tag{2.6}$$

with A denoting the area of the entrance aperture as seen from focus. In the specific case of the *Chromex* instrument, F denotes the distance between entrance slit and

mirror, and A denotes the area of the mirror covered by the light cone (see Fig. 2-1).

The light gathered by an optical instrument is dependent on the *étendue* $A\,\Omega$. Keeping the area A fixed, the light throughput is proportional to the solid angle

$$\Omega = \frac{A}{F^2} \propto \frac{1}{f^2}\,. \tag{2.7}$$

The $f/4$ aperture ratio was chosen as a specification of the *Chromex* spectrograph since a high light throughput is desired.

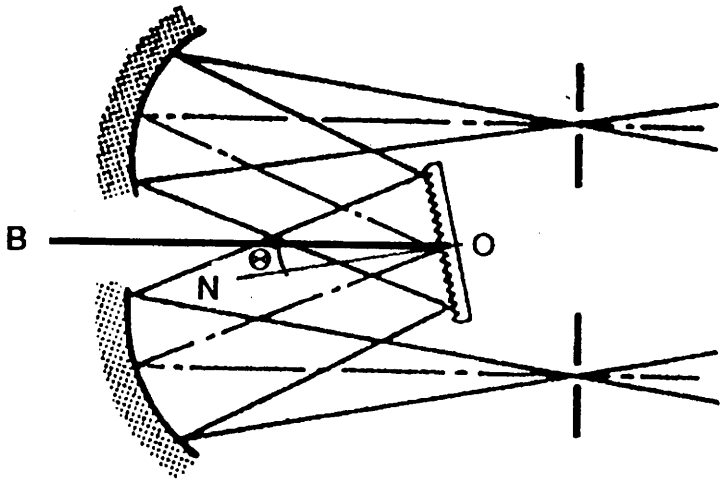

Figure 2-1: The asymmetrical Czerny-Turner configuration of the spectrograph.

The entrance slit is straight and bilaterally adjustable from $10\,\mu$m to 2 mm. It is computer controlled with a stepper-motor drive. The slit height is 9.8 mm. Three blazed gratings are selectable, each with a different number of grooves per unit length: $600\,\mathrm{mm}^{-1}$, $1200\,\mathrm{mm}^{-1}$, and $1800\,\mathrm{mm}^{-1}$. The blazing leads to a further improvement of the light throughput. The dispersion and wavelength resolution for these gratings will be discussed in the chapter regarding wavelength calibration.

The three [68 mm x 68 mm] gratings are mounted onto a turret within the spectrograph. Due to the fact that the turret carries three gratings, their motion is a combination of a rotation and a translation. The system has a manufacturer precalibration that reads the appropriate stepper-motor positions from an internal database for each setting of the spectrograph center wavelength $\lambda_{\mathrm{chromex}}$. This precalibration is specifically done for each individual instrument. The precalibration would be lost

if a grating were exchanged manually. Therefore, the gratings can only be exchanged automatically.

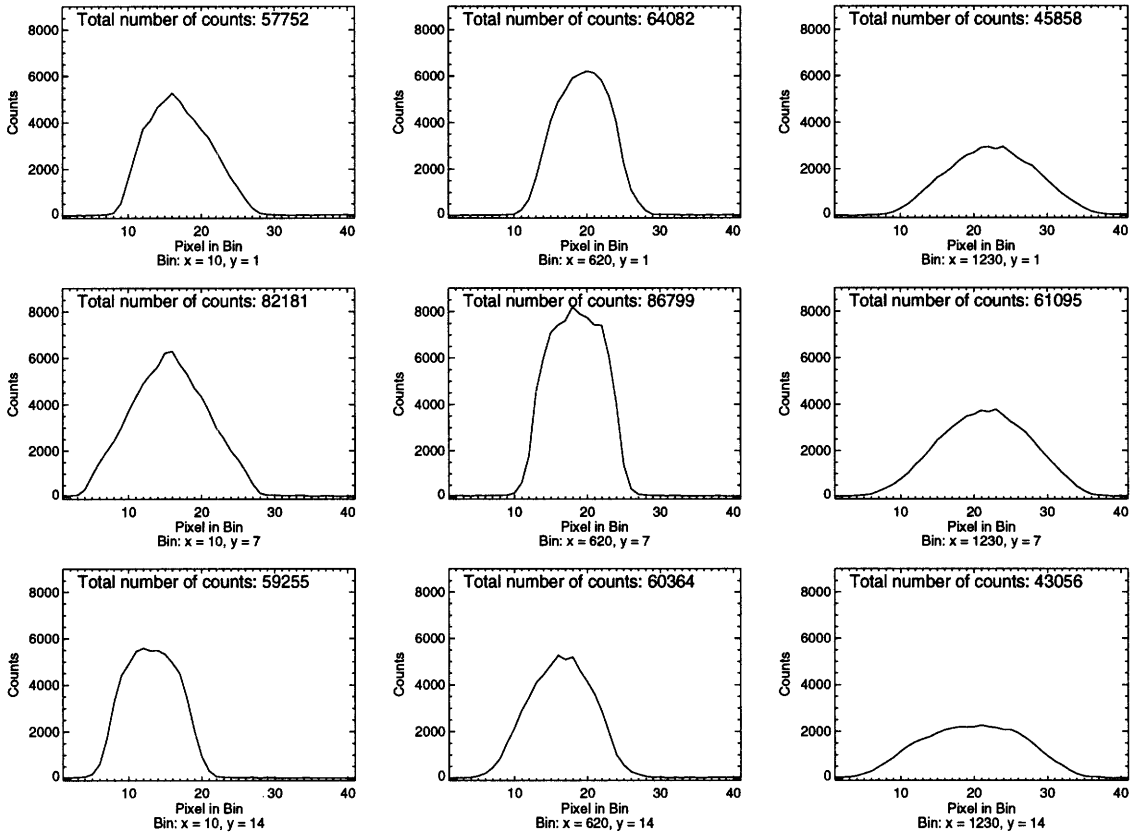

Figure 2-2: **The spatial line shape of a continuum light source on different positions of the detector plane. This detector exposure was taken with the $600\,\mathrm{mm}^{-1}$ grating and a spectrograph center wavelength set to $\lambda_{\mathrm{chromex}} = 800\,\mathrm{nm}$. The three detector bins $y \in \{1, 7, 14\}$ are exposed to the same light input from a halogen calibration source.**

The spectrograph center wavelength will be referred to as $\lambda_{\mathrm{chromex}}$ throughout this entire thesis. Although $\lambda_{\mathrm{chromex}}$ carries a physical meaning by means of the manufacturer precalibration, it will only be regarded as a hardware parameter. A new wavelength calibration will be performed relative to the manufacturer precalibration, treating $\lambda_{\mathrm{chromex}}$ as a variable.

A digital stepper-motor drive is used for the wavelength scanning. For the $1200\,\mathrm{mm}^{-1}$ grating, the wavelength accuracy is $\pm 0.15\,\mathrm{nm}$, precalibrated by the manufacturer. The wavelength repeatability precision can be improved to $\pm 0.05\,\mathrm{nm}$ by scanning to the selected wavelength from the same wavelength direction. The wavelength range lies between $180\,\mathrm{nm}$ and $10\,\mu\mathrm{m}$, but is dependent on the grating used.

The wavelength scanning as well as all other functions of the spectrograph are controlled via a serial connection RS232. This connection between the data acquisition computer and the tokamak cell is optically buffered.

The system is optically set up in an asymmetrical Czerny-Turner configuration shown in Fig. 2-1. The configuration consists of two mirrors and a grating. In the specific instrument used for this thesis, the exit slit is substituted by a detector plane. For the given instrument with a specific grating chosen, the Czerny-Turner configuration is uniquely defined by specifying the angle formed between the line normal to the grating and the line $\overline{OB}$ drawn in Fig. 2-1. The optical configuration is corrected for aberration effects. This feature is crucial for using a two-dimensional CCD detector as the exit plane. The correction is implemented by the use of toroidal mirrors.

Such an optical system transforms the image of a point source into an elongated vertical spot. The straight slit will then be transformed into the portion of a circle on the detector screen. This effect does not affect the wavelength resolution of the system, but it changes the absolute wavelength calibration as a function of the detector row, and it limits the spatial resolution of the system. The effect of the aberration on the absolute wavelength calibration of the instrument is discussed in the calibration appendix.

The instrument has a useful focal field area of [13 mm x 28 mm]. 14 optical fibers are focused onto the entrance slit and then mapped onto that focal field area through the optical system. The detector count rate as a function of pixel position is measured, using the $600\,\mathrm{mm}^{-1}$ grating, with the spectrograph center wavelength set to $\lambda_{\mathrm{chromex}} = 800\,\mathrm{nm}$. The center input fiber and the two outermost input fibers are illuminated by a continuum calibration light source, and all other inputs are kept dark. This configuration leads to three horizontal stripes on the detector plane.

Fig. 2-2 shows the spatial cross section of this continuum spectrum for nine different positions on the detector plane. The total count rate, the spatial width, and the spatial shape of these nine peaks are functions of detector position. None of these features can affect the wavelength calibration of the instrument. The fact that

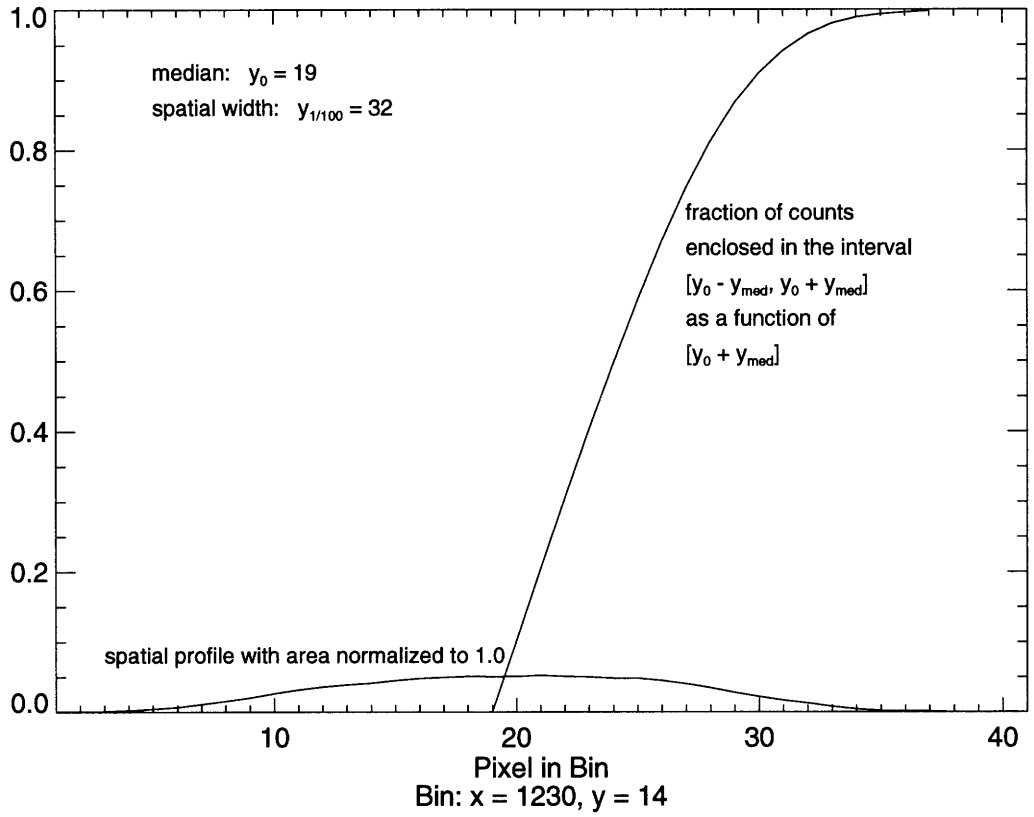

Figure 2-3: The spatial width and the percentage of the total area covered within that width.

the total count rate can be a function of the detector bin position will be taken into account within the intensity calibration by introducing a bin dependent sensitivity. The shape of a spatial line profile will not affect the intensity calibration if a spatial bin covers the whole spatial region which is affected by its corresponding input fiber. In order to make sure that this condition is met, the width of the spatial profile has to be calculated.

The calculation of the width of a spatial profile is illustrated in Fig. 2-3. For this calculation, the spatial profile shown in the right bottom corner of Fig. 2-2 is used since it has the largest width among all the nine profiles presented in that figure. This chosen profile is plotted again in Fig. 2-3, but there normalized to have unit area. The median y_0 of the normalized profile is calculated. As a function of distance y_{med} from this median, the area included within the interval $M = [y_0 - y_{med}, y_0 + y_{med}]$ is calculated as a function of y_{med}. This function $r(y_{med})$ is equal to the ratio of the

count rate contained in the interval M and the total count rate. The width $y_{1/100}$ of the spatial profile is then defined as

$$y_{1/100} \equiv 2 \cdot \min\{y_{med} | r(y_{med}) > 0.99\} \ . \tag{2.8}$$

The calculation for the chosen profile leads to a spatial width of $y_{1/100} = 32$ pixels.

The configuration of the instrument is intended to allow for absolute intensity measurements with inaccuracies smaller than 1%, thereby also necessitating that the interchannel crosstalk be less than 1%. Since the detector plane might be slightly rotated with respect to the slit image, a spatial width of 32 pixels will not be sufficient to reduce the interchannel crosstalk below 1%. The spatial bin width has been chosen to be 41 pixels, a choice which allows for 14 independent spatial bins on the detector plane.

2.4 The Periscope Fiber Bundle

This section will describe the mechanical construction of the optical fiber bundle which transmits the signals from the tokamak into the spectrometer system. In addition, the locations of the different optical inputs within the vessel will be specified for later reference in this thesis.

2.4.1 Construction of the Bundle

The optical fiber bundle is designed to provide the input for several optical instruments. For that reason, its input plane is a combination of three sets of optical fibers. The whole system is illustrated in Fig. 2-4.

The rectangular input plane of the bundle includes one set of fibers which is arranged as a two-dimensional array with the dimensions [10 mm x 8 mm]. Its fibers — made of glass and having a diameter of 10 μm each — are used to extract an optical image from inside the vessel. This array is split into two halves. Between the two, 40 optical quartz fibers with a diameter of 400 μm are arranged in two columns of 20 fibers each. One of these columns consists of fibers optimized for use in the

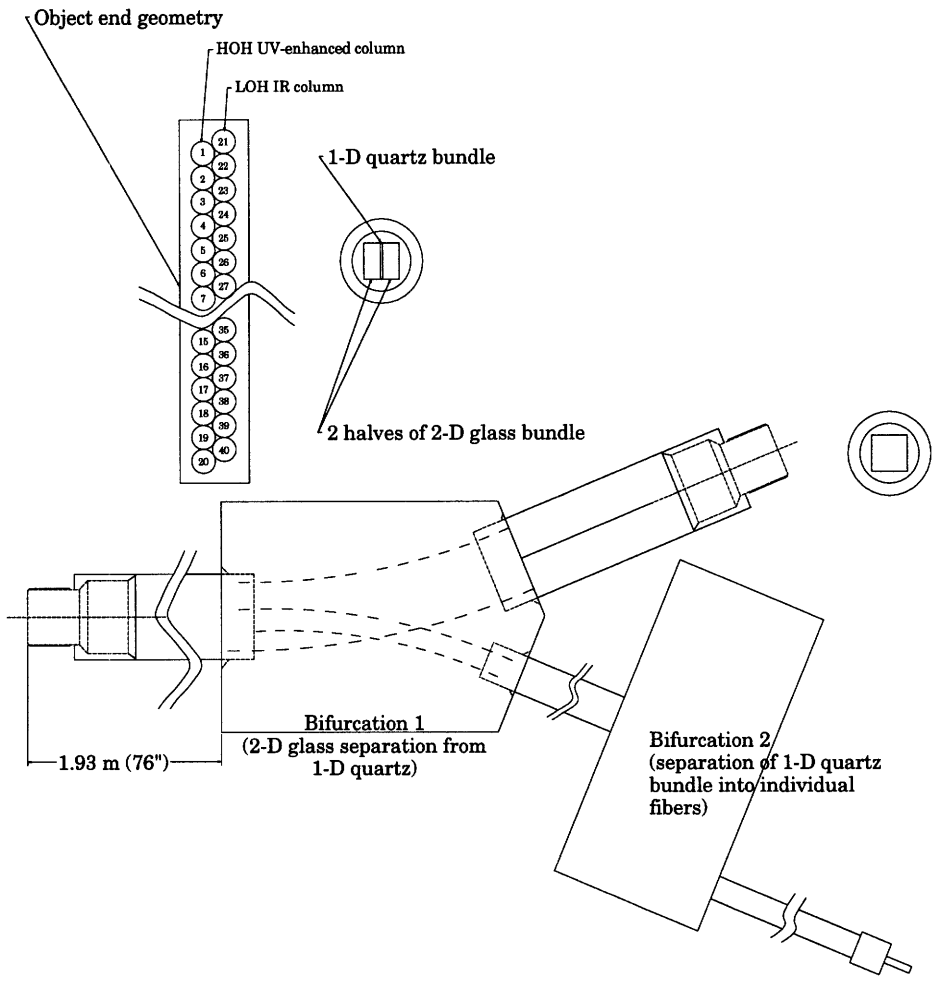

Figure 2-4: Construction drawing for the fiber bundle system of the periscope. In the lower half of the figure, the overall bundle system including the 2 fiber bifurcations is shown. In the upper half, the structure of the periscope input is presented. This bundle input sits directly under the vessel window.

visible and ultraviolet regions, the other one is optimized for use in the visible and the infrared regions of the spectrum.

The input fiber arrangement has to be split in order to provide separate input signals for the different diagnostic instruments. In a first bifurcation, the fibers of the two-dimensional glass fiber array are separated from the 40 single optical quartz fibers. The glass fiber array then forms an output plane for a two-dimensional image. In a second fiber bifurcation, the one-dimensional bundle of optical fibers is broken up into 40 separate fibers. The two bifurcations are illustrated in Fig. 2-4. The *Chromex* spectrometer system only uses the 20 fibers optimized for visible and ultraviolet light. These quartz fibers will be denoted by UV 1, UV 2, ..., UV 20.

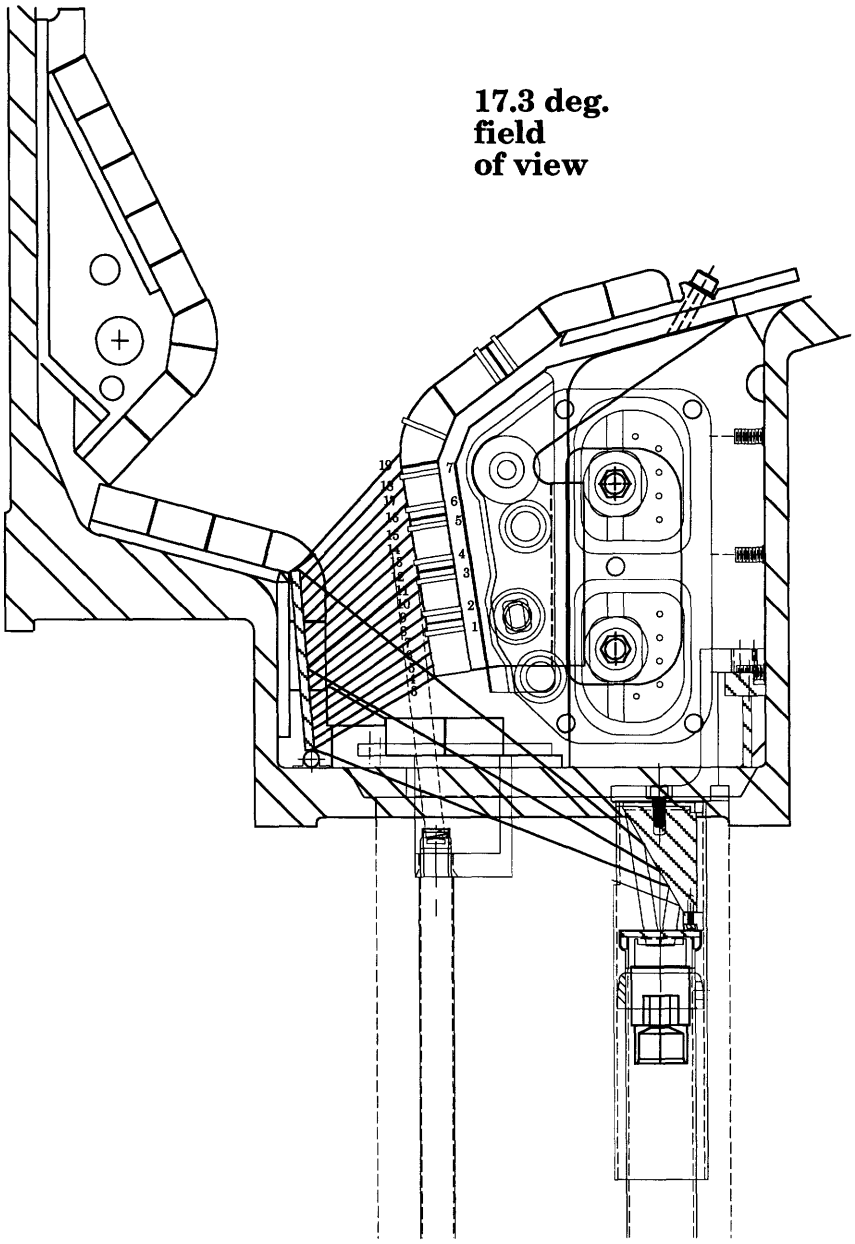

Figure 2-5: Outer divertor view A_{bottom}. Fibers UV 3 - UV 19 allow the analysis of plasma parameters by looking at the outer divertor. Their spatial correspondence with the Langmuir probes FMP 1 - FMP 7 is shown.

Since there are two such periscope bundles available for the *Chromex* system, there are altogether 40 different fibers which provide a set of possible inputs from different spatial positions for the *Chromex* system. A variable subset of them is connected to the 14 *Chromex* spectrometer input fibers, which have a diameter of 200 μm each. These 14 fibers are focused onto the entrance slit of the spectrometer.

2.4.2 Divertor Views

The entire fiber optical system consists of two identically manufactured bundles of the kind described above. These bundles are inserted into two different periscopes at the tokamak, thus providing two different images of the tokamak divertor.

The geometry of the outer divertor view A_{bottom} can be seen in Fig. 2-5; the figure shows the light paths of the radiation observed from the corresponding fibers. Only the 17 fibers UV 3 - UV 19 view the outer divertor surface. The light paths of these fibers end at divertor plate positions where the probes FMP 1 - FMP 7 are situated. These probes are so-called 'domed probes' since they project above the divertor surface (see Ref. [16]). Using data from these Langmuir probes, the electron density N_e and the electron temperature T_e at the probe positions are calculated for every plasma discharge as a function of time.

For the outer divertor views, the light paths through the plasma, ending at the probe positions, are relatively short due to both the geometry of the tokamak divertor and the geometry of the magnetic flux surfaces. The light path through the plasma is constrained by the narrowness of the divertor slot and by the fact that it lies partly within the private flux zone. For the outer divertor views, a correlation between the Langmuir probe data and the density measurements using a spectroscopic method will be examined.

The light paths for the inner divertor view K_{bottom} are presented in Fig. 2-6. All 20 fibers UV 1 - UV 20 observe light radiated by the plasma. The view angle spanned by the K_{bottom} fibers is 34.68° , almost twice the angle of 17.3° spanned by the A_{bottom} fibers. In addition, the path length of the K_{bottom} fibers within the plasma is much longer than the corresponding length for the A_{bottom} fibers, and some of the

inner divertor light paths cross the region near the X-point. Because of the long path-length integration of these views, it cannot be expected that there will be a substantial correlation between Langmuir probe data from the inner divertor surfaces and density measurements using a spectroscopic method.

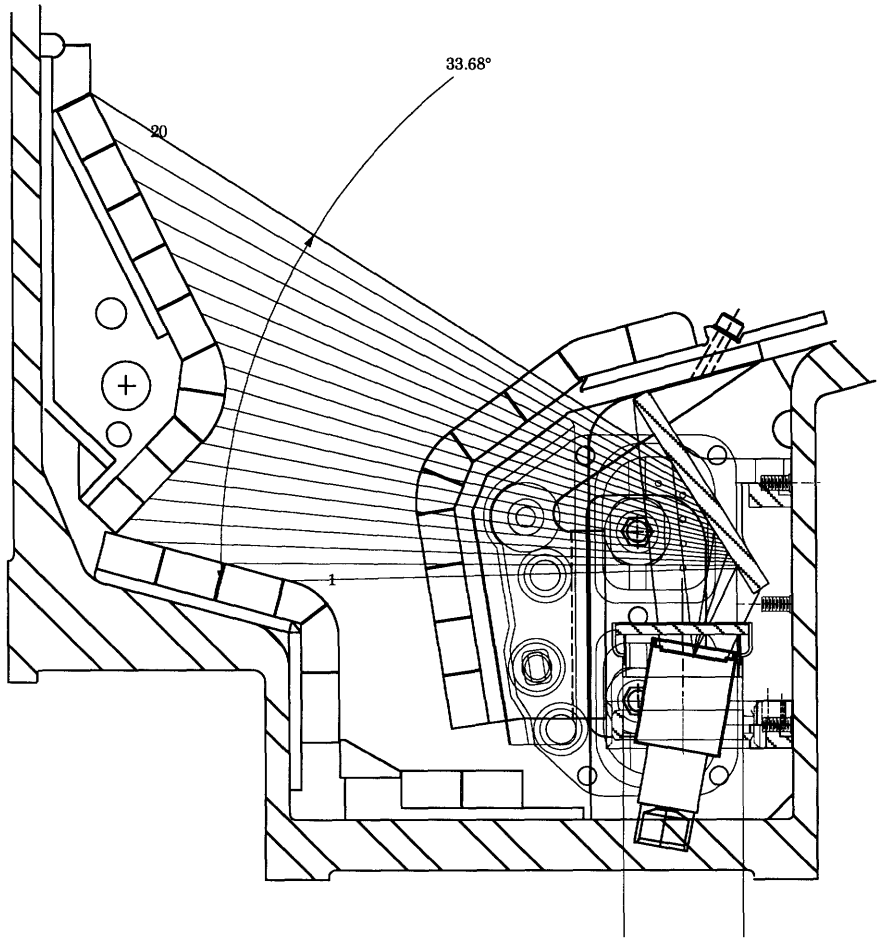

Figure 2-6: Inner divertor view K_{bottom}. Fibers UV 1 - UV 20 allow viewing the plasma by looking at the inner divertor through an opening in the outer divertor.

Chapter 3

Theory of Spectral Line Broadening

This thesis is concerned with the radiation emitted during transitions between discrete atomic energy levels. As the spectral resolution

$$R = \frac{\lambda}{\Delta\lambda} = \frac{\nu}{\Delta\nu} \tag{3.1}$$

of an optical instrument is increased, spectral lines acquire a characteristic functional dependence within frequency or wavelength space, respectively. It is the aim of this chapter to summarize which physical phenomena affect the shape of a spectral line, and to present spectral line profile functions for the phenomena relevant to the plasma diagnostic to be introduced in this thesis. These functions will not be derived from first principles in this work since this chapter shall merely provide the theoretical background for the numerical analysis of experimental data; most of the theory for this chapter can be found in Refs. [17, 24].

It turns out that two functions suffice to describe the spectral line profiles due to many fundamental physical processes, the Gaussian and the Lorentzian:

$$\text{Lorentzian}\,(\nu-\nu_0,\Delta\nu_L) = \frac{1}{\pi}\frac{\Delta\nu_L}{2(\nu-\nu_0)^2+\frac{1}{2}{\Delta\nu_L}^2}\,, \tag{3.2}$$

$$\text{Gaussian}\,(\nu-\nu_0,\Delta\nu_G) = \frac{1}{\sqrt{\pi}}\frac{2\sqrt{\ln 2}}{\Delta\nu_G}\exp\left[-4\left(\frac{\nu-\nu_0}{\Delta\nu_G}\right)^2\ln 2\right]\,. \tag{3.3}$$

These functions are normalized such that

$$\int_{-\infty}^{+\infty} \text{Lorentzian}\,(\nu - \nu_0, \Delta\nu_L)\, d\nu = \int_{-\infty}^{+\infty} \text{Gaussian}\,(\nu - \nu_0, \Delta\nu_G)\, d\nu = 1\,. \qquad (3.4)$$

In the following sections and chapters, the term *width* will always refer to the *full width at half maximum* of a profile in both wavelength and frequency space. Similarly, $\Delta\nu$ and $\Delta\lambda$ always denote full widths at half maximum for all the profiles appearing in this thesis. The only half width at half maximum to appear will be the Stark broadening parameter $\alpha_{1/2}$.

If one observes a spectral line of a motionless atom that is isolated from its neighbors and is shielded from all external electromagnetic fields, one will find that the line has a spectral width, the natural line width. This *natural line broadening* is due to the Heisenberg uncertainty principle. The shape of the spectral profile is a Lorentzian. Its width in frequency space is approximately given by $1/2\pi\tau$, where τ denotes the natural life time of the initial state. In this thesis, the natural line broadening will be ignored since it is negligible compared to other line broadening effects.

The width of spectral lines emitted by a gaseous discharge is also observed to increase with gas pressure and current density. This effect is due to the increased density of neutrals, atoms, and ions in the source, leading to more frequent collisions with and among the radiating atoms. As a result, the decay rates and spectral energy widths of their transitions are increased. This *pressure broadening* can be due to many different types of interactions which can be categorized as *Stark broadening*, *resonance broadening*, *van der Waals' broadening* et cetera. These subdivisions themselves can be classified as either *impact broadening* or *quasi-static broadening* mechanisms, depending on the theory used to analyze them. Within this thesis, Stark broadening will be crucial for calculating the electron densities in the tokamak divertor from the experimental data.

Spectral line shapes are affected by external electromagnetic fields perturbing the energy levels of the radiating atoms. In a plasma discharge, spatial variations in the overall background densities of electrons and ions produce variations of electric fields within the plasma. These fields can be viewed as external for the individual

atom, thereby producing a statistical line broadening. If this broadening is caused by electric fields via the Stark effect, the overall mechanism is called *Stark broadening*. Quantitatively, Stark broadening will dominate all the other broadening mechanisms for high electron densities — $N_e > 3 \cdot 10^{20}\,\mathrm{m}^{-3}$ for the 2–7-transition of deuterium — which can be concluded from the error analysis in chapter 5.

Spectral line broadening can also result from magnetic fields by way of the *Zeeman effect*. The magnetic field leads to an energy splitting of levels which were degenerate in the field-free case. Each of the resulting multiple transition lines exhibits all the broadening phenomena a single transition would exhibit. Since the *Chromex* system cannot resolve the level splitting, the only measurable effect is an overall line broadening due to the overlap of the multiple line profiles which lie too close together to be resolved. The Zeeman splitting of lines is taken into account within the analytical form of the function that is fitted to the measured line shape in order to calculate the electron density.

The random motion of the radiating atoms induces a line broadening due to the Doppler effect. *Doppler broadening* is dependent on the temperature of the radiating species. An attempt will be made to include a correction for Doppler broadening in the electron density measurements based on Stark broadening.

Finally, the optical instrument itself causes a broadening of the spectrum appearing on the exit plane. A theoretical spectral line profile with the shape of a delta function, emitted into the entrance slit of the instrument, would have a finite width on the exit plane. All measurements will also be corrected for this *instrumental broadening*.

3.1 Convolution of Line Profiles

The data acquired will show spectral line profiles that are affected by several different physical processes. Neglecting natural broadening, the profile will still be influenced by the mechanisms of Zeeman splitting, as well as Stark, Doppler, and instrumental broadening. In this section, it will be shown how the separate profiles of the distinct

physical processes combine and lead to a final profile.

I will assume that there are two independent line-broadening mechanisms which are described by the separate profiles $I_1(\delta\lambda)$ and $I_2(\delta\lambda)$. The measured line shape $I(\delta\lambda)$ will then be given by (see Ref. [24, page 302])

$$I(\delta\lambda) = \int_{-\infty}^{+\infty} I_1(\delta\lambda')\, I_2(\delta\lambda - \delta\lambda')\, \mathrm{d}(\delta\lambda') \,. \tag{3.5}$$

Let us assume that we have two functions $f(x)$ and $g(x)$

$$f, g : \mathcal{R} \rightarrow \mathcal{R}_+ \cup \{0\} \,, \tag{3.6}$$

where both f and g are Lebesgue integrable. We can then define a shorthand for the convolution integral:

$$(f * g)(y) \equiv \int_{-\infty}^{+\infty} f(x)\, g(y - x)\, dx \,. \tag{3.7}$$

As derived in Ref. [6, page 75], the convolution $*$ is commutative:

$$\forall y \in \mathcal{R} \backslash \mathrm{N} : (f * g)(y) = (g * f)(y) \,;\; \int_{\mathrm{N}} dx = 0 \,. \tag{3.8}$$

One can also derive that the convolution $*$ is associative:

$$((f * g) * h)(y) = (f * (g * h))(y) \,. \tag{3.9}$$

The two properties of the convolution which are expressed in equations 3.8 and 3.9 are sufficient to unfold the spectral profiles of the experimental data.

We will also need to know how a Lorentzian and a Gaussian behave with respect to the convolution $*$. The following theorems will be stated without proof:

$$\begin{aligned} \text{Lorentzian}\,(\nu - \nu_0, \Delta\nu_1) \quad &* \quad \text{Lorentzian}\,(\nu - \nu_0, \Delta\nu_2) \\ &\longrightarrow \quad \text{Lorentzian}\,(\nu - \nu_0, \Delta\nu_1 + \Delta\nu_2) \,. \end{aligned} \tag{3.10}$$

$$\begin{aligned} \text{Gaussian}\,(\nu - \nu_0, \Delta\nu_1) \quad &* \quad \text{Gaussian}\,(\nu - \nu_0, \Delta\nu_2) \\ &\longrightarrow \quad \text{Gaussian}\,(\nu - \nu_0, \sqrt{{\Delta\nu_1}^2 + {\Delta\nu_2}^2}) \,. \end{aligned} \tag{3.11}$$

The profile resulting from the convolution of a Gaussian profile with a Lorentzian profile remains to be determined. It is derived in Ref. [17, page 250], and is given by:

$$\alpha(a,w) = \frac{\alpha_0\, a}{\pi} \int_{-\infty}^{+\infty} \frac{\exp[-y^2]}{a^2 + (w-y)^2}\, dy \ . \tag{3.12}$$

From the width $\Delta\nu_G$ of the Gaussian profile and the width $\Delta\nu_L$ of the Lorentzian profile, one can calculate the parameters:

$$w = \frac{2(\nu - \nu_0)\sqrt{\ln 2}}{\Delta\nu_G} \ , \tag{3.13}$$

$$a = \frac{\Delta\nu_L}{\Delta\nu_G}\sqrt{\ln 2} \ . \tag{3.14}$$

The constant α_0 only affects the overall scale of the profile. For our purposes, we will require that α_0 is appropriately chosen such that the overall profile is normalized to a unit area. The coefficient of the function $\alpha(a,w)$ is then automatically equal to the integral of the line profile over the entire frequency space, a fact which will make it much easier to calculate the intensities of transitions. The profile $\alpha(\nu)$ is called a *Voigt profile* [*ibidem*, page 248]. Defining

$$\text{Voigt}\,(a,w) \equiv \alpha(a,w) \ , \tag{3.15}$$

we can write:

$$\begin{aligned} \text{Lorentzian}\,(\nu - \nu_0, \Delta\nu_L) \quad &* \quad \text{Gaussian}\,(\nu - \nu_0, \Delta\nu_G) \\ &\longrightarrow \quad \text{Voigt}\left(a\left(\frac{\Delta\nu_L}{\Delta\nu_G}\right),\, w(\nu - \nu_0, \Delta\nu_G)\right) \ . \end{aligned} \tag{3.16}$$

3.2 Instrumental Broadening

Ideally, a spectrometer would analyze the incoming radiation into pure monochromatic beams without any frequency overlap. In practice, spectral lines have a profile on the exit plane of the spectrometer, even if the instrumental resolution is not sufficient to observe the spectral width of the incoming radiation. The reason lies in the fact that the instrument itself causes a broadening of the lines.

3.2.1 Theoretical Assumptions about the Instrumental Profile

To correct the measurements for the inherent instrumental broadening, I will assume that the instrumental line profile is itself a convolution of a Gaussian with a Lorentzian profile, thus a Voigt profile. I will characterize the instrument by the variables $\Delta\lambda_{Instr,G,grating}$ and $\Delta\lambda_{Instr,L,grating}$ where the indices 'G' and 'L' refer to the Gaussian and Lorentzian widths respectively. Assuming that radiation with a spectral width much narrower than the instrumental resolution is emitted into the instrument, a Voigt profile described by the parameter

$$a_{Instr,grating} = \sqrt{\ln 2}\,\frac{\Delta\lambda_{Instr,L,grating}}{\Delta\lambda_{Instr,G,grating}} \tag{3.17}$$

and with a total measured width of $\Delta\lambda_{Instr,Voigt}$ will appear on the exit plane. As indicated, these parameters will be dependent on the grating used for a fixed slit width.

3.2.2 Determination of the Instrumental Broadening Parameters

In order to determine the characteristic instrumental widths for each grating, a low-pressure mercury lamp is used as a light source. Spectra are measured for the transitions which minimize the coma of the grating. A least squares fit to the spectral detector profiles is performed, giving both $\Delta\lambda_{Instr,Voigt,grating}$ and $a_{Instr,grating}$ as results.

Grating [mm^{-1}]	$\Delta\lambda_{Instr,Voigt}$[Å]	$\Delta\lambda_{Instr,L}$[Å]	$\Delta\lambda_{Instr,G}$[Å]	Transition [nm]
600	2.68	1.37 ± 1.10	1.89	404.66
1200	1.29	0.44 ± 0.21	0.98	546.07
1800	0.79	0.25 ± 0.14	0.61	253.65

Table 3.1: Instrumental broadening parameters: total, Lorentzian, and Gaussian widths of the profile, as obtained for the different gratings and for a slit width of 20 μm, using the given spectral lines emitted from a low pressure mercury lamp.

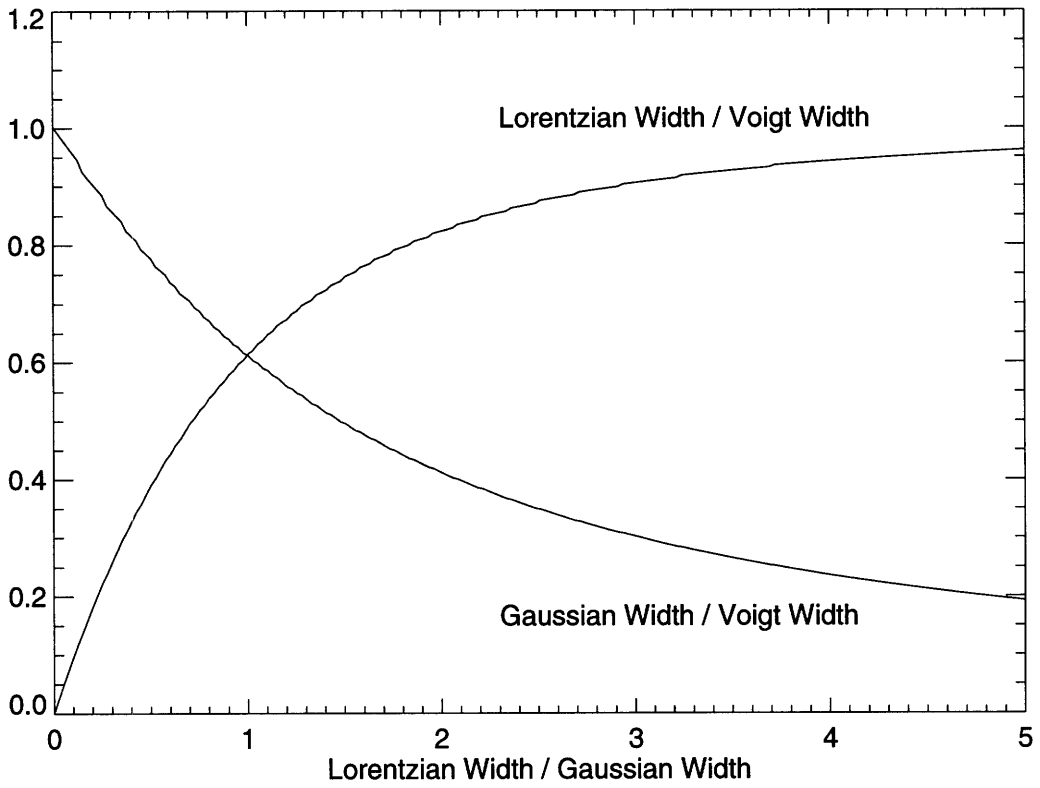

Figure 3-1: $\Delta\lambda_L/\Delta\lambda_{Voigt}$ and $\Delta\lambda_G/\Delta\lambda_{Instr,Voigt}$ are numerically calculated as functions of $\Delta\lambda_L/\Delta\lambda_G$.

The ratios $\Delta\lambda_L/\Delta\lambda_{Voigt}$ and $\Delta\lambda_G/\Delta\lambda_{Voigt}$ have been calculated numerically as functions of $\Delta\lambda_L/\Delta\lambda_G$. These two curves, given in Fig. 3-1, are in agreement with Ref. [24, page 303, Table V]. Using these functions, the widths $\Delta\lambda_{Instr,G}$ and $\Delta\lambda_{Instr,L}$ can be calculated from $\Delta\lambda_{Instr,Voigt}$ and a_{Instr} for the three different gratings. The results are summarized in Table 3.1.

The coma of the grating introduces asymmetries in the appearance of the detected transition lines, thereby introducing errors in the fitted instrumental widths. The uncertainties in the Lorentzian widths of the instrumental profiles are also listed in Table 3.1. These uncertainties were determined by fitting the asymmetric halves of the profiles separately and comparing the results. For the $1800\,\mathrm{mm}^{-1}$ grating, which will be most frequently used in our application, the inaccuracy of the instrumental width will be $\sim 0.14\,\text{Å}$. For electron densities larger than $3 \cdot 10^{20}\,\mathrm{m}^{-3}$, the 2–7-transition of deuterium exhibits Stark broadening widths larger than 2.06 Å. The uncertainty

of the electron density due to the inaccuracy of the instrumental width will then be smaller than 10%.

3.3 The Doppler Effect in a Maxwellian Gas

In order to calculate the spectral profile of the light emitted from a gas of atoms or molecules, one has to apply the Doppler effect to a statistical sample. The objects emitting the radiation — their mass is denoted by M_a — will be assumed to have a Maxwellian distribution given by

$$P(v) = \left(\frac{M_a}{2\pi kT}\right)^{\frac{1}{2}} \exp\left[-\frac{M_a v^2}{2kT}\right]. \tag{3.18}$$

Here, k denotes the Boltzmann constant and $T[^\circ \mathrm{K}]$ the absolute temperature of the emitting species.

In addition, we will neglect the natural width of the spectral line and assume that its spectral profile is properly described by a delta function, an entirely feasible assumption, given the resolution of our instrument. Based on these assumptions, it can be derived (see Ref. [17, page 248]) that the resulting spectral profile due to Doppler broadening is a Gaussian whose width is given by

$$\Delta\nu_{Doppler} = \frac{2\nu_0}{c}\sqrt{\frac{2kT\,\ln 2}{M_a}}\,. \tag{3.19}$$

In our experimental setup, the emitting objects will be neutral deuterium atoms. The corresponding neutral temperature T describes their underlying distribution function. Measurements performed by another diagnostic instrument, a Fabry-Perot interferometer, indicate that this distribution function is peaked around $T = 2\,\mathrm{eV}$ in the tokamak divertor. For these measurements, the 2–3-transition of deuterium was used. Accordingly, $T = 2\,\mathrm{eV}$ will be used to calculate the width of the Doppler broadening profile throughout this thesis. As an example, the width of the Gaussian Doppler profile for the deuterium 2–9-transition can be calculated to be

$$\Delta\lambda_{Doppler} = 0.295\,\text{Å}. \tag{3.20}$$

3.4 Stark Broadening

The fundamental physics leading to Stark broadening has been described earlier in this chapter. We will be concerned here only with Stark profiles derived for the hydrogen Balmer series.

3.4.1 Determination of Electron Densities from Stark Widths

The theoretical Stark profiles numerically calculated for the hydrogen Balmer series are usually presented as one half of the symmetrical profile $S(\alpha)$ where

$$\alpha \equiv \frac{\delta\lambda\,[\text{Å}]}{F_0}\,, \tag{3.21}$$

$$F_0 = 1.25 \cdot 10^{-13} \left(N_e\,[\text{m}^{-3}]\right)^{2/3}, \tag{3.22}$$

and $\delta\lambda$ denotes the distance from the line center (see Ref. [24, page 274]). F_0 is called *Holtzmark field strength*. The profiles $S(\alpha)$ are again normalized via

$$\int_{-\infty}^{+\infty} S(\alpha)\, d\alpha = 1\,. \tag{3.23}$$

For the Balmer transitions between H_α and H_δ, tabulated profiles and the underlying theory of their calculation can be found in Ref. [8].

For our purposes, it will be sufficient to use the fact that, to a first approximation, the width of the Stark broadening in wavelength space scales algebraically with the electron density at the point of emission (see Ref. [24, page 274]):

$$\Delta\lambda_{Stark}\,[\text{Å}] = 2.50 \cdot 10^{-13}\, \alpha_{1/2} \left(N_e\,[\,\text{m}^{-3}]\right)^{2/3}. \tag{3.24}$$

Here, $\alpha_{1/2}$ is the *half* width at half the maximum of the corresponding profile $S(\alpha)$ for a particular transition.

It should be noted that, in principle, the theoretical Stark width $\alpha_{1/2}$ is itself dependent on both the electron density N_e and the electron temperature T_e. These higher order effects are not taken into account, an approach which is not entirely unjustified. As stated in Ref. [8, page 1], the temperature tends to be of minor influence on the observed line widths. As can be seen in Ref. [11, page 323, Table I],

the theoretical Stark widths $\alpha_{1/2}$ for the H_δ-transition vary only between 0.171 and 0.174 within an electron temperature range of

$$5 \cdot 10^3 \,^\circ\mathrm{K} < T_e < 4 \cdot 10^4 \,^\circ\mathrm{K} \tag{3.25}$$

for a fixed electron density of $N_e = 10^{21}\,\mathrm{m}^{-3}$. The typical electron temperatures in the tokamak divertor lie in the order of $10^4\,^\circ\mathrm{K}$, but can reach values up to $5 \cdot 10^5\,^\circ\mathrm{K}$. It turns out that MARFE phenomena, which will prove to be the objects most suitable for our application, do exhibit electron temperatures satisfying relation 3.25.

It must also be remarked that the theoretical Stark profile will be approximated by a Lorentzian, as is suggested in Ref. [24, page 270]. This assumption is necessary since other analytical approximations are not available in the literature. Lorentzians are particularly useful here since their shape resembles the large wings of the theoretical Stark profiles. More generally, the Lorentzian shape fits the Stark broadening profiles of heavier elements more closely, as is mentioned in [*ibidem*, page 302].

3.4.2 Transitions Used for Stark Broadening Analysis

For the calculation of electron densities from spectroscopic data, the transitions in the Balmer series of deuterium will be used. Since the Alcator C-Mod tokamak is fueled with deuterium, these emission lines have a relatively high brightness. The Balmer series is particularly suitable for observation with the *Chromex* spectrometer system since all transitions of the series lie within the range of the wavelength calibration of the instrument.

The calculation of electron densities, as outlined above, relies heavily on a precise measurement of the spectral profiles. For that reason, electron densities will only be derived from spectroscopic data acquired by use of the $1200\,\mathrm{mm}^{-1}$ or the $1800\,\mathrm{mm}^{-1}$ grating. In addition, it is desirable to have as many transitions as possible within a spectrum available for analysis. A high resolution is equivalent to a small spectral band width. In order to achieve both high resolution and an observation of several transitions within one spectrum, one has to observe the high-n transitions of the series near the ionization limit. Therefore, the analysis will focus on the four Balmer series

transitions 2–7, 2–8, 2–9, and 2–10.

An optimal setup of the instrument for density measurements would employ the $1800\,\mathrm{mm}^{-1}$ grating with $\lambda_{\text{chromex}} = 385.0\,\mathrm{nm}$. The resulting spectral band between $\approx 362\,\mathrm{nm}$ and $\approx 407\,\mathrm{nm}$ would include the four transitions mentioned as well as the effective ionization limit, which is defined by the Inglis-Teller limit (Ref. [9]). The theoretical Stark widths $\alpha_{1/2}$ have been calculated in Ref. [1] using the impact approximation for electrons and the quasi-static approximation for ions. The calculations are performed for an electron density of $N_e = 1.2 \cdot 10^{19}\,\mathrm{m}^{-3}$ and an electron temperature of $T_e = 1\,850°\,\mathrm{K}$. In the same reference, the theoretical results were compared with experimental measurements, leading to experimental widths which were between 10% and 15% lower than the theoretical widths.

The quasi-static approximation and the impact approximation are the two extreme approximations in the general theory of pressure broadening. The quasi-static approximation is valid when the perturbing charges move relatively slowly so that the perturbing field during the interaction time — which is of the order of the lifetime of the excited state — can be described as 'quasi-static': the emitting system is considered to be continuously under the influence of the perturbers during the entire emission process. The quantitative results will then be independent of the temperature of the perturbing species. In contrast, in the impact approximation the emitting system is assumed to be unperturbed most of the time, only perturbed by fast impacts. This approximation therefore requires that the duration of a collision be short compared to the time between collisions, and compared to the unperturbed lifetime

n	λ [nm]	$\alpha_{1/2}$
6	410.06	0.150
7	396.90	0.184
8	388.80	0.283
9	383.43	0.345
10	379.69	0.458
∞	364.50	—

Table 3.2: Theoretical Stark widths $\alpha_{1/2}$ for transitions in the Balmer series of deuterium from Ref. [1]. n gives the principal quantum number of the initial state. The wavelength data are taken from Ref. [21, page 75].

of the state.

Both electron temperature and electron density for which the widths $\alpha_{1/2}$ were calculated lie below the range for which they will be used in our application. This is only justified under the condition that both the quasi-static approximation for the ions and the impact approximation for the electrons — which were used in the calculation — are still valid for our parameter ranges. The equation for the validity of the quasi-static approximation is given in Ref. [8, page 9, equation (17)]. The same equation can be used to describe the validity of the impact approximation of the electrons, since the impact approximation is the complement of the quasi-static approximation. Taking into account the remarks in [*ibidem*, page 33], the results for protons and electrons are summarized in [*ibidem*, page 11, Fig. 1] for the Balmer series of hydrogen. For the 2–7-transition, the electron impact approximation *and* the quasistatic approximation for ions are valid over the entire electron density range

$$5 \cdot 10^{18}\,\mathrm{m}^{-3} < N_e < 4 \cdot 10^{22}\,\mathrm{m}^{-3}\,, \tag{3.26}$$

"at least for portions of the profiles near or within the half-intensity points" [*ibidem*, page 33]. Our application lies well within these bounds.

It has already been argued above that the temperature dependence of the calculated Stark widths tends to be minor. It remains to be seen whether the results for the theoretical Stark widths presented in Table 3.2 can be used for our parameter ranges. This question will be discussed by comparing the results presented here for the H_δ-transition with the corresponding results presented in Ref. [11].

For an electron density of $N_e = 10^{19}\,\mathrm{m}^{-3}$ and an electron temperature of $T_e = 5\,000°\,\mathrm{K}$, Ref. [11] lists a theoretical Stark width of $\alpha_{1/2,2-6} = 0.149$ for the H_δ-transition. This is in perfect agreement with the result presented in Table 3.2, especially because the Stark widths in Ref. [11] increase with decreasing temperature. For the intended use of our application, an electron density of $N_{e,typical} = 10^{21}\,\mathrm{m}^{-3}$ and an electron temperature of $T_{e,typical} = 30\,000°\,\mathrm{K}$ are to be considered typical. For these parameters, Ref. [11] gives a theoretical Stark width of $\alpha_{1/2,2-6,typical} = 0.173$.

So the error in the theoretical Stark width presented in Table 3.2 is about 15%

for the H_δ-transition, given the typical plasma parameters for our application. Since the theoretical Stark widths $\alpha_{1/2}$ increase with electron density, the values given in Table 3.2 will generally be too small. An underestimate of the theoretical Stark widths by 15% translates into an overestimate of the measured electron density by approximately 19%.

3.5 Zeeman Splitting

The *form* of the energy level splitting due to an external magnetic field is dependent on the strength of the magnetic field. In general, one distinguishes between the *anomalous* Zeeman effect for the case of a weak magnetic field and the Zeeman effect in the *Paschen-Back* regime for strong magnetic fields, also referred to as the *Paschen-Back effect*.

3.5.1 The Regime of Zeeman splitting

The parameter indicating the relevant regime is defined as ξ in Ref. [2, page 211].

$$\xi = \frac{\mathcal{H}\mu_0}{\Delta E} \; ; \; \Delta E \equiv E_+ - E_- \tag{3.27}$$

For $\xi \ll 1$ the regime of the anomalous Zeeman effect is given, for $\xi \gg 1$ the Paschen-Back regime. μ_0 denotes the Bohr magneton:

$$\mu_0 = \frac{e\,\hbar}{2\,m_e\,c} \tag{3.28}$$

Let $\mathbf{M}$ denote the quantum mechanical operator for the total angular momentum of an electronic bound state of the deuterium atom. Let the eigenvalues of $\mathbf{M^2}$ be denoted by $j(j+1)\hbar^2$. Similarly, $0 \leq l \leq n-1$ shall denote the quantum number describing the orbital angular momentum of the state.

The quantities E_+ and E_- then denote the "field-free energies of the Pauli approximation" for the eigenstates of $\mathbf{M^2}$ with the quantum number $j_+ = l + \frac{1}{2}$ and $j_- = \left|l - \frac{1}{2}\right|$. The energy levels in the Pauli approximation are given by [*ibidem*,

page 61]:

$$W = -\frac{Z^2}{n^2}\left[1 + \frac{(\alpha Z)^2}{n}\left(\frac{1}{j+\frac{1}{2}} - \frac{3}{4n}\right)\right] \mathrm{Ry}\,, \tag{3.29}$$

where $\mathrm{Ry} = 13.6\,\mathrm{eV}$ is the Rydberg energy unit, α is the fine structure constant, $Z = 1$ is the number of electrons per atom for deuterium, and n is the principal quantum number of the level.

Let W_0 denote the non-relativistic field-free energy of the level described by n. The fine structure splitting between states characterized by j_+ and j_- is given by

$$\Delta E = W_0 \frac{(\alpha Z)^2}{n}\left(\frac{1}{j_+ + \frac{1}{2}} - \frac{1}{j_- + \frac{1}{2}}\right). \tag{3.30}$$

Since $j_+ = j_- \Leftrightarrow l = 0$, the fine structure splitting vanishes only in the case of $l = 0$. Assuming $l \neq 0$ and inserting the expressions for j_+ and j_-, we obtain:

$$\Delta E = W_0 \frac{(\alpha Z)^2}{n}\frac{1}{l(l+1)}\,. \tag{3.31}$$

For the $n = 2$ hydrogen level with $l = 1$, the quantum number $j_- = \frac{1}{2}$ corresponds to both the $2S_{1/2}$- and the $2P_{1/2}$-state, whereas $j_+ = \frac{3}{2}$ refers to the $2P_{3/2}$-state. So using equation 3.31 with $l = 1$, one can calculate

$$\Delta E_{n=2,l=1} = 0.365\,\mathrm{cm}^{-1} = 7.26 \cdot 10^{-24} J, \tag{3.32}$$

corresponding to $\xi = 1$ for a field strength of [*ibidem*, page 212]

$$\mathcal{H}_{n=2,l=1} \approx 7\,800\,\mathrm{Gauss} = 0.78\,\mathrm{Tesla}\,. \tag{3.33}$$

Since

$$\Delta E \sim \frac{1}{n^3}, \tag{3.34}$$

the corresponding field strength for the energy level $n = 7$ with $l = 1$ will be of the order $\mathcal{H} = 18.2\,\mathrm{mT}$.

As a result, for low magnetic fields in the tokamak divertor ($B < 2\,\mathrm{T}$), the deuterium levels $n = 7, \ldots, 10$ can be described by the Paschen-Back effect whereas the level $n = 2$ is in an intermediate regime between Paschen-Back and anomalous Zeeman effect. Transitions between these levels undergo the *partial* Paschen-Back effect. For intermediate and high magnetic fields ($B > 4\,\mathrm{T}$), both levels will be in

the Paschen-Back regime. Since the energy splittings for low magnetic fields will be relatively small compared to the other broadening effects, I will assume that we are solely dealing with this *complete* Paschen-Back effect.

3.5.2 The Energy Splitting

Let m_l denote the quantum number for the component of the orbital angular momentum which is parallel to the magnetic field vector $\vec{B}$. m_s shall denote the corresponding quantum number for the electron spin. Please note that the notation has changed from the last section. The energy shift ΔE_B due to the magnetic field is calculated for the Paschen-Back regime in Ref. [20, page 310]:

$$\Delta E_B = -\frac{e\hbar}{2\,m_e\,c}\,|B|\,(m_l + 2m_s)\;. \tag{3.35}$$

Assuming that both levels undergo a complete Paschen-Back effect, the transitions have to satisfy the selection rules (Ref. [2, page 210])

$$\Delta m_s \;=\; 0\;; \tag{3.36}$$

$$\Delta m_l \;=\; 0, \pm 1;\;\text{ depending on the polarization of the light.} \tag{3.37}$$

The transitions appearing in the spectrum are then derived from

$$E_{spectrum} = E_{init} - E_{final} - \Delta m_l \frac{e\hbar}{2\,m_e\,c}\,|B|\;. \tag{3.38}$$

Neglecting a further splitting of these 3 levels due to spin-orbit coupling, the spectral lines have the appearance of a Lorentz triplet. The center line will have twice the intensity of the shifted lines. The splitting due to the Zeeman effect in the Paschen-Back regime, together with the relative intensities of the lines, is illustrated in Ref. [2, page 211, Fig. 22].

For the purposes of this thesis, the splitting introduced due to the magnetic field will therefore be calculated using

$$\frac{\Delta\lambda_{Zeeman}}{\lambda_0} = \frac{\omega_{ce}}{\omega_0} = \frac{e\,B}{m_e\,c}\,\frac{\lambda_0}{2\pi\,c}\,, \tag{3.39}$$

where ω_{ce} denotes the electron cyclotron frequency. For a magnetic field of $B = 5\,\mathrm{T}$, the deuterium transition 2-9 would exhibit a Zeeman splitting of 0.694 Å.

3.5.3 The Effect of Zeeman Splitting on the Spectral Profiles

Even for the maximal magnetic fields of $B_{max} = 8\,\mathrm{T}$ occurring in the divertor, the *Chromex* spectrometer system will not be able to resolve the corresponding splitting into separate peaks. Therefore, the magnetic field will effectively broaden the measured line widths in addition to the other broadening mechanisms.

In the absence of a magnetic field, the spectral profile could be described by the following functional form:

$$F^{B=0}(\vec{V}, w) = V_1 \,\mathrm{Voigt}\,(V_0, w) + V_2 + V_3\, w\,. \tag{3.40}$$

The parameter V_0 takes the place of the form parameter a of the Voigt profile. The variable w is again the distance from the line center scaled by the Gaussian width as defined in equation 3.13. $F^{B=0}(\vec{V}, w)$ is essentially a Voigt profile with an overall scale, a constant offset V_2, and a linear correction V_3 to the background.

In the presence of a magnetic field, the single line described by equation 3.40 will split into three lines. Each of these three separate lines will be broadened by the same physical processes which affect the single line shape. Calculations of spectral line profiles due to combined Stark and Zeeman effects have been carried out in Ref. [18], but only for the transitions L_α, L_β, and H_α. In this thesis, I will assume that each of the three existing lines in the presence of a magnetic field is *quantitatively* affected in the same way as the single line in the absence of a magnetic field. The Lorentzian and the Gaussian widths of each of the three lines described by $\Delta m_l = 0, \pm 1$ will be assumed to be equal to the corresponding widths of the single line in the zero magnetic field case. This is indeed an approximation: although it is certainly correct for the Doppler profile and the instrumental profile, it is not true *a priori* for the Stark profile.

With this approach, one can approximate the measured profile of the spectral lines by a superposition of three Voigt profiles. They have the same shape parameter a, amplitudes corresponding to the relative intensities of the transitions $\Delta m_l = 0, \pm 1$, and centers in w-space shifted by $w_{center,\Delta m_l} = \frac{1}{2}\,\Delta m_l\,\Delta w_{Zeeman}$.

The quantity Δw_{Zeeman} denotes the full splitting of the transition in w-space, that is, the splitting between the transitions $\Delta m_l = \pm 1$. Noting that this splitting in frequency space is given by

$$\Delta \nu_{Zeeman} = \frac{2\,\mu_0\,|B|}{h}\,, \tag{3.41}$$

it follows that

$$\Delta w_{Zeeman} = 4\,\sqrt{\ln 2}\,\frac{\mu_0\,|B|}{h\,\Delta \nu_G}\,. \tag{3.42}$$

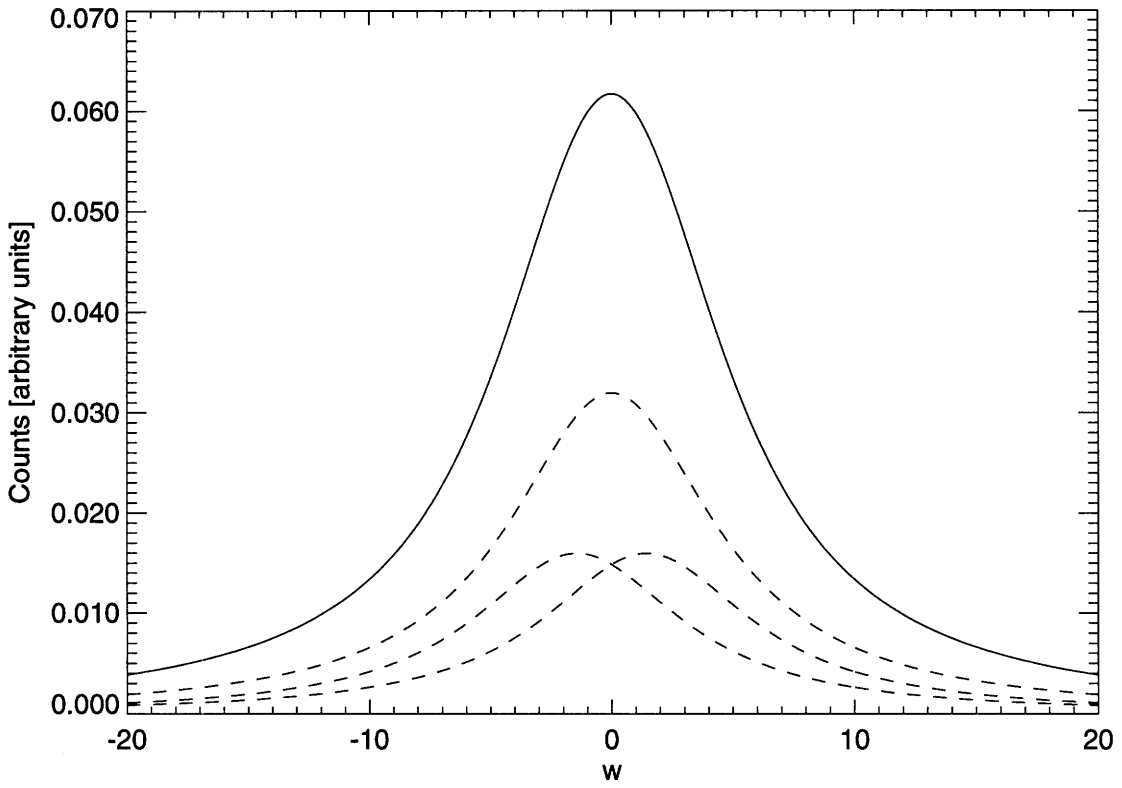

Figure 3-2: The form of the spectral line shape in the presence of a magnetic field, plotted in w-space. The solid curve shows $F^{Zeeman}(\vec{V}, w, \Delta w_{Zeeman})$ with the parameters $\vec{V} = (5, 1, 0, 0)$. $\Delta w_{Zeeman} = 2.87 \Leftrightarrow \Delta \lambda_{Zeeman} = 1.18\,\text{Å}$ was calculated for the deuterium 2-7 transition, assuming a magnetic field of $B = 8\,\text{T}$ and a temperature of $T = 2\,\text{eV}$. The three dashed curves show the three transitions $\Delta m_l = 0, \pm 1$ separately.

The overall functional form approximating the measured profile in the presence of a magnetic profile can then be written as

$$\begin{aligned} F^{Zeeman}(\vec{V}, w, \Delta w_{Zeeman}) &= \frac{1}{2} V_1 \,\text{Voigt}\,(V_0, w) \\ &+ \frac{1}{4} V_1 \,\text{Voigt}\,(V_0, w - \frac{1}{2}\Delta w_{Zeeman}) \\ &+ \frac{1}{4} V_1 \,\text{Voigt}\,(V_0, w + \frac{1}{2}\Delta w_{Zeeman}) + V_2 + V_3\, w\,, \end{aligned} \tag{3.43}$$

where Δw_{Zeeman} is given by equation 3.42.

Except for the magnitude of the magnetic field B, which is required for the calculation of Δw_{Zeeman}, equations 3.43 and 3.40 are dependent on the same parameters. As expected, the function $F^{Zeeman}(\vec{V}, w, \Delta w_{Zeeman})$ reduces to $F^{B=0}(\vec{V}, w)$ in the absence of a magnetic field.

The superposition of the three Voigt profiles leading to the spectral shape function $F^{Zeeman}(\vec{V}, w, \Delta w_{Zeeman})$ is illustrated in Fig. 3-2. From this plot, it is apparent that one cannot expect the experimental data to exhibit three separate peaks, not even at the highest magnetic fields.

Chapter 4

Numerical Procedure for the Analysis of Broadened Deuterium Lines

This chapter will describe in detail the method by which a raw spectrum is analyzed in order to obtain the underlying electron density. I assume that the optimal system setup was chosen for the data acquisition, such that the four deuterium Balmer transitions 2-7, 2-8, 2-9, 2-10 are analyzed with the highest possible instrumental resolution. The analysis is based on a single-transition fit: the electron density is extracted from an individual spectral line independent of its series neighbors. Thus, strictly speaking, it is not necessary to have more than one line present in a spectrum. However, multiple lines allow for a comparison of the different results.

It is entirely sufficient to use count spectra — as opposed to brightness spectra — for the density analysis since the spectral sensitivity of the instrument is constant over the fit interval surrounding a spectral line to a very good approximation. The experimental data will be represented by two vectors of the same length:

$$\begin{aligned} \vec{i}(y,t) &= (i_1, i_2, ..., i_{1242}) \ , \\ \vec{\lambda}_{cal}(y) &= (\lambda_{cal,1} \ , \lambda_{cal,2} \ , ..., \lambda_{cal,1242}) \ . \end{aligned}$$

The element $i_x(y,t)$ represents the number of counts on the bin (x,y) of the detector

plane, measured at time t of a specific discharge. The calibration map provides the wavelength $\lambda_{cal,x}(y)$ corresponding to that bin for that specific discharge.

4.1 Fundamental Fitting Process

In the following, the analysis procedure will be described for a data set which is 'appropriate' for calculating the electron density. A data set is 'appropriate' if it does not fulfill any of the rejection criteria listed in a later section of this chapter.

Let the spectral wavelength of the analyzed transition be denoted by λ_0. The analyzing software selects all the data points whose calibrated wavelengths lie in an interval surrounding this central wavelength:

$$\lambda_{cal,x} \in I_{max} = [\lambda_0 - \Delta\lambda_{left} \ , \ \lambda_0 + \Delta\lambda_{right}] \ . \tag{4.1}$$

The bin (x, y) with the maximal number of counts among those data points is determined to correspond to $\lambda_{cal,max}$. In general, $\Delta\lambda_{left} \neq \Delta\lambda_{right}$. The interval edges are chosen such that an impurity close to the deuterium transition cannot be mistaken for the line maximum.

The analysis interval is then recentered around the wavelength $\lambda_{cal,max}$:

$$I_{center} = [\lambda_{cal,max} - \Delta\lambda_{left} \ , \ \lambda_{cal,max} + \Delta\lambda_{right}] \ . \tag{4.2}$$

The data points in the interval I_{center} are used for a fit to the Gaussian

$$f(\vec{G}, x) = G_0 \exp\left(-\frac{z^2}{2}\right) + G_3 + G_4\, x + G_5\, x^2 \ , \tag{4.3}$$

$$z = \frac{x - G_1}{G_2}. \tag{4.4}$$

For this preliminary least squares fit, it is not relevant that the functional form is specifically a Gaussian since this fit is only used to determine the initial estimates for the later fitting procedures.

The vector $\vec{G} = (G_0, ..., G_5)$ is returned as the result of the least squares fit. The Gaussian is centered on the data and its peak in wavelength space does not necessarily coincide with the point where that data set has its absolute maximum. The variable

G_1 will then be equal to the wavelength which is assigned to the transition by the wavelength calibration. The wavelength data are now shifted onto its final spectral value:

$$\vec{\lambda}_{spec}(y,t) = \vec{\lambda}_{cal}(y,t) + \lambda_0 - G_1 \ . \tag{4.5}$$

This procedure allows one to exclude all errors which could result from the absolute wavelength calibration. The analysis is solely dependent on the dispersion measurements.

Let us assume that p is the number of data points lying in the interval

$$I_{fit} \equiv \left[\lambda_0 - \frac{1}{2}\Delta\lambda_{sym} \ , \ \lambda_0 + \frac{1}{2}\Delta\lambda_{sym}\right] \ , \tag{4.6}$$

where $\Delta\lambda_{sym}$ denotes the width of the fitting interval in wavelength space. The points for the final data fitting procedure are selected as follows:

$$\begin{aligned} \vec{\lambda}_{fit} &= \left(\lambda_{spec,x_1} \ , ..., \lambda_{spec,x_k} \ , ..., \lambda_{spec,x_p}\right) \ , \qquad (4.7) \\ \forall k \in \{1,...,p\} : \lambda_{spec,x_k} &\in I_{fit} \ , \\ \vec{w}_{fit} &= (w_1 \ , ..., w_k \ , ..., w_p) \ , \qquad (4.8) \\ \forall k \in \{1,...,p\} : w_k &= \frac{2\sqrt{\ln 2}}{\Delta\nu_G}\left(\frac{c}{\lambda_{spec,x_k}} - \frac{c}{\lambda_0}\right) \ , \\ \vec{i}_{fit} &= \left(i_{fit,x_1} \ , ..., i_{fit,x_k} \ , ..., i_{fit,x_p}\right) \ , \qquad (4.9) \end{aligned}$$

where

$$\Delta\nu_G = \sqrt{\Delta\nu^2_{Doppler} + \Delta\nu^2_{Instr,G}} \tag{4.10}$$

is the width of the profile resulting from the convolution of the Doppler profile with the Gaussian part of the instrumental profile. Using an estimated neutral temperature of $T = 2\,\mathrm{eV}$, $\Delta\nu_G$ is treated as a known quantity.

The final fit will be performed in frequency space, with an *abscissa* scaled by the Gaussian width units. By construction, the line center has the coordinate $w = 0$. The analysis interval can be chosen to be symmetric since the effect of neighboring impurity lines will be suppressed by the algorithm of the fitting method, as will be shown in chapter 5. In addition, an analysis interval symmetrically centered around the line peak will allow an improved fit to the wings of the line shape.

The numerical fitting routine used is discussed in Ref. [3, chapter 11]. It performs a non-linear least squares fit to a function of an arbitrary number of parameters. The function may be any non-linear function. The routine has to be provided with three vectors: two vectors for *abscissa* and corresponding *ordinate* values, as well as a vector $\vec{W}$ specifying a relative weight for each data point within the fit. The functional form to be fitted is given by equation 3.43:

$$\begin{aligned} F^{Zeeman}(\vec{V}, w, \Delta w_{Zeeman}) \;=\; & \frac{1}{2} V_1 \,\mathrm{Voigt}\,(V_0, w) \\ & + \frac{1}{4} V_1 \,\mathrm{Voigt}\,(V_0, w - \frac{1}{2}\Delta w_{Zeeman}) \\ & + \frac{1}{4} V_1 \,\mathrm{Voigt}\,(V_0, w + \frac{1}{2}\Delta w_{Zeeman}) + V_2 + V_3\, w\,. \end{aligned}$$

For each discharge, the magnetic field measured as a function of time is retrieved from the database. Knowing the magnetic field at a specific point within the divertor for all times, the Zeeman splitting in w-space can be calculated by using equation 3.42.

The fitting routine returns the vector $\vec{V}$. The value needed for the calculation of densities is the form parameter V_0. In order to perform the fit, initial guesses for the elements of $\vec{V}$ have to be provided. These are taken to be

$$\vec{V}^{init} = \left(1.4,\; G_0,\; G_3 + G_4 \cdot G_1 + G_5 \cdot G_1^2,\; 0\right)\,. \tag{4.11}$$

In the initial fit, all data points are taken to have an equal relative weight by choosing $\vec{W} = (1, ..., 1)$. As a result of the initial fit, the parameters $\vec{V}^{j=1}$ are returned.

Based on the results of an iteration j, the weighting of the data points is changed in a way to be described below. Using the parameters returned by the fit j as a guess, the fit is iterated on the basis of the same set of data points, returning the parameters $\vec{V}^{j+1}$ as a result. This procedure is iterated up to 20 times, unless the parameter V_0 converges before that number of iterations is reached. The iteration is considered to have converged when $V_0^j = V_0^{j+1}$ is true to within an accuracy of $\frac{1}{1000}$.

Based on the curve $F^{Zeeman}(\vec{V}^j, w, \Delta w_{Zeeman})$, the weighting for the iteration $j+1$ is calculated as follows:

$$\forall k \in \{1, ..., p\}: \tag{4.12}$$

$$F^{Zeeman}(\vec{V}^j, w_k, \Delta w_{Zeeman}) \leq i_{x_k}:$$

$$W_k = \exp\left[-9\left(\frac{F^{Zeeman}(\vec{V}^j, w_k, \Delta w_{Zeeman}) - i_{x_k}}{F^{Zeeman}(\vec{V}^j, w_k, \Delta w_{Zeeman}) - (G_3 + G_4 \cdot G_1 + G_5 \cdot G_1^2)}\right)^2\right]$$

$$F^{Zeeman}(\vec{V}^j, w_k, \Delta w_{Zeeman}) > i_{x_k}: \; W_k = 1$$

The influence of a particular data point (w_k, i_{x_k}) increases with its weight W_k. The above weight distribution is a result of several numerical tests comparing the desired fit with its actual form.

In the above attribution of weights to data points, the relative influence of all data points which lie below or exactly on the numerically fitted curve — given by $F^{Zeeman}(\vec{V}^j, w_k, \Delta w_{Zeeman})$ — will be equal to its maximum for the next iteration of the fit. The influence of all data points which lie above the numerically fitted curve is decreased exponentially with their distance from the numerical fit relative to the distance of the numerical fit from the background as obtained from the Gaussian fit. By construction, the weight attributed to a data point is a *continuous* function of its distance from the numerical fit at that position in w-space. In addition, no data point is ever disregarded completely.

The physical reason for manipulating the relative weights of the data points in order to obtain a final numerical fit is found as follows: we need to find a numerical fit which represents the width of the deuterium transition best. The impurity transitions surrounding the deuterium line will always distort the line shape by *adding* to the count rates in certain regions of w-space. These impurities are only sometimes observable whereas the deuterium lines can always be found in the spectrum. By attributing the highest influence to data points which lie below or exactly on the numerical fit, one can ensure that those data points have the highest influence on the result of the fit which are solely due to the deuterium transition.

Although these arguments are generally valid, the presented method is only func-

tional when the center of the deuterium transition is precisely determined for the data; this requirement is only met if there are no dominant impurity transitions present in the interval I_{max} defined in equation 4.1.

4.2 Rejection Criteria

This section summarizes all the criteria used in the analysis software to reject measured spectral line shapes which are not appropriate for the determination of electron densities. The completeness of the corresponding rejection criteria for data sets ensures that an automation of the analysis is possible.

The following text lists a number of criteria. If any of these criteria is fulfilled for a particular transition at a particular time in a specific discharge, no density data for this particular transition will be recorded in the database. This set of conditions is the outcome of empirical tests.

If the standard deviation of the raw data is too small, no transition is observed: the data are too *flat*.

Rejection Criterion 4.2.1 (Standard Deviation)

$$\frac{1}{\frac{1}{p}\sum_{k=1}^{p} i_{x_k}} \sqrt{\frac{\sum_{k=1}^{p} \left(i_{x_k} - \frac{1}{p}\sum_{k=1}^{p} i_{x_k} \right)^2}{p}} < 0.04$$

The analysis program calculates how far the wavelength determined for a particular transition is shifted from its actual value. Data sets for which this shift lies substantially beyond the error limits of the wavelength calibration are rejected.

Rejection Criterion 4.2.2 (Absolute Wavelength Calibration)

$$|G_1 - \lambda_0| > 3\,\mathrm{nm}$$

One discards data with low ratios of the signal to the underlying noise. This sorting process already starts after the preliminary Gaussian fit. Three restrictions are imposed on the data sets, regarding their absolute peak height, their peak height relative to the background, and their maximum number of counts. For the current operating temperature of the detector, the dark charge count rate is about 120 counts per data acquisition cycle ($\sim 45\,\mathrm{ms}$).

Rejection Criterion 4.2.3 (Peak Height of Preliminary Fit) $G_0 < 20$

Rejection Criterion 4.2.4 (Relative Peak Height)

$$\frac{G_0}{G_3 + G_4 \cdot G_1 + G_5 \cdot G_1^2} < 0.04$$

Rejection Criterion 4.2.5 (Maximum Count Number in a Single Bin)

$$\max\left(\{i_{x_1}, ..., i_{x_n}\}\right) < 160$$

Whenever the fit to the Voigt profile diverges, the data set can obviously not be used for a density calculation.

Rejection Criterion 4.2.6 (Divergence of Voigt Fit) *The fit to the Voigt profile diverges: the form parameter V_0 is infinite or zero, the scale V_1 becomes infinite or negative, the constant background term V_2 diverges, or the linear term V_3 diverges.*

Some fits to the Voigt profile resemble the data points near the peak very well, but the wings of the fit do not match the data. If the constant term drops well below the number of counts due to the dark charge, the data set is rejected.

Rejection Criterion 4.2.7 (Dark Background) $V_2 < 100$

In the chapter dealing with the error analysis of this fitting procedure, a routine calculating the *maximal* inaccuracy due to the data scatter in the wavelength direction will be introduced. Its result $r_{\delta\lambda}$ indicates what the maximal error of the density calculation would be. It is calculated on the basis of the fitted profile and the data set.

Rejection Criterion 4.2.8 ($\delta\lambda$ Scatter) $r_{\delta\lambda} > 1.5$

In some cases of very low electron densities, the result for the total measured Lorentzian width $\Delta\lambda_L$ turns out to be very close to the expected instrumental contribution to the Lorentzian width. These cases cannot be used to calculate an electron density since the uncertainty of the measurement would be too large.

Rejection Criterion 4.2.9 (Dominating Instrumental Contribution)

$$\Delta\lambda_L < 1.1 \cdot \Delta\lambda_{Instr,L,grating}$$

4.3 Calculating the Electron Density from the Spectral Line Fits

The fit of the theoretically predicted profile $F^{Zeeman}(\vec{V}, w, \Delta w_{Zeeman})$ to the measured spectra requires a knowledge of both the underlying magnetic field strength and the temperature of the emitting deuterium atoms. Both parameters are fixed and are not allowed to vary during the least squares fit.

The temperature estimate together with the knowledge of the instrumental line shape leads to a knowledge of the expected total Gaussian width $\Delta\nu_G$. The toroidal magnetic field $B_{toroidal}$ is known for all discharges as a function of time. In order to calculate the magnitude B of the magnetic field, the approximation

$$B = \left|\vec{B}\right| \approx |B_{toroidal}| \tag{4.13}$$

is used, which leads to errors of less than 3%.

The fitting routine returns the vector $\vec{V}$. For the calculation of electron densities, one only needs the shape parameter $a = V_0$. The Lorentzian width due to Stark broadening can then be calculated as

$$\Delta\lambda_{Stark} = \frac{a\,\Delta\lambda_G}{\sqrt{\ln 2}} - \Delta\lambda_{Instr,L,grating}\,. \tag{4.14}$$

From this width $\Delta\lambda_{Stark}$ in wavelength space, the underlying electron density is derived using equation 3.24.

Chapter 5

Error Analysis

This chapter will try to quantify some of the uncertainties of the electron density measurement performed. The uncertainties dealt with here have three different origins: approximations made in the theory underlying the analysis, the statistical nature of the count spectra, and a non-homogeneous plasma.

The effects discussed will include the neutral temperature dependence of the line shape, as well as line shape distortions due to nearby lines from impurities. In addition, it is examined whether it is appropriate to calculate the electron density from only a single line, without taking its series neighbors into account. The results obtained from different line transitions are compared. Furthermore, the parameter $r_{\delta\lambda}$ is presented as a measure for the *maximal* inaccuracy of the result due to the deviations of the fits from the data in wavelength space. Also, the consequences of electron and neutral density gradients within the view of observation are discussed. An estimate of the measurement uncertainties is provided, based on the statistical characteristics of the line fits.

This chapter concludes with an attempt to estimate the *overall* uncertainty of the electron density measurements performed with the presented method. This estimate includes — in addition to the effects mentioned in the preceding paragraph — the uncertainty in the theoretical Stark widths, the uncertainty in the Lorentzian widths of the instrumental line shape, as well as the inaccuracy of the dispersion measurements.

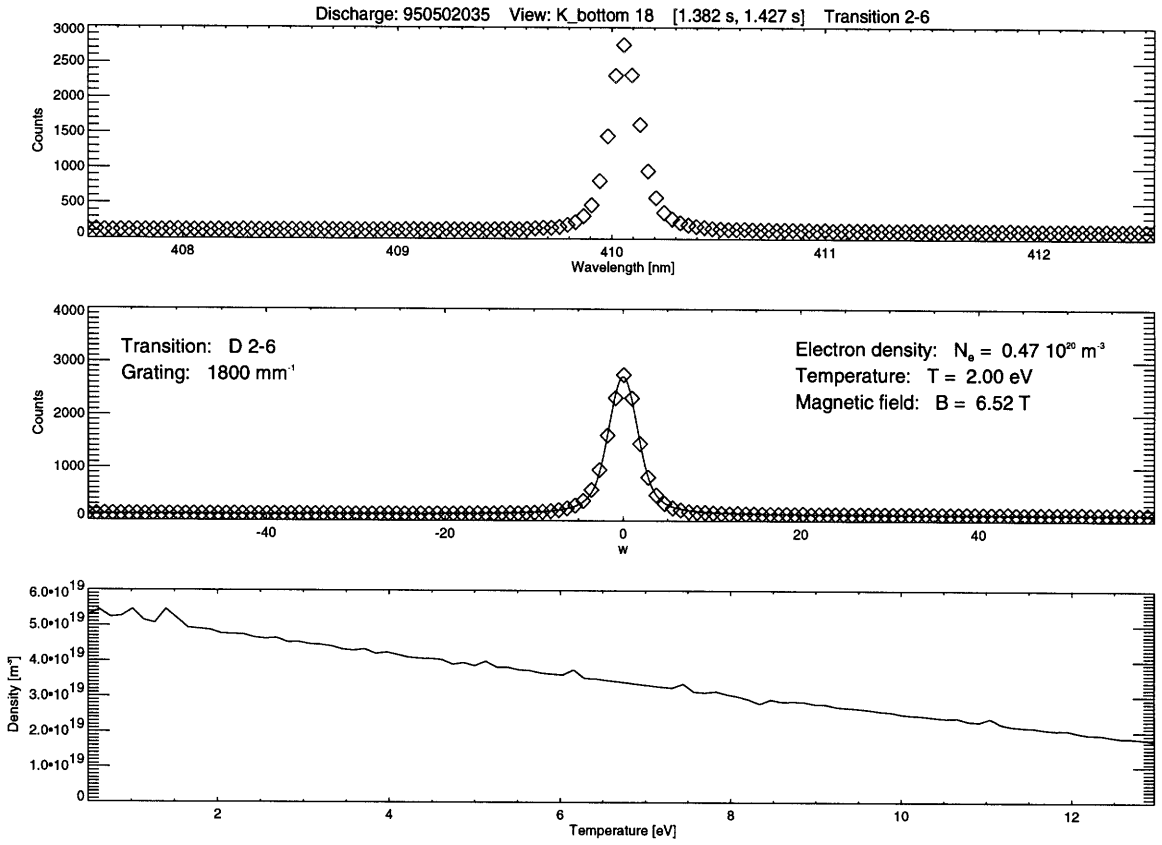

Figure 5-1: Case of a low electron density: neutral temperature dependence of the electron density calculation using the D_δ-transition. The upper graph shows the raw spectrum in wavelength space. The center graph shows the data and the curve fitted to it in w-space, assuming a neutral temperature of $T = 2\,\mathrm{eV}$. The lower graph shows the density calculated for this specific transition as a function of the neutral temperature used for the analysis.

5.1 Neutral Temperature Dependence

The calculation of electron densities from spectral line profiles must be corrected for the Doppler broadening which depends on the temperature of the emitting deuterium atoms. As argued in a previous chapter, a neutral temperature of $T = 2\,\mathrm{eV}$ will be used to calculate the electron densities. This section will exhibit the influence of neutral temperature on the result for the electron density.

Figures 5-1, 5-2, and 5-3 show spectral line profiles together with the theoretical profile $F^{Zeeman}(\vec{V}, w, \Delta w_{Zeeman})$, fitted to the data in w-space assuming $T = 2\,\mathrm{eV}$. The electron density is then recalculated for the same overall configuration, except that the underlying neutral temperature is changed within a broad range. The re-

sulting electron densities are then plotted as a function of neutral temperature.

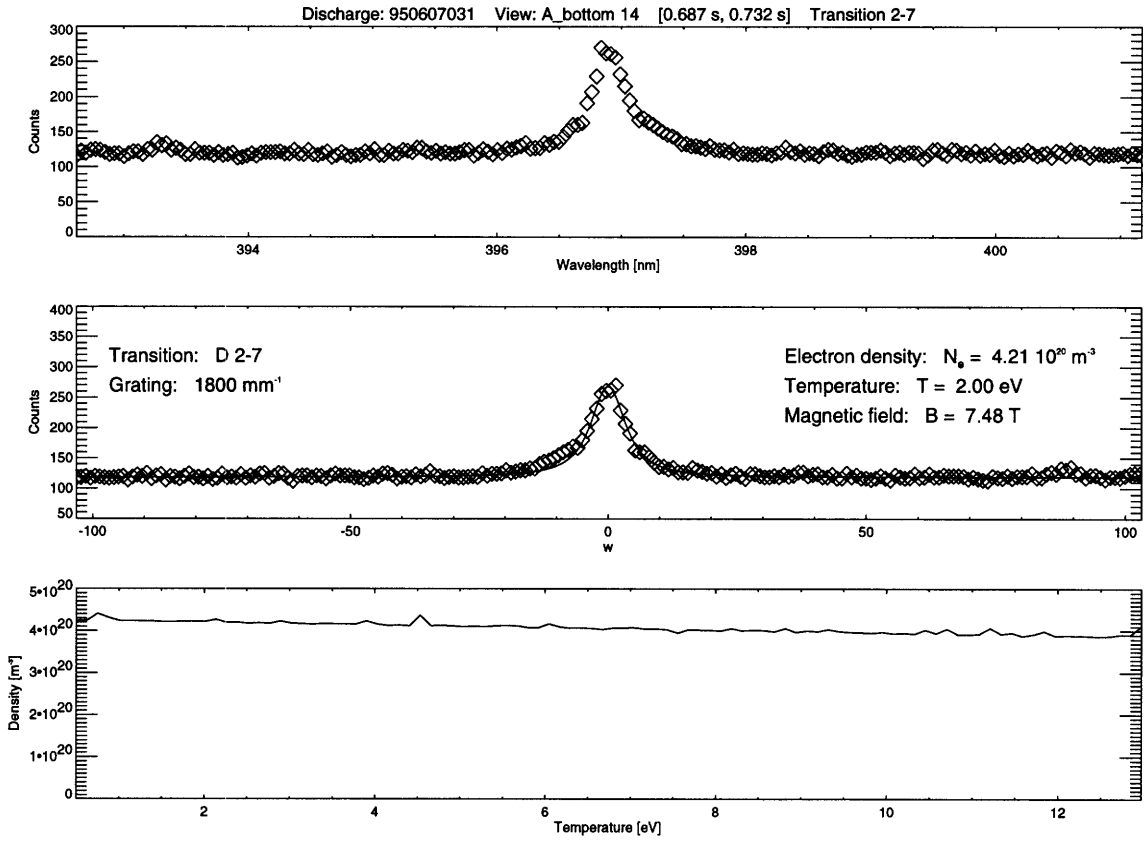

Figure 5-2: Case of an intermediate electron density: neutral temperature dependence of the electron density calculation using the D 2–7-transition. The upper graph shows the raw spectrum in wavelength space. The center graph shows the data and the curve fitted to it in w-space, assuming a neutral temperature of $T = 2\,\mathrm{eV}$. The lower graph shows the density calculated for this specific transition as a function of the neutral temperature used for the analysis.

The three figures mentioned cover the whole possible range of densities in the tokamak divertor. Fig. 5-1 shows an extreme low density case. As can be seen, the temperature dependence is almost linear with some scatter due to numerical inaccuracies combined with noise in the data. In the examined range of neutral temperatures $0.5\,\mathrm{eV} < T < 13\,\mathrm{eV}$, the calculational result for the electron density varies between $5.3 \cdot 10^{19}\,\mathrm{m}^{-3}$ and $1.8 \cdot 10^{19}\,\mathrm{m}^{-3}$. This strong variation with temperature shows that the Doppler broadening has become an effect comparable to Stark broadening. There are two causes for this situation: the low electron density which is equivalent to a small Stark width, and the fact that Fig. 5-1 shows a deuterium 2–6 transition for which the Stark widths are generally smaller than those for the Balmer transitions

with higher principal quantum numbers n.

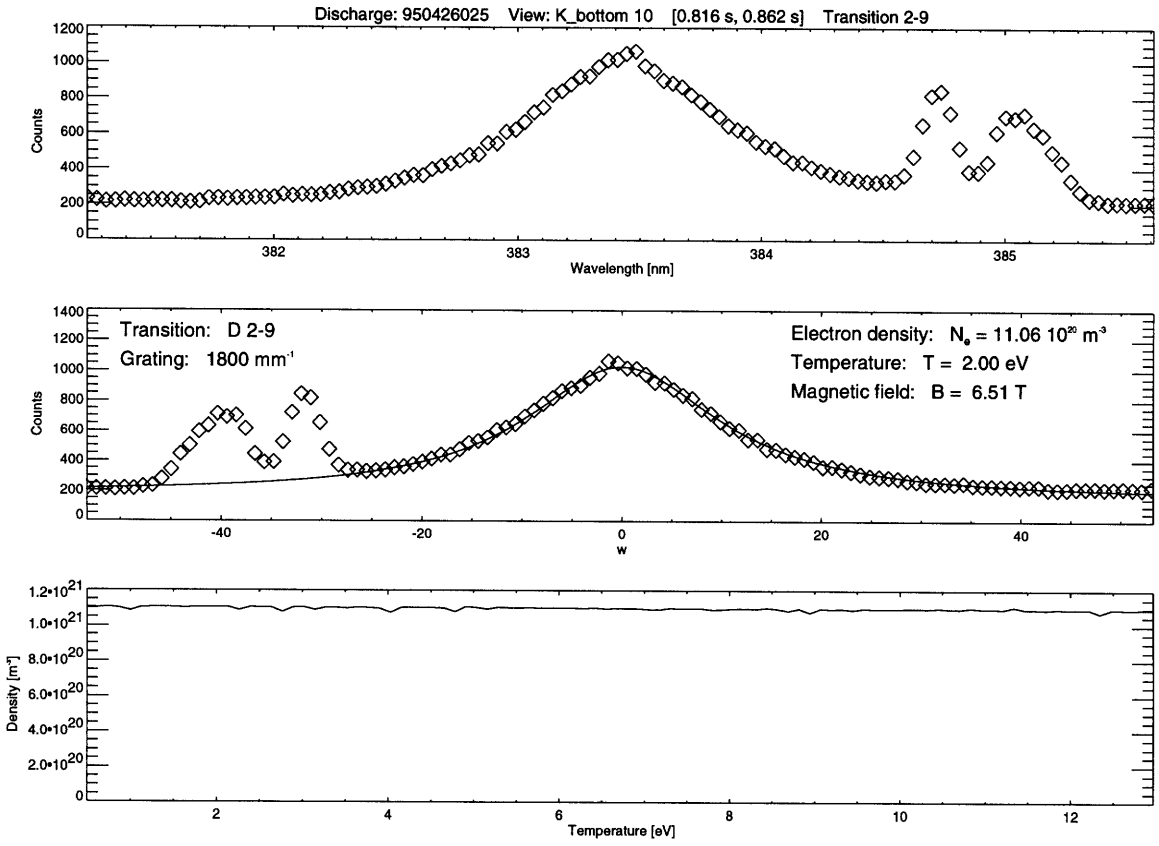

Figure 5-3: Case of a high electron density: neutral temperature dependence of the electron density calculation using the D 2–9-transition. The upper graph shows the raw spectrum in wavelength space. The center graph shows the data and the curve fitted to it in w-space, assuming a neutral temperature of $T = 2\,\mathrm{eV}$. The lower graph shows the density calculated for this specific transition as a function of the neutral temperature used for the analysis.

Figures 5-2 and 5-3 show the temperature dependence of the analysis for the cases of intermediate and high electron density. The intermediate density case is the one we will encounter during most discharges. The calculated electron density varies between $4.25 \cdot 10^{20}\,\mathrm{m}^{-3}$ and $3.9 \cdot 10^{20}\,\mathrm{m}^{-3}$ over the entire range of neutral temperatures that can be expected to occur. For the case of high electron densities shown in Fig. 5-3, the effect of temperature dependence is entirely negligible.

Result of Error Analysis 5.1.1 (Neutral Temperature Dependence) *For electron densities of order $N_e \approx 10^{20}\ m^{-3}$ and higher, the influence of the neutral temperature uncertainty on the electron density calculation becomes negligible.*

One conclusion to be drawn from this result is concerned with the numerical fitting procedure itself: the neutral temperature is not allowed to vary within the fit, it is *a priori* chosen and stays fixed. Figures 5-2 and 5-3 show that this approach is entirely justified and even necessary for the procedure to work properly: allowing the temperature to vary within the fitting routine could — in the case of an intermediate or high electron density — lead to a diverging temperature since there would be almost no dependence on this parameter. Fixing the neutral temperature thus prevents the routine from returning unphysical results.

In addition, a weak temperature dependence implies in almost all the cases of interest that even a substantial error in the estimate $T = 2\,\mathrm{eV}$ could not affect the calculated electron density substantially.

5.2 Impurity Lines

This section will demonstrate the properties of the fitting routine presented in chapter 4 regarding the influence of impurity lines surrounding the deuterium transition of interest. To be precise, it will be attempted to show that equation 4.12 is successful in reducing the influences of impurity effects in such a way that the fit of the theoretical line profile resembles only the deuterium transition, but not the impurity lines.

An example is shown in Fig. 5-4. The deuterium 2–9-transition is surrounded by several impurity lines, some of them surrounding the peak and some situated close to the center of the peak. The graph shows that the fit clearly follows the deuterium transition, not taking the impurities into account at all.

Another example of a deuterium line surrounded by impurity lines is given in Fig. 5-5. It shows the deuterium 2–8-transition, extracted from the same measured spectrum as Fig. 5-4. It is obvious that the fit to the 2–8-transition is distorted by the impurity effects. The fit is centered at the strong impurity transition close to the center of the 2–8-transition. For that reason, the width of the fit is far smaller than the actual width of the 2–8-transition. The reason for this deviation is found in the fact that a high count rate due to an impurity line is located within the interval

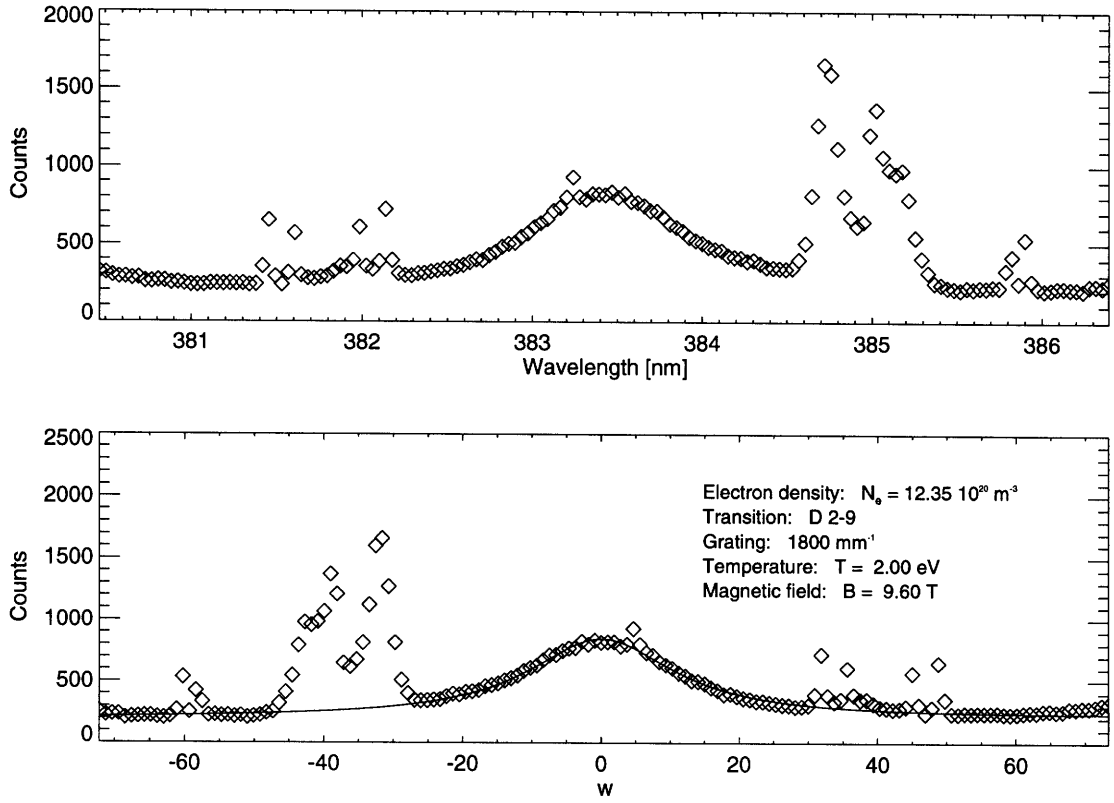

Figure 5-4: The upper graph shows the raw spectrum of the D 2–9-transition in wavelength space. The lower graph shows the same spectrum in w-space, together with the theoretical profile fitted to it. The numerical fit resembles the deuterium transition only, a distortion due to the impurities cannot be seen. The presented data are taken from time frame [0.906 s, 0.951 s] and view K_{bottom} 14 in discharge 950609011.

I_{max} defined in equation 4.1. As a result, the electron density calculated from the 2–8-transition is $N_e = 6.10 \cdot 10^{20}\,\mathrm{m}^{-3}$, about half the value calculated from the 2–9-transition.

Result of Error Analysis 5.2.1 (Impurity Line Effects) *As long as the interval* $[\lambda_0 - \Delta\lambda_{left}, \lambda_0 + \Delta\lambda_{right}]$ *surrounding a deuterium Balmer series transition at* λ_0 *is not strongly affected by impurity lines, the fit of the theoretical shape function* $F^{Zeeman}(\vec{V}, w, \Delta w_{Zeeman})$ *to the data will not be affected by the impurity lines either. (See equation 4.1 for a more detailed specification of the interval.)*

In order to separate acceptable fits from the ones to be rejected, one therefore has to rely on another rejection criterion for the numerical fits. This criterion, presented later in this chapter, will be provided by the calculation of the quantity $r_{\delta\lambda}$,

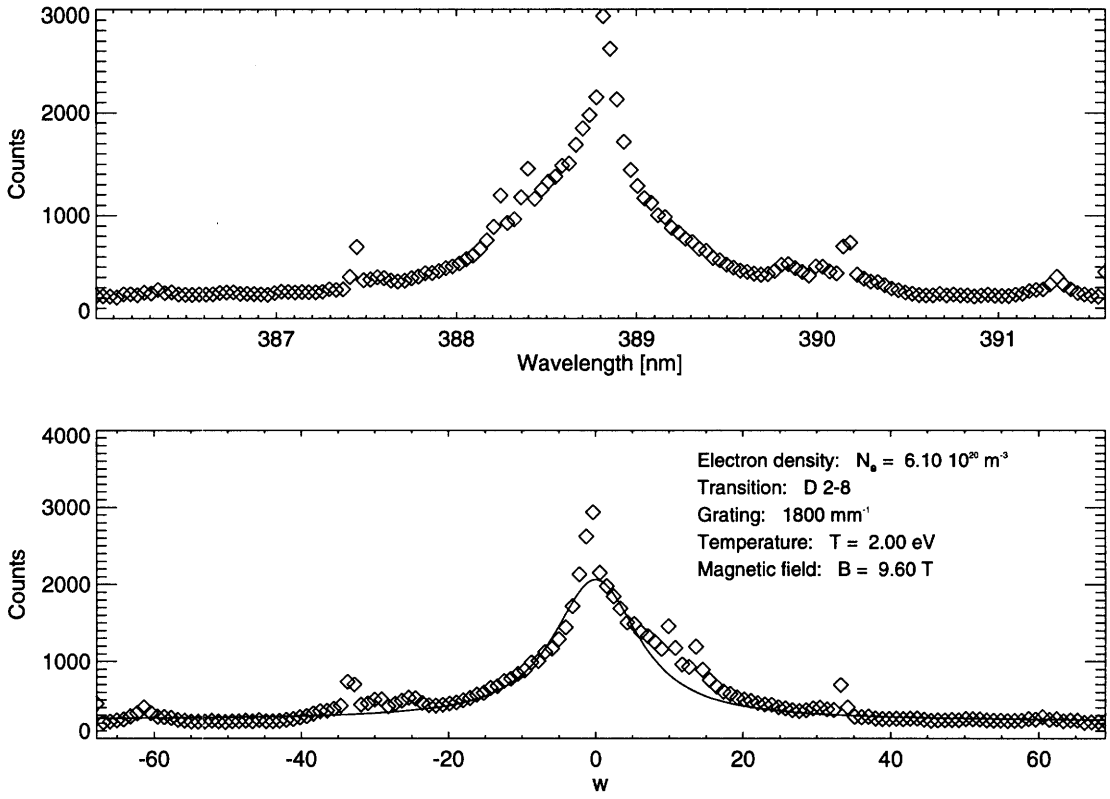

Figure 5-5: The upper graph shows the raw spectrum of the D 2–8-transition in wavelength space. The lower graph shows the same spectrum in w-space, together with the theoretical profile fitted to it. The numerical fit is clearly distorted by the impurity effects. The presented data are taken from time frame [0.906 s, 0.951 s] and view K_{bottom} 14 in discharge 950609011.

which indicates the maximal inaccuracy of the electron density due to data scatter in wavelength space.

5.3 Neighboring Balmer Series Lines

The analysis routine is constructed to use a single deuterium transition in the Balmer series to calculate the underlying electron density. The series neighbors of the transition of interest are not taken into account, implying that they cannot affect the result of the analysis. It is the aim of this section to examine this hypothesis.

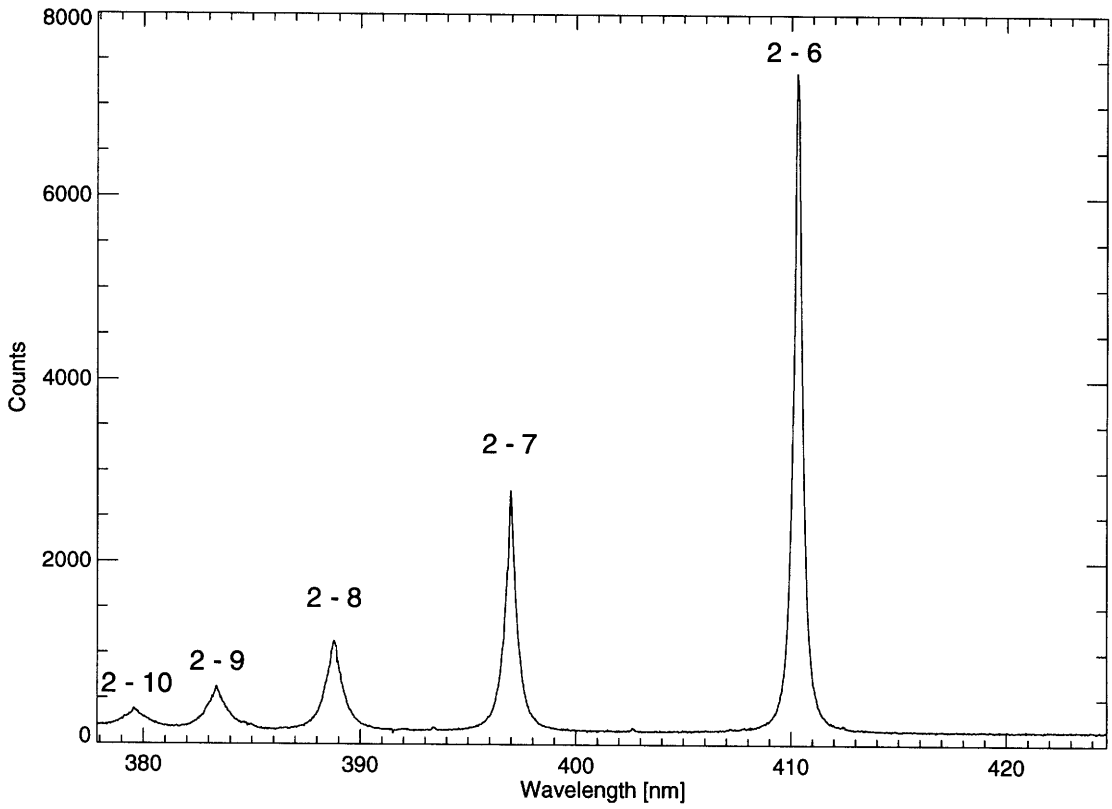

Figure 5-6: A strongly Stark broadened deuterium spectrum without impurity effects, shown in wavelength space. The different transitions from the Balmer series of deuterium are indicated. The data were observed with fiber A_{bottom} 16 during time frame [0.994 s, 1.039 s] in discharge 950509022.

5.3.1 Fitting Single Transitions Separately

In order to test whether the existence of neighboring lines in the Balmer series can affect the results of the analysis routine outlined in chapter 4, one needs to look at a set of data satisfying certain conditions:

- If there is any interaction between multiple transitions affecting the calculational result for the electron density, this effect would be most apparent in the case of a high electron density. Therefore, a spectrum exhibiting high electron densities should be chosen for the analysis.

- The data set to be examined should be as free from impurities as possible in order to separate different effects.

- As many series transitions as possible should be present within the spectrum.

A spectrum which satisfies all these criteria is presented in Fig. 5-6. The standard analysis applied to this data set returns the numerical results given in Table 5.1.

Transition	Form	Scale	Offset	Linear Term	$\Delta\lambda_{Stark}$ [Å]	N_e [10^{21} m^{-3}]
2 – 6	4.96	65119	132.4	-0.0079	3.778	1.01
2 – 7	6.69	29329	139.9	0.0202	5.166	1.19
2 – 8	9.92	16662	139.8	0.0260	7.788	1.16
2 – 9	12.05	8941	159.5	0.0296	9.501	1.16
2 – 10	13.45	4205	180.0	0.0930	10.619	0.89

Table 5.1: The results returned by the analysis routine for the spectrum shown in Fig. 5-6. The form parameter denotes V_0. The scale refers to V_1 [counts]. The offset represents the constant background given by V_2 [counts]. The linear term refers to V_3 [counts / unit in w-space]. Note that the external magnetic field was given by $B = 5.88\,\mathrm{T}$. The temperature was assumed to be $T = 2\,\mathrm{eV}$.

The energy levels of the series converge at the series limit D 2–∞. The number of states per unit frequency interval increases monotonically as the distance to the series limit decreases. For that reason, the constant term V_0 should increase monotonically with the principal quantum number n of the transition. The data for the transitions D 2–6, ..., 2–10 presented in Table 5.1 do indeed exhibit this behavior. Due to the same phenomenon, the linear variation of the transition background around the center of each single line in frequency space has to be non-negative: $V_1 \geq 0$. This condition is satisfied by all transitions present in the spectrum, except for D 2–6.

It is also expected that the separate analysis of all transitions leads to comparable results for the electron density. In the data set discussed, the density derived from the transition D 2–10 lies far off the value derived from the other transitions. The results for the other transitions center around a value of $N_e = 1.13 \cdot 10^{21}\,\mathrm{m}^{-3}$ with a maximal deviation of 10%.

Another effect to be considered here is the depression of series limits, as discussed in Ref. [9]. The separation between levels decreases with increasing principal quantum number n. Given the Stark broadening of the series members, the states will eventually merge into a continuum for energies below the series limit. The lowest energy of this continuum is referred to as the *Inglis-Teller limit*. The principal quantum

number n_{max} of the last term observed in the series will be given by

$$N_i \, n_{max}^{15/2} = 0.027 \, {a_0}^{-3} \, , \tag{5.1}$$

where a_0 is the Bohr radius and N_i the ion density. For $N_i \approx N_e = 1.1 \cdot 10^{21} \, \mathrm{m}^{-3}$, one finds $n_{max} = 12.47$.

From the part of the spectrum measured, it cannot be decided where the onset of the continuum lies. Among the transitions observed, the 2–10-transition will in any case be the transition which is most affected by the depression of the series limit, an effect which might lead to a distortion of its line shape and which could expain the low result for the electron density derived from the line shape of this transition.

5.3.2 Fitting Multiple Transitions Simultaneously

It has to be examined whether neighboring series transitions affect the density calculation from a single transition. The deciding criterion will be based on the result returned by a routine that performs a numerical fit of multiple lines in the spectrum. The routine will be applied to the spectrum presented in Fig. 5-6.

The routine fits the theoretical function $F^{spec}\left(\vec{V}^{spec}, \vec{\lambda}_{center,cal}\, , \lambda\right)$ to the entire spectrum in wavelength space. The function is given by

$$\begin{aligned} & F^{spec}\left(\vec{V}^{spec}, \vec{\lambda}_{center,cal}\, , \lambda\right) \\ & \quad = \sum_{n=6}^{10} F^{Zeeman}\left((a_{2-n}, V_{1,2-n}, 0, 0), w_{2-n}, \Delta w_{Zeeman,2-n}\right) \\ & \qquad + V_{2,spec} + V_{3,spec}\left[\lambda - \frac{1}{2}(\lambda_{center,cal,2-6} + \lambda_{center,cal,2-10})\right] \, , \end{aligned} \tag{5.2}$$

where

$$\vec{V}^{spec} = (V_{1,2-6}, \ldots, V_{1,2-10}, V_{2,spec}, V_{3,spec}, N_{e,spec}) \tag{5.3}$$

is the vector which contains the free parameters of the fit. $V_{1,2-n}$ denotes the multiplicative scale for the 2–n-transition. The result returned from the fit to the single transition 2–n is used as an initial estimate for this parameter. $V_{2,spec}$ is an overall constant. Its initial estimate is given by

$$V_{2,spec} = \frac{1}{2}\left(V_{2,2-6} + V_{2,2-10}\right) \, , \tag{5.4}$$

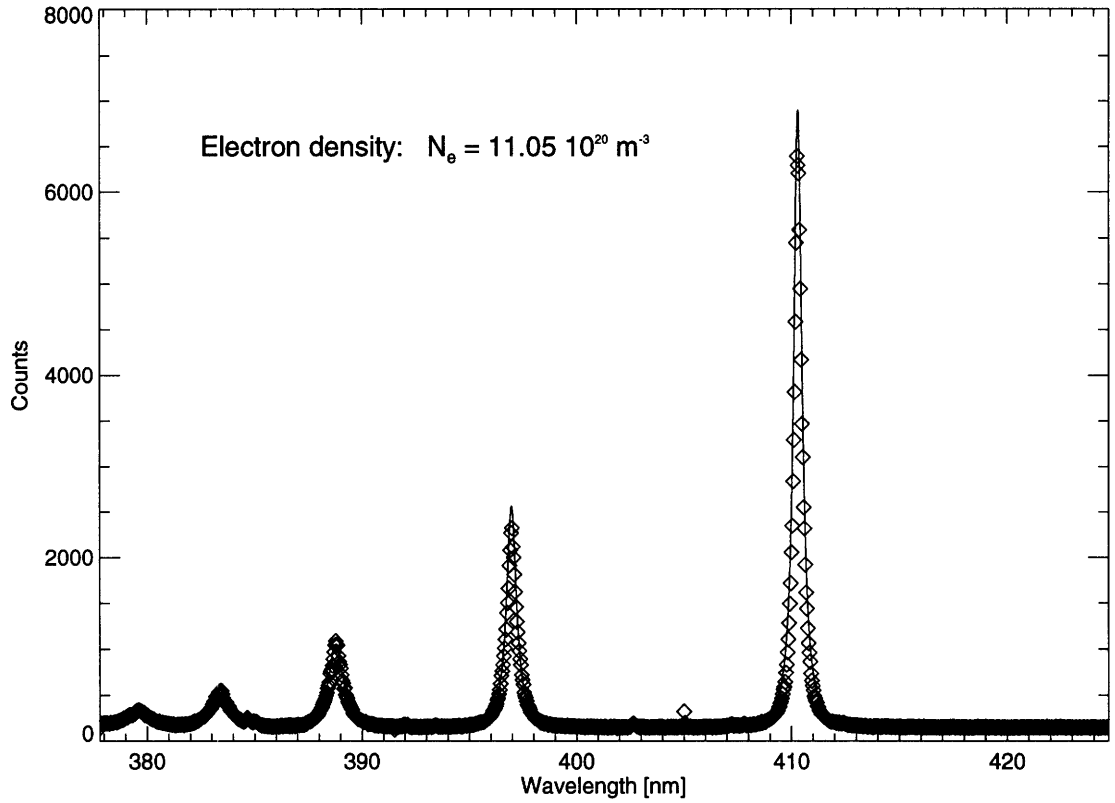

Figure 5-7: The diamonds show the spectrum already presented in Fig. 5-6. The solid line shows the result of a consistent theoretical fit to the data points. The parameters returned by the fitting routine are given in Table 5.2.

again using the results from the single fits. Similarly, the initial estimate for the linear term is taken to be

$$V_{3,spec} = \frac{V_{2,2-6} - V_{2,2-10}}{\lambda_{center,cal,2-6} - \lambda_{center,cal,2-10}} \ . \tag{5.5}$$

The electron density $N_{e,spec}$ will be used to calculate the Stark widths of all deuterium transitions in the spectrum consistently. Its initial estimate is the average of the densities obtained from the fits to the transitions 2–6, ..., 2–9.

The variable a_{2-n} denotes the form parameter of the spectral Voigt profile for the transition 2–n, calculated for a given electron density of $N_{e,spec}$, including Doppler, Stark, and instrumental effects in the way described in chapter 3 and section 4.3. The quantity $\Delta w_{Zeeman,2-n}$ is the energy splitting in w-space for the 2–n transition, as calculated for the single fits in equation 3.42. The vector

$$\vec{\lambda}_{center,cal} = (\lambda_{center,cal,2-6}\ , \ldots , \lambda_{center,cal,2-10}) \tag{5.6}$$

Transition	$\lambda_{center,cal}$ [nm]	Scale	Offset	Linear Term	$N_{e,spec}$ [10^{21} m^{-3}]
2 – 6	410.31	65661	135.8	-1.437	1.105
2 – 7	396.97	28201			
2 – 8	388.78	15734			
2 – 9	383.34	8498			
2 – 10	379.58	4963			

Table 5.2: The results obtained by performing a consistent overall fit to the entire spectrum shown in Fig. 5-6. $\lambda_{center,cal}$ denotes the wavelength of the center of the transition, according to the wavelength calibration. The scale refers to $V_{1,2-n}$ [counts]. The offset represents the constant background given by $V_{2,spec}$ [counts]. The linear term refers to $V_{3,spec}$ [counts / nm]. $N_{e,spec}$ is the electron density that is consistently used to resemble the Stark widths for all the transitions in the spectrum. Note that the external magnetic field was given by $B = 5.88\,\mathrm{T}$. The neutral temperature was assumed to be $T = 2\,\mathrm{eV}$.

contains the centers of the deuterium transitions present in the spectrum, determined during the single fit processes and based on the wavelength calibration. These values are kept fixed during the fit of multiple transitions.

The weighting for the different data points will be determined similar to equation 4.12 used for the single fits. Let m be the number of data points that describe the spectrum. It is then assumed that the experimental spectral data points are given by the vectors

$$\vec{\lambda} = (\lambda_1, \ldots, \lambda_k, \ldots, \lambda_m)\,, \tag{5.7}$$

$$\vec{i} = (i_1, \ldots, i_k, \ldots, i_m)\,, \tag{5.8}$$

and that the values calculated from the theoretical fit function based on the initial estimate parameters are given by the vector

$$\vec{F} = (F_1, \ldots, F_k, \ldots, F_m)\,. \tag{5.9}$$

The weight vector $\vec{W}$ used by the least squares fit routine is calculated as follows:

$$\forall k \in \{1, ..., m\}: \tag{5.10}$$

$$F_k \leq i_k:$$

$$W_k = \exp\left[-9\left(\frac{F_k - i_k}{F_k - b_{\lambda_k}}\right)^2\right]$$

$$\text{with } b_{\lambda_k} = V_{2,spec} + V_{3,spec}\left(\lambda_k - \frac{1}{2}(\lambda_{center,cal,2-6} + \lambda_{center,cal,2-10})\right)$$

$$F_k > i_k:\ W_k = 1\,.$$

This weighting ensures a suppression of impurity effects on the multiple line fit. Since the initial estimates of the multiple fit parameters are based on the final results for the single fits, the fitting routine converges after only one iteration.

The result of the multiple transition fit is graphed in Fig. 5-7. The numerical values are presented in Table 5.2. The overall result of $N_{e,spec} = 1.11 \cdot 10^{21}\,\mathrm{m}^{-3}$ lies remarkably close to the average of the electron densities calculated separately from the transitions 2–6, ..., 2–9.

Result of Error Analysis 5.3.1 (Neighboring Series Transitions) *The electron densities calculated from the separate deuterium transitions 2–6, ..., 2–9 lie close to the electron density calculated from consistently fitting the whole spectrum containing the transitions 2–6, ..., 2–10. This implies that the effects due to series neighbors only affect the electron density calculations negligibly. From comparisons of the separate electron density calculations, it becomes apparent that the results for the 2–10-transition are less reliable.*

5.4 Data Scatter in Wavelength Space

This section introduces a rejection criterion for the theoretical fit, based on an estimate for the maximal uncertainty due to data scatter in wavelength space around the numerical fit.

For this section, it is assumed that the three vectors containing the data

$$\begin{aligned} \vec{i}_{fit} &= \left(i_{fit,x_1}, ..., i_{fit,x_k}, ..., i_{fit,x_p}\right) , \\ \vec{w}_{fit} &= \left(w_1, ..., w_k, ..., w_p\right) , \\ \vec{\lambda}_{fit} &= \left(\lambda_{spec,x_1}, ..., \lambda_{spec,x_k}, ..., \lambda_{spec,x_p}\right) , \end{aligned}$$

are given. The precise definition of these vectors is provided by equations 4.7–4.9.

In addition, it is assumed that the numerical fit has been performed successfully and that the theoretical profile $F^{Zeeman}(\vec{V}, w, \Delta w_{Zeeman})$ has been obtained, as well as the final vector of weights calculated from 4.12:

$$\vec{W} = (W_1, \ldots, W_k, \ldots, W_p) \ . \tag{5.11}$$

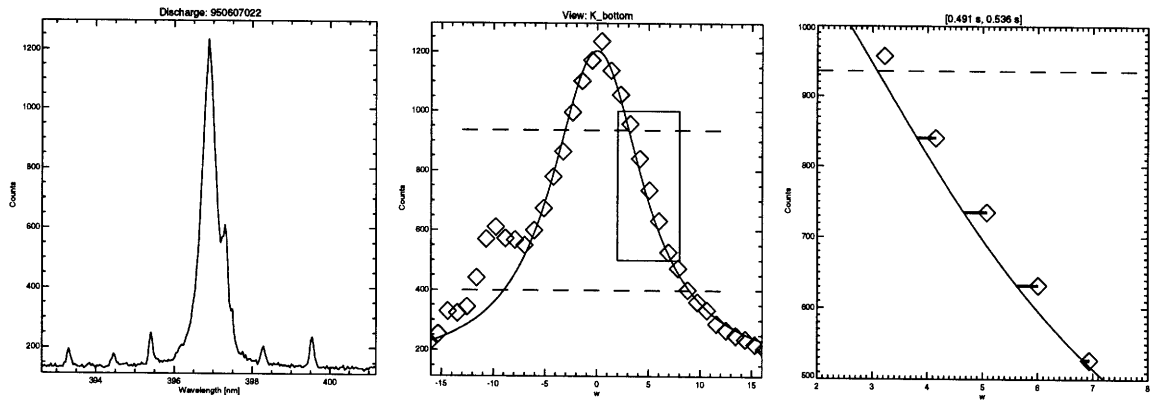

Figure 5-8: The calculation of the variable $r_{\delta\lambda}$ used as a rejection criterion. The graph to the left shows the raw data within the interval I_{fit} (see equation 4.6) in wavelength space. The center graph shows the numerical fit (solid line) to the raw data points (diamonds) close to the center of the line in w-space. The two horizontal lines indicate the restriction imposed by 5.12. The solid rectangle encloses the region which is shown in the graph to the right. The graph to the right shows the numerical fit (solid line) to the raw data (diamonds) in a small portion of w-space. The lengths of the thick horizontal lines between the numerical fit and the raw data points are elements of the vector $\vec{\chi}$ in equation 5.22.

For the given purposes, the set of data points is restricted to those points which lie between the $\frac{1}{4}$- and the $\frac{3}{4}$-intensity points. This is done by requiring

$$i_{fit,x_k} \in \left[i_{min} + \frac{1}{4}\left(i_{max} - i_{min}\right),\, i_{min} + \frac{3}{4}\left(i_{max} - i_{min}\right) \right] , \tag{5.12}$$

where

$$i_{min} = \min\left\{ i_{fit,x_1}, ..., i_{fit,x_k}, ..., i_{fit,x_p} \right\} , \tag{5.13}$$

$$i_{max} = \max\left\{ i_{fit,x_1}, ..., i_{fit,x_k}, ..., i_{fit,x_p} \right\} . \tag{5.14}$$

This requirement is graphically illustrated in Fig. 5-8. The resulting subset of data points will be denoted by the vectors

$$\vec{i}_{peak} = \left(i_{peak,1}, \ldots, i_{peak,l}, \ldots, i_{peak,q}\right) , \tag{5.15}$$

$$\vec{w}_{peak} = \left(w_{peak,1}, \ldots, w_{peak,l}, \ldots, w_{peak,q}\right) , \tag{5.16}$$

$$\vec{\lambda}_{peak} = \left(\lambda_{peak,1}, \ldots, \lambda_{peak,l}, \ldots, \lambda_{peak,q}\right) , \tag{5.17}$$

$$\vec{W}_{peak} = \left(W_{peak,1}, \ldots, W_{peak,l}, \ldots, W_{peak,q}\right) , \tag{5.18}$$

with $q \leq p$, p and q positive non-zero integers. It is intended to calculate the deviation of the data points from the fit *in wavelength space*. First, one calculates this deviation

in w-space, as illustrated in the right graph in Fig. 5-8. For each data point at $w_{peak,l}$ on the w-axis, one can find a coordinate w'_l such that the following conditions are both met:

$$i_{peak,l} = F^{Zeeman}(\vec{V}, w'_l, \Delta w_{Zeeman}) , \tag{5.19}$$

$$|w'_l - w_{peak,l}| \quad \text{is minimal} . \tag{5.20}$$

These conditions ensure that w'_l is the point closest to $w_{peak,l}$ at which the value of the numerical fit is equal to the value of the raw data count rate at $w_{peak,l}$. One can then calculate the vector

$$\vec{\chi} = (\chi_1, \ldots, \chi_l, \ldots, \chi_q) , \tag{5.21}$$

$$\chi_l = w_{peak,l} - w'_l . \tag{5.22}$$

The variable

$$\sigma_w = \sqrt{\frac{\sum_{l=1}^{q} {\chi_l}^2}{m}} \tag{5.23}$$

will then quantify the scatter of the data around the fit in w space. From the overall Gaussian width $\Delta\nu_{Gauss}$ underlying the fit, the scatter in wavelength space is calculated to be

$$\sigma_\lambda = \frac{{\lambda_0}^2}{c} \Delta\nu_{Gauss} \frac{\sigma_w}{\sqrt{\ln 2}} . \tag{5.24}$$

From σ_λ, the *maximal* uncertainty of the electron density calculation can be calculated.

The variable σ_λ quantifies how far the data points deviate in the wavelength dimension from the numerical fit. In the case of maximal error, the full Stark width $\Delta\lambda_{Stark}$ was misfitted by an amount of $\pm 2\sigma_\lambda$. Based on the parameters of the fit, the Stark width $\Delta\lambda_{Stark}$ is calculated as described in section 4.3. Using equation 3.24, the electron density $N_e(\Delta\lambda_{Stark})$ can be derived. The maximal relative uncertainty in electron density due to scatter in wavelength space can thus be quantified by

$$r_{\delta\lambda} = \frac{N_e(\Delta\lambda_{Stark} + 2\sigma_\lambda)}{N_e(\Delta\lambda_{Stark})} . \tag{5.25}$$

The quantity $r_{\delta\lambda}$ is used to decide whether a specific fit is acceptable. $r_{\delta\lambda}$ does not provide a good indication how large the physical uncertainty actually is since

the calculation of $r_{\delta\lambda}$ itself is aimed at finding the *maximal* uncertainty in electron density due to data scatter in wavelength space. As a consequence, calculating the *actual* physical uncertainty from $r_{\delta\lambda}$ would invariably lead to an overestimate of that uncertainty.

5.5 Path Integral

In all preceding parts of this thesis, the plasma emitting the radiation to be analyzed was assumed to be homogeneous. In reality, the signal entering the optical system is the result of a path integral along the line of sight. For this discussion, it will be assumed that the emitting plasma volume is homogeneous with respect to temperature and magnetic field variations. Electron and neutral density are allowed to vary along the line of sight.

The light path will be parametrized with the length l, where l denotes the distance from the divertor plate onto which the view is directed. In addition, $l = d$ shall denote a point on the light path, such that all contributions to the signal come from points satisfying $l \leq d$. The intensity I of the radiation entering the optical system can then be calculated using

$$\frac{dI(\lambda)}{d\lambda} = \frac{A\,\Omega}{4\pi} \int_{l=0}^{d} \frac{d\epsilon(\lambda, l)}{d\lambda}\, dl\ . \tag{5.26}$$

Here, $A\,\Omega$ is the *étendue* of the instrument, and $\epsilon(\lambda, l)$ denotes the local emissivity of the plasma for the wavelength λ at the position l on the light path. I has units of [photons / s], and ϵ has units of [photons / s m^3]. The local emissivity can be calculated from

$$\epsilon(\lambda, l) = N_0(l)\, N_e(l)\, \langle \sigma v \rangle_{l, T(l), \lambda}\ . \tag{5.27}$$

The temperature is taken to be constant along the path integral. The cross section $\langle \sigma v \rangle_{l, T_0, \lambda}$ must be dependent on l since the spectral line shape is dependent on the electron density which can vary with l. With fixed temperature, the path integral reduces to

$$\frac{dI(\lambda)}{d\lambda} = \frac{A\,\Omega}{4\pi} \int_{l=0}^{d} N_0(l)\, N_e(l)\, \frac{d}{d\lambda} \langle \sigma v \rangle_{l, T_0, \lambda}\, dl\ . \tag{5.28}$$

As can be seen from this equation, the spectral profile from a deuterium transition is weighted by the product of the two densities. It is the aim of this section to model the signal entering the optical system, which is analyzed by the fitting routine (see chapter 4). For the numerical modeling which is performed for several functional dependences of $N_e(l)$ and $N_0(l)$ on l, the interval $[0, d]$ is divided into intervals

$$X_{path,i} = [(i-1)\,\Delta l,\ i\,\Delta l]\ ; i \in \left\{1, \ldots, \frac{d}{\Delta l}\right\} \qquad (5.29)$$
$$\text{with } \Delta l \longrightarrow 0\ .$$

The final signal entering the optical system is modeled to be emitted by $d/\Delta l$ separate volumes of length Δl along the path and of a cross section $A_\perp$ — which is taken to be equal for all the volumes — perpendicular to the path. Each separate volume V_i is located at the position l_i along the path and is indexed by $i \in \{1, \ldots, d/\Delta l\}$. It is assumed that the area $A_\perp$ covers the entire cross section of the light cone perpendicular to the path at all path positions l. Given the functional dependences of the electron and neutral density on the path parametrization l, one can calculate the spectral line profile of a particular deuterium transition emitted from the set of volumes $\{V_i | \, i \in \{1, \ldots, d/\Delta l\}\}$.

The magnetic field is assumed to be constant along the path, so the Zeeman splitting Δw_{Zeeman} is taken to be constant. The calculations presented are based on the 2–7-transition and on a magnetic field strength of $B = 5\,\mathrm{T}$. Using equation 3.24, the width $\Delta\lambda_{Stark,i}$ can be calculated from $N_e(l_i)$. The form parameter a_i of the Voigt profile describing the spectral line shape of the radiation emitted from the volume V_i is then derived from equation 4.14, thereby introducing instrumental and Doppler broadening artificially. The use of the $1800\,\mathrm{mm}^{-1}$ grating and a temperature of $T = 2\,\mathrm{eV}$ are assumed.

The spectral line shape of the deuterium 2–7-transition emitted from the volume V_i can then be described by the function

$$F_i^{path}(w) = N_e(l_i)\, N_0(l_i)\, F^{Zeeman}\left(\vec{V_i} = (a_i, 1, 0, 0), w, \Delta w_{Zeeman}\right)\ . \qquad (5.30)$$

The contributions from the different volumes are summed, leading to

$$F^{path}(w) = \sum_{i=1}^{d/\Delta l} F_i^{path}(w) \; . \tag{5.31}$$

This is the modeled input of the optical system, given the two density variations along the light path and the physical assumptions mentioned above.

In the following, four different configurations of density variations are used to calculate $F^{path}(w)$. These profiles are then analyzed using the standard routine for calculating the electron density; this routine is based on the spectral line shape of a single deuterium transition in the Balmer series.

Neutral and Electron Density Constant

If both neutral and electron density are kept constant along the path, the measured electron density will always be equal to the electron density on the divertor plate.

Neutral Density Exponentially Increasing and Electron Density Constant

$$\begin{aligned} N_e(l) &= N_{e,plate} \; , \\ N_0(l) &= N_{0,plate} \exp\left(p \frac{x}{d}\right) \; ; p > 0 \; . \end{aligned} \tag{5.32}$$

If the electron density is kept constant along the path, but the neutral density increases with the distance from the divertor plate, the measured electron density is still calculated to be equal to the density on the plate. This result is expected since the change in intensity cannot change the width of a line.

Neutral Density Constant and Electron Density Exponentially Decreasing

Assuming a flush mount probe measures the electron density on the divertor surface right at the location of the separatrix, the light path will lie within the private flux zone for all points with $l \geq 0$. The electron density will therefore decrease with increasing l. One can assume that this decrease is exponential and that the neutral

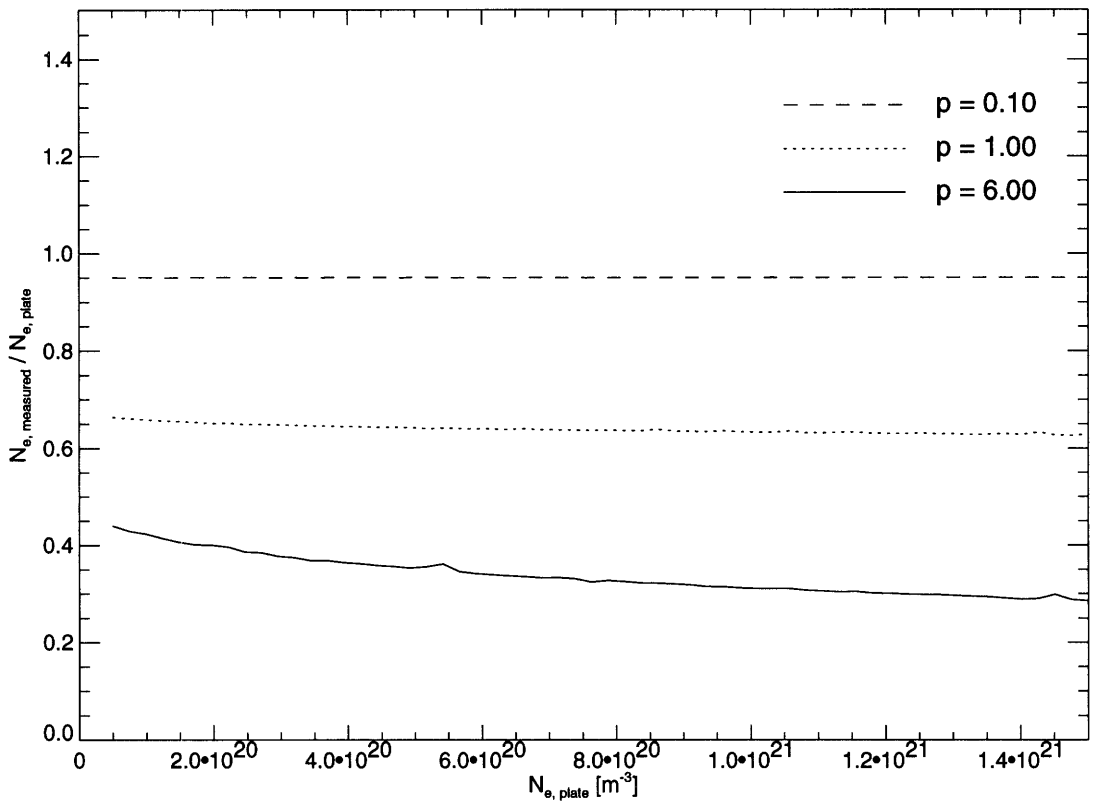

Figure 5-9: Case of a constant neutral density, with an electron density that is exponentially decreasing with the distance from the divertor plate (Equation 5.33). $N_{e,plate}$ denotes the electron density on the divertor plate. $N_{e,measured}$ refers to the electron density calculated from the path integral model.

density is constant:

$$\begin{aligned} N_e(l) &= N_{e,plate} \exp\left(-p\frac{x}{d}\right) \; ; p > 0 \; ; \\ N_0(l) &= N_{0,plate} \; . \end{aligned} \tag{5.33}$$

The modeled results are plotted in Fig. 5-9. The spectroscopically measured electron densities will always be lower than the electron density on the divertor surface, their ratio being almost constant as a function of the electron density on the plate.

Sharply Peaked Neutral and Electron Density Profiles

The case of electron and neutral density profiles which are sharply peaked at the same point along the path will be important for chapter 6 of this thesis since the MARFE phenomena discussed there lead to similar profiles. For the calculations, we

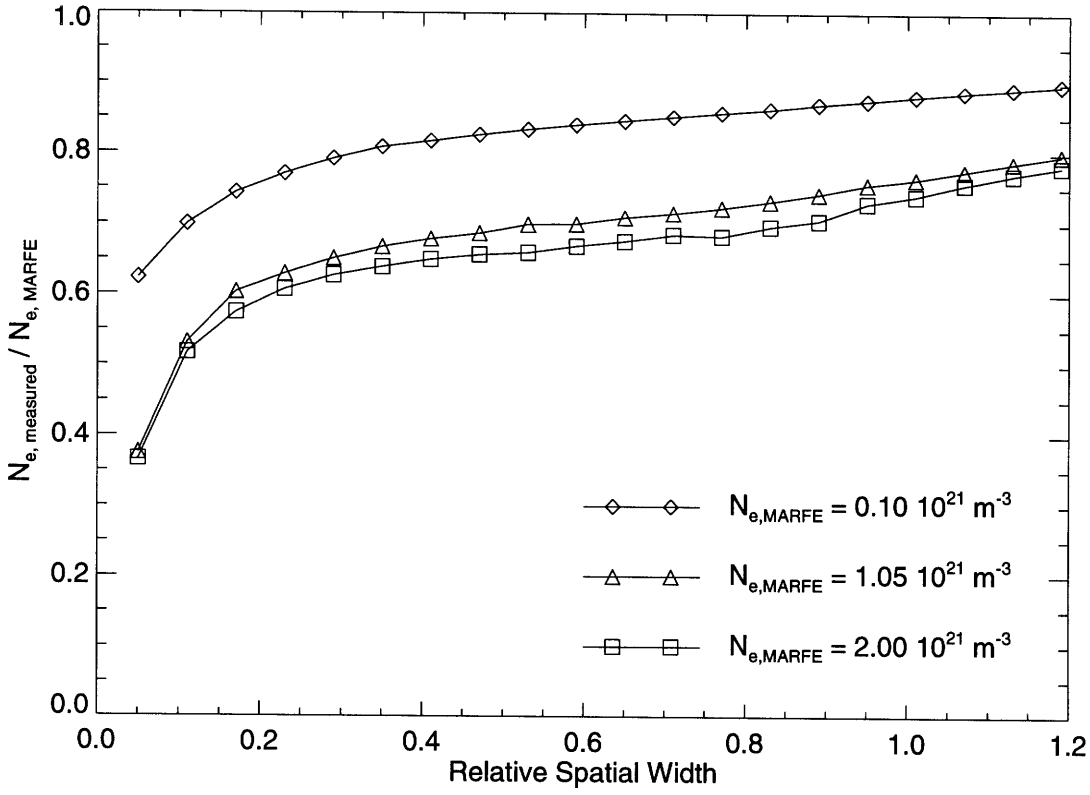

Figure 5-10: Case of neutral and electron density profiles which are sharply peaked at the same point along the path (equation 5.34). $N_{e,MARFE}$ denotes the peak electron density of the profile. $N_{e,measured}$ refers to the electron density calculated from the path integral model. The 'Relative Spatial Width' denotes the ratio $\Delta l/d$.

will assume the following spatial profiles:

$$N_e(l) = N_{e,background} + (N_{e,MARFE} - N_{e,background}) \exp\left(-\left[\frac{l-\frac{d}{2}}{\Delta l}\frac{2}{\sqrt{\ln 2}}\right]^2\right) \quad (5.34)$$

$$N_0(l) = N_{0,background} + (N_{0,MARFE} - N_{0,background}) \exp\left(-\left[\frac{l-\frac{d}{2}}{\Delta l}\frac{2}{\sqrt{\ln 2}}\right]^2\right) .$$

The two Gaussians describing the neutral and the electron density along the path have the same width Δl and are both peaked in the center of the path. The quantity $\Delta l/d$ will be referred to as the 'Relative Spatial Width' in Fig. 5-10 since it expresses the modeled spatial width of the MARFE as a fraction of the total effective path length. For the calculations, we choose

$$\frac{N_{0,MARFE}}{N_{0,background}} = 10 , \quad (5.35)$$

$$N_{e,background} = 5 \cdot 10^{19}\,\mathrm{m}^{-3} . \quad (5.36)$$

The calculations have been performed for three different peak electron densities $N_{e,MARFE}$ as a function of $\Delta l/d$.

The results are presented in Fig. 5-10. As expected, the electron density measured via Stark broadening is predicted to approach the peak electron density with increasing spatial width of the MARFE. Above relative spatial widths of ~ 0.3, the ratio between measured electron density and peak electron density increases roughly linearly with the spatial width.

Result of Error Analysis 5.5.1 (Path Integral) *If both electron and neutral density vary along the light path of the view, the spectroscopically measured electron density will lie between the minimal and the maximal electron density on the path. In addition, the measured value will lie close to* $N_e(l')$ *if* $N_e(l')\,N_0(l')$ *is the global maximum of the curve* $N_e(l)\,N_0(l)$.

5.6 Quantification of the Statistical Uncertainty in the Measurement

This section aims to quantify the uncertainty due to statistical fluctuations in the count rates and due to theoretical misrepresentations of the experimental spectral line shape. This section does not take into account the quantitative error in the theoretical Stark broadening parameters $\alpha_{1/2}$.

5.6.1 Electronic Noise

As described in chapter 2, the CCD detector exhibits the phenomenon of a thermally induced accumulation of dark charge. The error associated with this thermal effect can be quantified by analyzing the detector count rates measured without incoming signal.

Before each discharge, two frames of data are taken in order to subtract the background from the detected signal. These frames are used to calculate the statistical

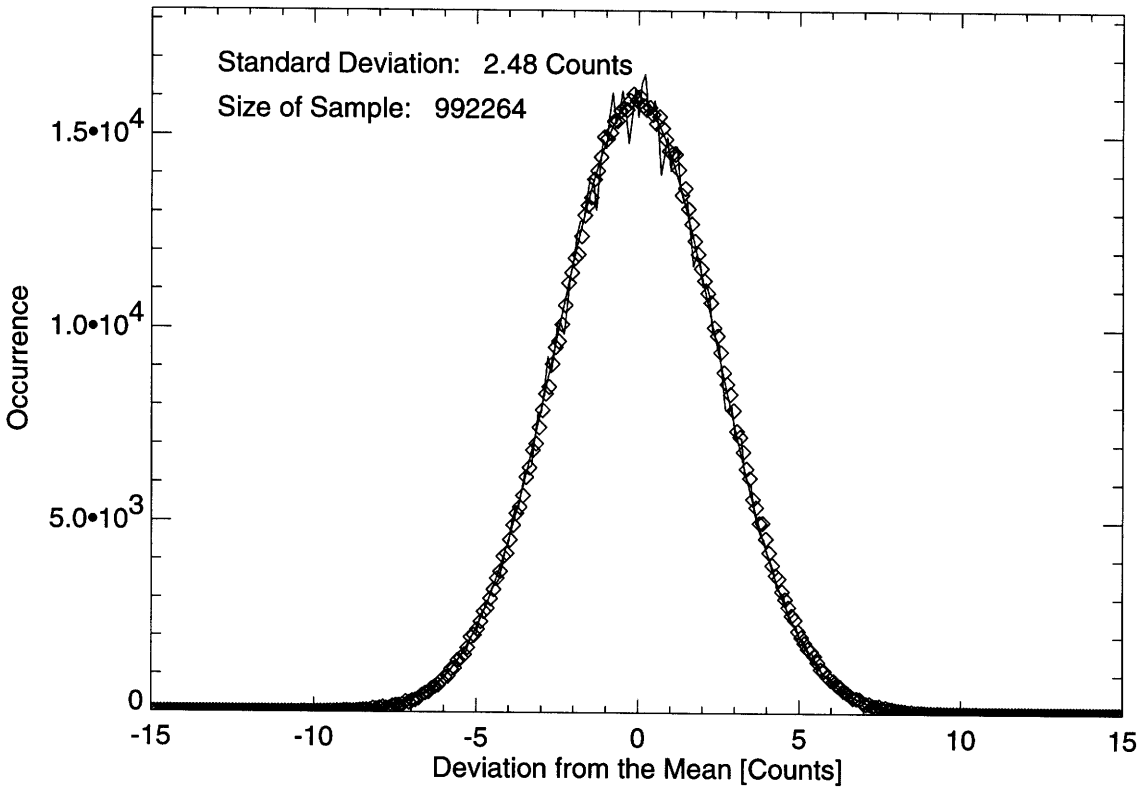

Figure 5-11: The discontinuous solid curve shows the distribution of the statistical count rate fluctuations due to electronic noise. The continuous solid curve is a Gaussian fit to this empirically determined distribution. Its standard deviation is calculated to be 2.48 counts. The sample has a size of 992264 data points. The diamonds show the distribution due to an artificially generated noise sample of the same size.

fluctuation due to electronic noise. A frame consists of 14 bin rows, each of them including 1242 bins for the spectral dimension. A least squares fit to the 14 background spectra of a frame is performed using a second order polynomial. The deviations Δc from this fit are stored in a database. A histogram is generated which shows the distribution of these deviations. The distribution is plotted in Fig. 5-11. Its functional dependence is given by

$$P(\Delta c) = \frac{1}{\sqrt{2\pi}\,\sigma} \exp\left(-\frac{\Delta c^2}{2\,\sigma^2}\right) . \tag{5.37}$$

The function $P(\Delta c)$ is normalized to unity and the standard deviation σ satisfies $\langle x^2 \rangle = \sigma^2$. The calculation leads to $\sigma_{noise} = 2.48$ counts.

In order to estimate the error of the measurements, it will be necessary to generate artifical noise with the same statistical characteristics as the measured noise. This

will allow to quantify the numerical response of the analysis routine to noise. As an example, artificial noise has been generated with a standard deviation of 2.48 counts and an average of zero counts. Using the same sample size as for the experimental data, the two distribution functions coincide, as can be seen in Fig. 5-11.

5.6.2 Characterization of the Error in the Spectral Line Fits

It is assumed that the vectors containing the *abscissa* and *ordinate* values of the raw data used for the fit in w-space,

$$\vec{i}_{fit} = \left(i_{\lambda_1}, ..., i_{\lambda_k}, ..., i_{\lambda_p}\right) \text{ and} \tag{5.38}$$

$$\vec{w}_{fit} = (w_1, ..., w_k, ..., w_p), \tag{5.39}$$

are given, together with the corresponding *ordinate* values of the fitted theoretical profile:

$$\vec{F} = (F_1, \ldots, F_k, \ldots, F_p) . \tag{5.40}$$

These vectors are available after each separate fit to a single line. The error in the spectral line fits can be analyzed statistically by exploiting these vectors.

Knowing the fit parameters, one can subtract the linear correction and the constant background and obtain the vector

$$\vec{c} = (c_1, ..., c_k, ..., c_p) , \tag{5.41}$$

$$c_k = F_k - V_{2,2-n} - V_{3,2-n}\, w_k .$$

The vector $\vec{c}$ denotes the count rate solely due to incoming photon flux, based on the theoretical fit. The constants $V_{2,2-n}$ and $V_{2,2-n}$ for the deuterium transition 2–n are returned by the analysis routine as results of the fit. In addition, the deviation of the data from the fit can be calculated and stored in the vector

$$\Delta\vec{c} = (\Delta c_1, ..., \Delta c_k, ..., \Delta c_p) , \tag{5.42}$$

$$\Delta c_k = i_{\lambda_k} - F_k .$$

The paired data points $\{[c_1, \Delta c_1], \ldots, [c_p, \Delta c_p]\}$ will be used for the statistical characterization of the numerical fits.

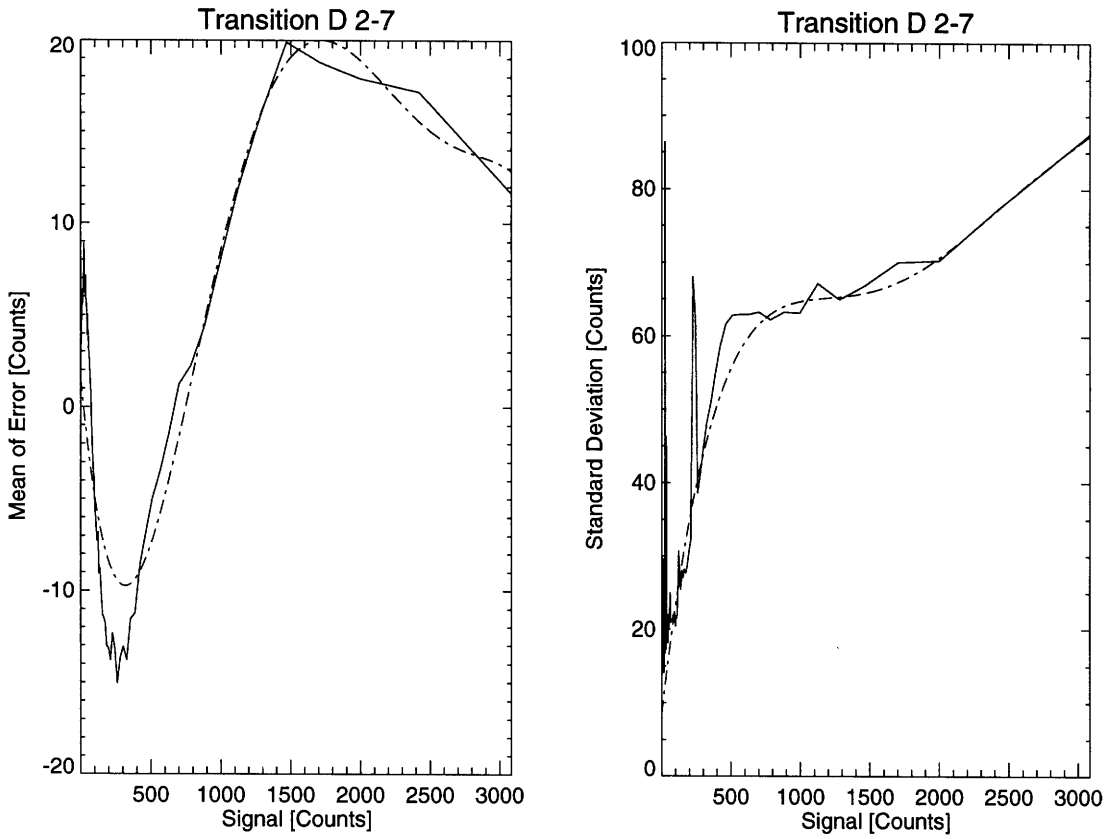

Figure 5-12: The statistical deviation of the measured spectra from the numerically fitted theoretical line shapes. Left: The solid curve shows the average of the deviation as a function of the signal c due to photon influx. The dashed curve provides a smooth polynomial approximation $\overline{\Delta i}(c)$ used for further analysis. Right: The solid curve shows the standard deviation as a function of the signal c due to photon influx. The dashed curve provides a smooth polynomial approximation $\sigma_i(c)$ used for further analysis.

Data points were accumulated over several discharges, leading to a size sample of 483534 points. For this sample, only numerical fits to the deuterium 2–7-transition were collected. From these data points, the average deviation of the numerical fits from the measured spectra is calculated as a function of the signal due to the incoming photon flux. Similarly, the standard deviation is calculated as a function of the same parameter. For both curves, each data point is calculated from a subset of 2000 points. The two curves are presented in Fig. 5-12.

As to be expected, the absolute standard deviation increases with the signal. The discontinuous peaks in the curve are due to impurity effects which always occur at typical locations within the fit. For further error analysis, the average deviation and

the standard deviation will be approximated by the smooth polynomial functions $\overline{\Delta i}(c)$ and $\sigma_i(c)$, which are also shown in Fig. 5-12. These two functions completely characterize the statistical error of the theoretical fits to transition 2–7.

5.6.3 Statistical Uncertainty in Electron Density Measurements

The method used to estimate the statistical uncertainty of the electron density calculation will be presented here. To find the error at a given density $N_{e,gen}$, the theoretically predicted profile $F^{Zeeman}(\vec{V}, w, \Delta w)$ is used to generate the vector

$$\vec{F}_{theory} = (F_{theory,1}, \ldots, F_{theory,k}, \ldots, F_{theory,p}) , \tag{5.43}$$

$$F_{theory,k} = F^{Zeeman}(\vec{V}_{theory}, w_k, \Delta w_{Zeeman}) , \tag{5.44}$$

$$\vec{V}_{theory} = (a(N_{e,gen}), V_{theory,1}, 120, 0) . \tag{5.45}$$

All parameters are defined in chapter 3 and are chosen according to the transition 2–7 for an electron density $N_{e,gen}$, no linear correction, and a background of 120 counts per 45 ms. In addition, a magnetic field strength of $B = 6\,\mathrm{T}$ and a neutral temperature of $T = 2\,\mathrm{eV}$ are assumed. The multiplicative scale $V_{theory,1}$ is chosen such that the peak height is 1000 counts.

Let $\mathrm{Rnd}(\sigma, k)$ be a function that returns a random value for any value of k, based on a Gaussian distribution with a standard deviation of σ and an average value of zero. One can then generate the vector

$$\vec{F}_{error} = (F_{error,1}, \ldots, F_{error,k}, \ldots, F_{error,p}) , \tag{5.46}$$

$$F_{error,k} = \overline{\Delta i}\,(F_{theory,k} - 120) + \mathrm{Rnd}\,(\sigma_i\,(F_{theory,k} - 120), k) . \tag{5.47}$$

This vector contains the artificially generated fluctuations, adjusted to the form of the fit.

Adding the theoretical profile due to the incoming photon flux to the artificially generated fluctuations, we obtain

$$\vec{F}_{gen} = \vec{F}_{theory} + \vec{F}_{error} . \tag{5.48}$$

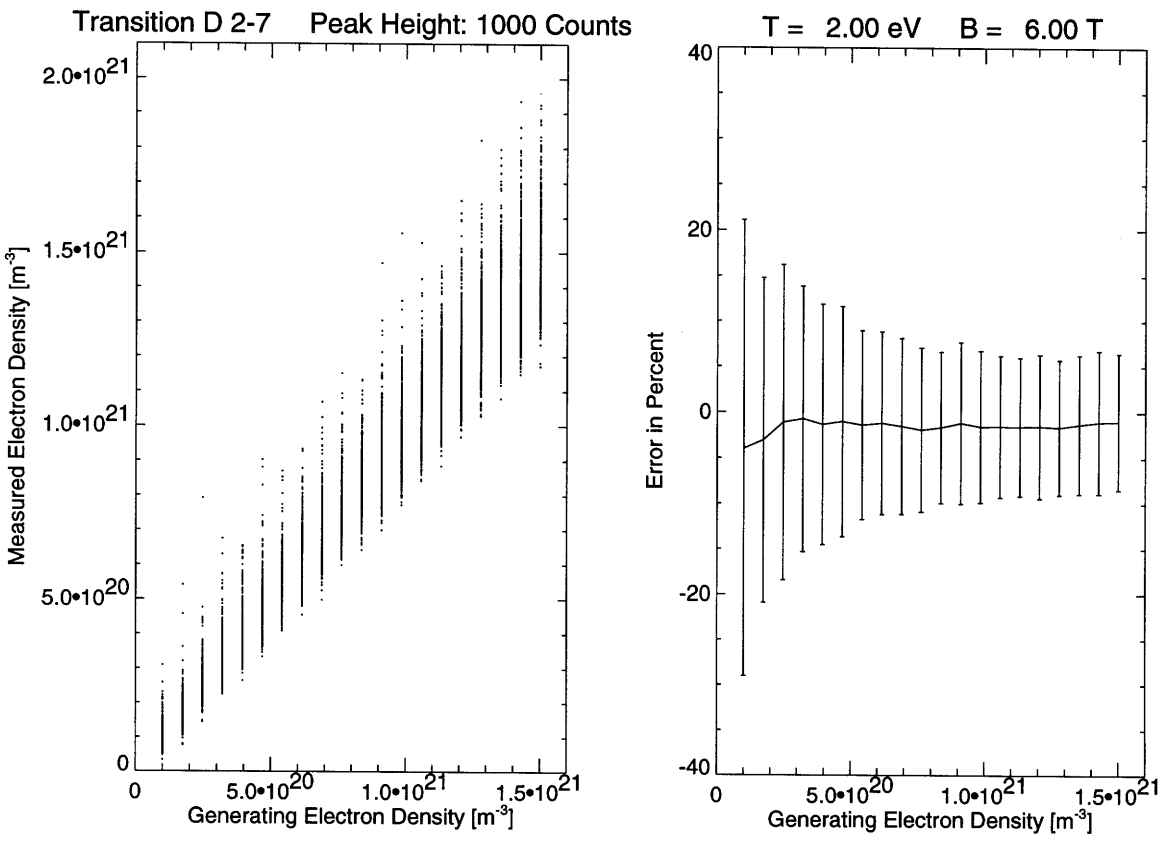

Figure 5-13: The effective error of the calculated electron density. Left: Scatterplot of the calculated electron density for theoretical profiles with artificially induced data scattering, as a function of the electron density that generates the theoretical profile. Right: The average error and the statistical error bars of the electron density calculation, derived from the scatterplot on the left.

This vector is *constructed* to statistically resemble the data one is expected to measure over a large sample. For a given generating density $N_{e,gen}$, a sample of 1000 vectors $\vec{F}_{gen}$ is generated. The analysis routine is applied to all these 'virtual spectra', calculating an electron density for each one of them. For the resulting set of electron densities, the average and the standard deviation are calculated. These results are presented in Fig. 5-13, both in form of a scatterplot and expressed relative to $N_{e,gen}$.

These results are rigorously correct only for the 2–7 transition, but they can be used as an upper limit for the transitions 2–8 and 2–9 as well since those generally have a broader profile whose width is less sensitive to fluctuations. These results do not apply to the 2–10-transition which, as shown earlier in this chapter, is not a

reliable source for the electron density calculation.

Result of Error Analysis 5.6.1 (Statistical Uncertainty) *The maximal statistical uncertainty of the presented procedure for the measurement of electron densities, using the transitions 2–7, 2–8, 2–9 of deuterium, is presented in* Fig. 5-13. *For electron densities larger than* $N_e = 3 \cdot 10^{20}\, m^{-3}$, *the maximal statistical uncertainty is smaller than* $\pm 15\%$. *This excludes the error in the theoretical Stark broadening parameters denoted by* $\alpha_{1/2}$.

5.7 Summary of Measurement Uncertainties

An attempt will be made to provide an estimate of the overall uncertainty in the electron density for the method discussed above. We will assume that the measurement is performed using the deuterium 2–7-transition observed with the $1800\,\mathrm{mm}^{-1}$ grating. We will also restrict the estimate to electron densities higher than $N_e = 3 \cdot 10^{20}\,\mathrm{m}^{-3}$.

For those densities, the statistical uncertainty is smaller than $\pm 15\%$, as has been shown in the previous section. The inaccuracy of the electron density due to the uncertainty of the instrumental profile measurements is smaller than $\pm 10\%$, as has been argued in 3.2.2.

All the measurements of spectral widths are dependent on the dispersion measurements whose uncertainties are discussed in section B.1.3 of the appendix. For the $1800\,\mathrm{mm}^{-1}$ grating, the uncertainty in the dispersion is estimated to be $\pm 3.2\%$, leading to an uncertainty of $\pm 4.6\%$ in electron density.

Under the condition of *exactly* known theoretical Stark widths $\alpha_{1/2}$ and assuming a homogeneously emitting volume, the method described in this thesis could therefore perform electron density measurements with an uncertainty of less than $\pm 19\%$ for the 2–7-transition with electron densities higher than $3 \cdot 10^{20}\,\mathrm{m}^{-3}$.

However, it has been argued in section 3.4.2 that the theoretical Stark widths used in this thesis are generally too small for our application. The theoretical $\alpha_{1/2}$ parameter for the transition 2–6 of deuterium is 15% too small, resulting in calculated electron densities that are 19% too high. In addition, the radiation observed is not

emitted by a homogeneous volume. On the contrary, neutral and electron density profiles will vary strongly along the path of the spectrometer chords, thereby effecting the measured electron densities significantly. The effects of these variations were discussed in section 5.5.

Chapter 6

Electron Density Measurements

This chapter presents the results of the electron density measurements performed with the method defined in the previous parts of this thesis. An emphasis is put on the correlation with measurements from other diagnostics such as H_α tomography and interferometry. The results from the outer divertor views A_{bottom} and the inner divertor views K_{bottom} are discussed separately.

The brightnesses of the Balmer transitions observed on the inner divertor fibers exhibit a strong spatial correlation with the tomography of the H_α emissivity. In the case of strongly peaked emissivities, this correlation allows us to use H_α tomography as a tool for determining the poloidal region where the dominant contribution to the signal on the *Chromex* fibers originates. Based on this reasoning, this chapter will present the spatial electron density profile of a MARFE at the inner divertor, as well as show the consistency of the electron density calculated from Stark broadening with the interferometer measurements for a MARFE at the outer divertor.

The same reasoning which proves the usefulness of the Stark broadening method for measuring the inner divertor electron densities also explains why there is no correlation between the outer divertor probe electron densities and the results obtained from the Stark broadening observed on the outer divertor fibers. A quantitative analysis of reflection measurements will show that the radiation entering the outer divertor fibers is largely dominated by contributions from the inner divertor. This explains why one cannot expect a correlation between the outer divertor probe results

and the electron densities resulting from the Stark broadening analysis of the outer divertor views.

6.1 Correlations with the Outer Divertor Langmuir Probes

The *intended* design for the mapping between the Langmuir probe positions and the outer divertor chords of the *Chromex* system is presented in Fig. 2-5. Using this correspondence, the correlation between the results from the Stark broadening method and the Langmuir probes can be analyzed statistically.

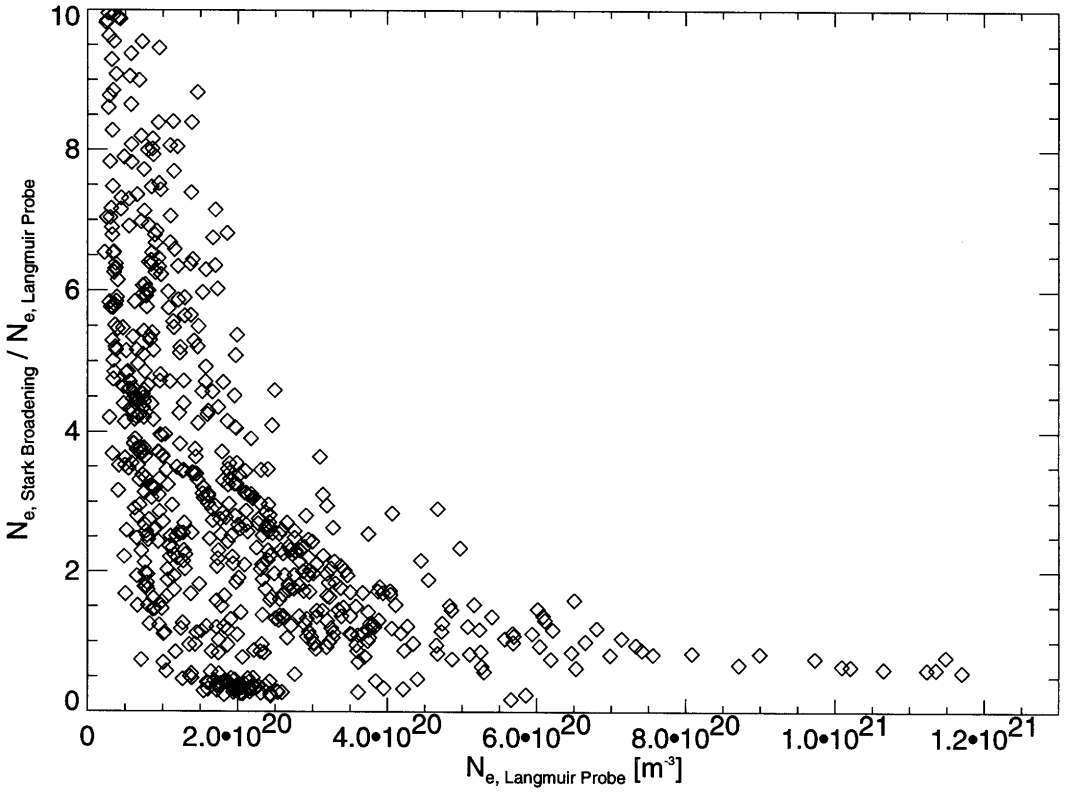

Figure 6-1: Statistical correlation between the Langmuir probe measurements and Stark broadening: a scatterplot of the ratio between the two measurements versus the electron density obtained from the Langmuir probes. The correlation shown refers to the Langmuir probe FMP 5 in Fig. 2-5 and the signal from the view $A_{bottom}\,12$ of the *Chromex* system. For the Stark broadening analysis, the Balmer transition 2–7 is used. The data are taken from discharges between April and June 1995 without any preselection.

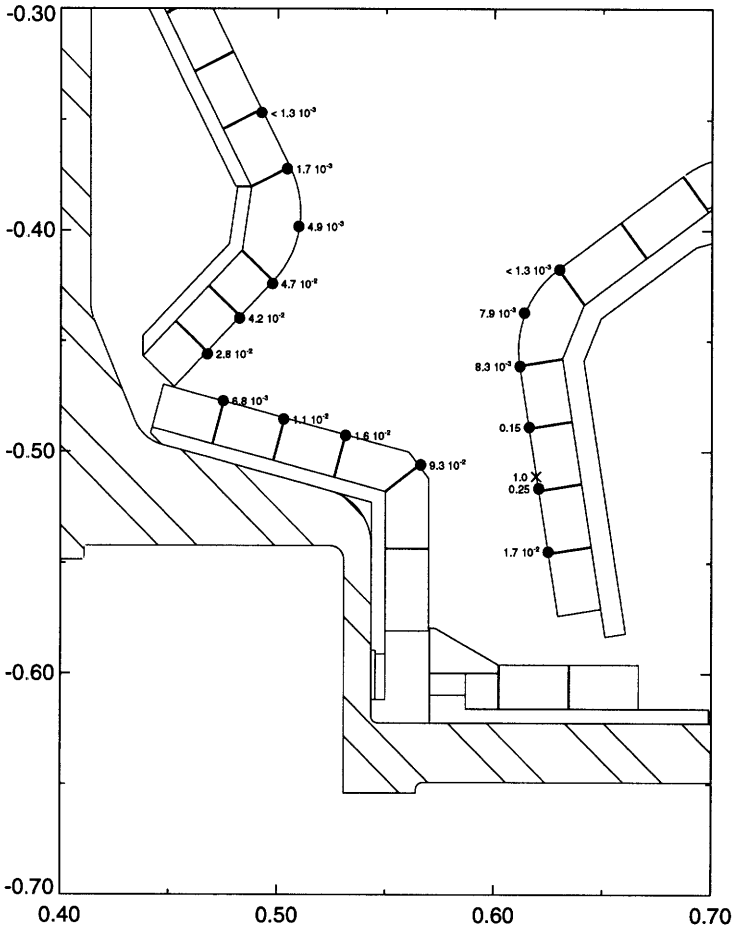

Figure 6-2: Reflective properties of the divertor surface for a white visible light source, using the fiber A_{bottom} 12 as a reference. The power of the photon influx is maximal if the source is moved to the point marked with a *cross*. The relative power for other source positions is given at the *dots*.

It is evident from Fig. 6-1 that there is no statistical correlation between the two measurements for electron densities at the Langmuir probes which are lower than $7 \cdot 10^{20}\,\mathrm{m}^{-3}$. Above that value, the ratio of the two measurements seems to approach a constant.

It has to be mentioned that the data used for the generation of Fig. 6-1 are not pre-selected, implying that both detached and undetached discharges (see Refs. [13, 16]) contribute to the total set of presented data. The effect of detachment could in principle explain why the Langmuir probe results can be much lower than the Stark broadening results: when the plasma is detached, the electron density on the divertor surface — which is measured by the probes — will essentially vanish. Nonetheless, a light path ending at the probe position could still intersect spatial regions with

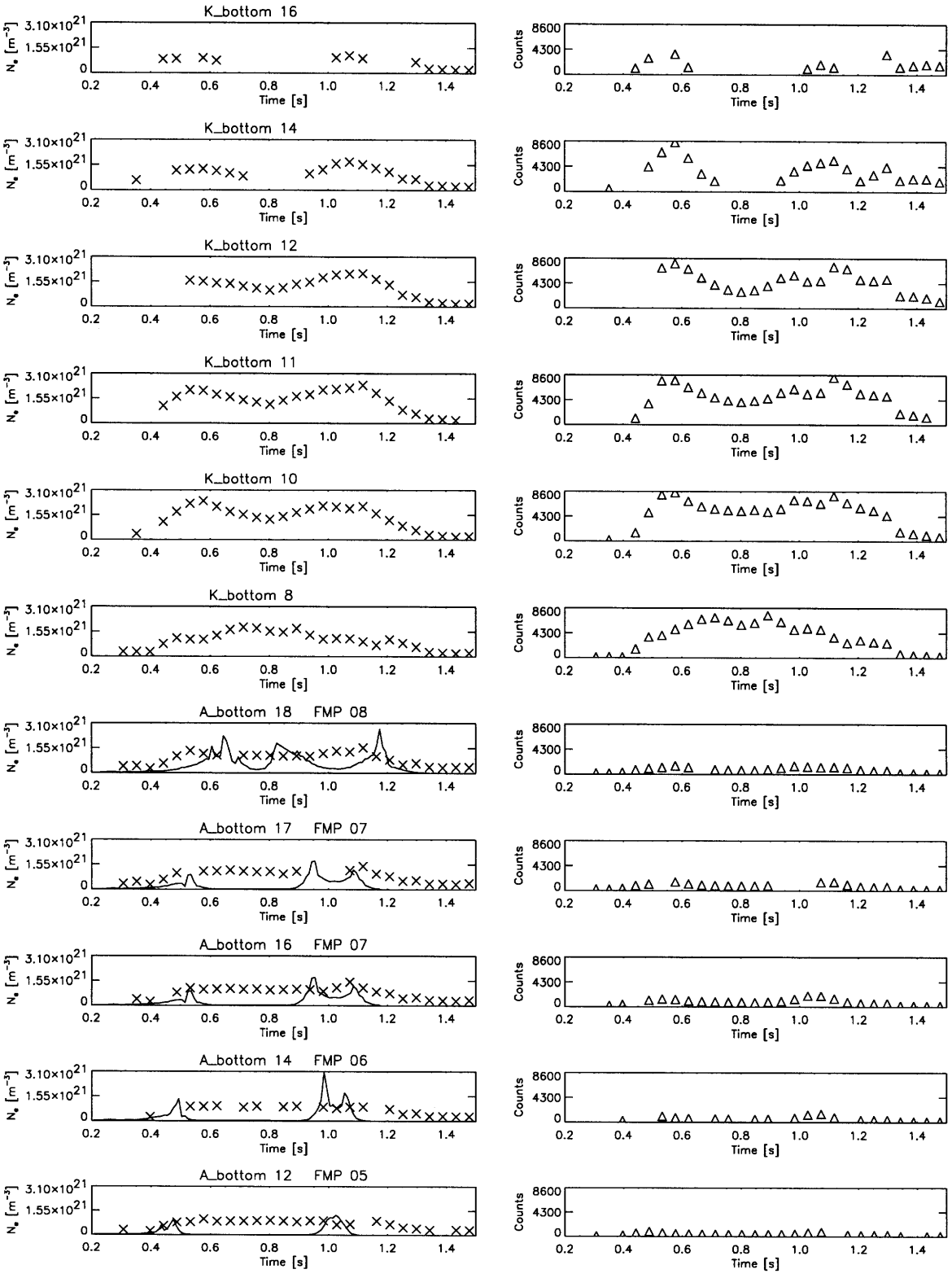

Figure 6-3: Stark Broadening analysis for chords viewing the outer divertor, using the Balmer transition 2–7 in discharge 950601012. The left column shows the Stark broadening results (crosses) and the Langmuir probe results (solid line) for the electron density as a function of time for the different views of the inner and outer divertor. The right column shows the intensity of the incoming photon flux for the 2–7 transition.

finite plasma density pulled back from the surface. The ratio between the two results would then not be an appropriate measure of the correlation between them. A closer examination on the basis of single detached discharges did not confirm this hypothesis, though. The lack of correlation, for low probe densities, between these two measurements is a phenomenon independent of detachment.

It will be argued that the reason for the lack of correlation in the case of low electron densities measured by the Langmuir probes is due to a principal difference between the two measurements: the Langmuir probes measure a density at a *single point* in space, whereas the spectrum observed by the spectrometer system is emitted by a *volume*. The sufficient and necessary condition for both measurements to lead to the same result requires that the light analyzed with the Stark broadening method is emitted solely in the vicinity of the point where the Langmuir probe measurement is performed.

This condition is not necessarily met, as can be seen from Fig. 6-2, which characterizes the reflective properties of the divertor surface for a white visible light source. This figure uses the same reference fiber as Fig. 6-1. The radiative power entering the fiber A_{bottom} 12 is maximal if the source is placed within the divertor slot, but up to 4.7% of that maximal input power is detected if the same source is placed at the inner divertor slightly below the nose. These reflective contributions to the signal on fiber A_{bottom} 12 have to be integrated over the whole divertor area in order to obtain the total reflective contribution to the A_{bottom} 12 input.

This integration has been carried out as described in Appendix C. As shown there, the inner divertor regions contribute about an order of magnitude more radiative power to the outer divertor fiber A_{bottom} 12 than the regions in the divertor slot. This calculation is based on the assumption that the plasma emissivity is homogeneous throughout the poloidal region where more than 90% of the total H_α emission in the divertor originates. In reality, the emissivity in the divertor slot is lower than the emissivity near the inner divertor, thereby increasing the relative contribution of the inner divertor region to the power input on fiber A_{bottom} 12. This implies that in almost all cases the signal observable through the outer divertor fibers will be entirely

dominated by light originating far from the outer divertor surface where the probes are situated.

Such a situation is shown in Fig. 6-3, presenting the Stark broadening analysis of an attached discharge. The intensity of the lines used for the Stark broadening analysis is very low for the A_{bottom} fibers viewing the outer divertor, compared to the intensity for the inner divertor views: the intensity on the A_{bottom} 12 fiber is about 8% of the intensity on the inner divertor view K_{bottom} 10 for the 2–7 transition at 0.8 s. It is then consistent with the reflection measurements presented in Fig. 6-2 and with their analysis in Appendix C to argue that a dominant contribution to the signal at A_{bottom} 12 originates above the divertor slot and reaches the outer divertor chords via reflection on the divertor surface.

This argument is also supported by the time dependence of the measured electron density which allows us to infer roughly where the analyzed radiation originates. Fig. 6-3 shows that the time dependence of the electron density measured on the chord A_{bottom} 18 resembles the one on the chords K_{bottom} 10-11-12. This can be explained by the fact that the upper A_{bottom} chords view regions of the plasma which are intersected by those K_{bottom} chords as well. The region covered by the lower A_{bottom} chords, on the contrary, should — in the absence of reflection — not have any overlap with the region viewed by the K_{bottom} array. Between 0.6 s and 1.0 s, the lower A_{bottom} chords observe a constant electron density which could result from a combination of radiation emitted in spatial regions covered by the fibers K_{bottom} 8-10, that is, spatial regions located close to the inner and outer noses.

In addition, the time dependence of the electron density on the A_{bottom} chords shows no correlation at all with the probe measurements. The probes show peaks whenever the separatrix strike point coincides with the probe position, as can be shown from other standard measurements not presented here. Once the strike point lies above a probe, the electron density measured by that specific probe drops essentially to zero, whereas the result obtained by the Stark broadening method remains at its constant value. The fact that the Stark broadening result for the electron density in this attached discharge is not affected by the separatrix sweeping through the

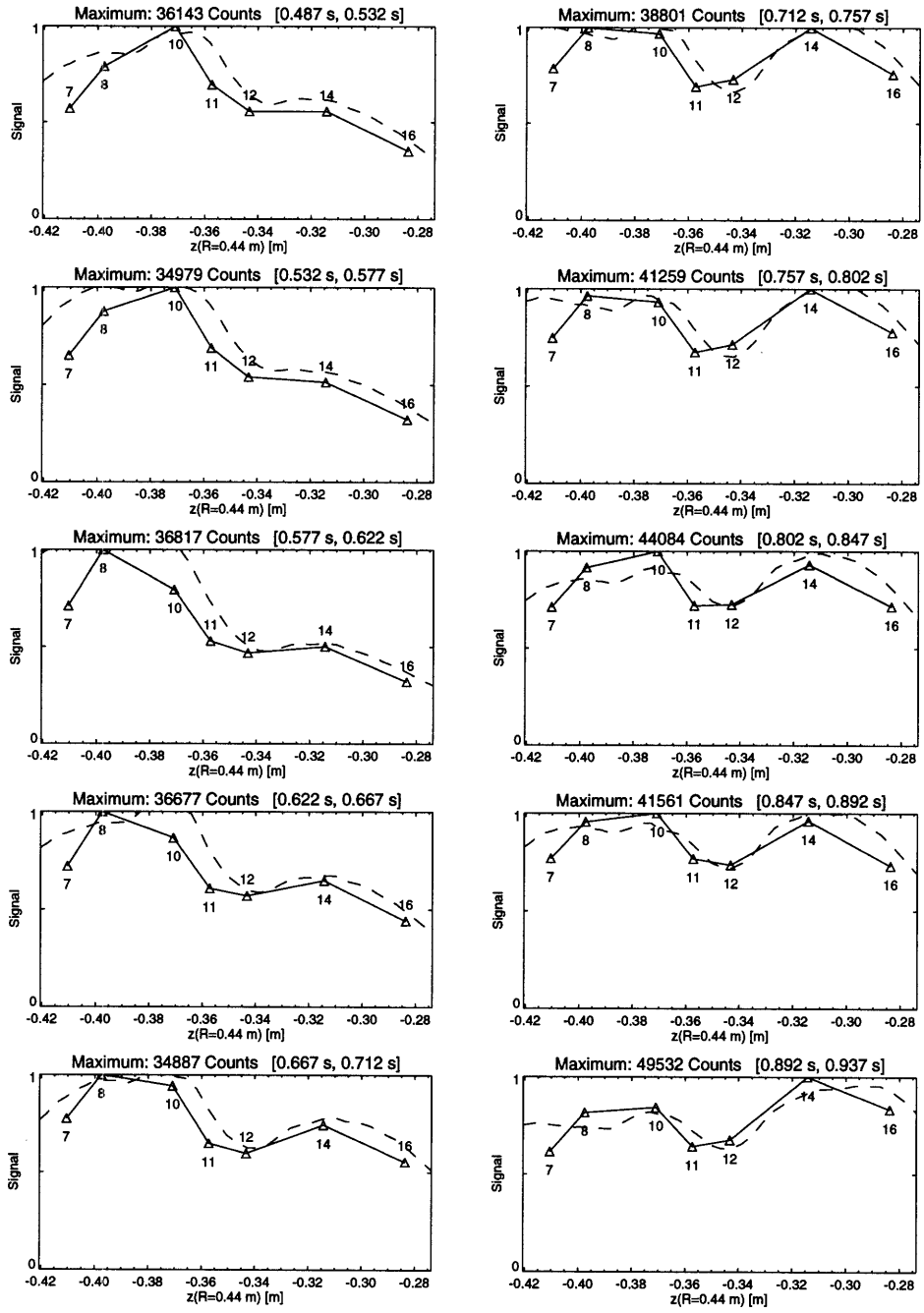

Figure 6-4: Correlation with the diode detector arrays used for the H_α tomography in discharge 950519007. The solid lines show the relative brightnesses of the 2–7-transition observed on the K_{bottom} fibers. These relative brightnesses were obtained by integrating over the spectral interval [396.5 nm, 397.7 nm] and by subtracting the background; they are presented relative to their maximum value in a specific time frame. The dashed lines show the brightness of the $K_{bottom,RA}$ diode detector array, which is rescaled separately in each time frame. Both brightnesses are plotted versus the z-coordinate at which the corresponding chord crosses the radial position $R = 0.44\,\mathrm{m}$. The numbers indicate the positions of the K_{bottom} fibers.

divertor slot indicates that the signal analyzed is dominated by contributions from above the slot.

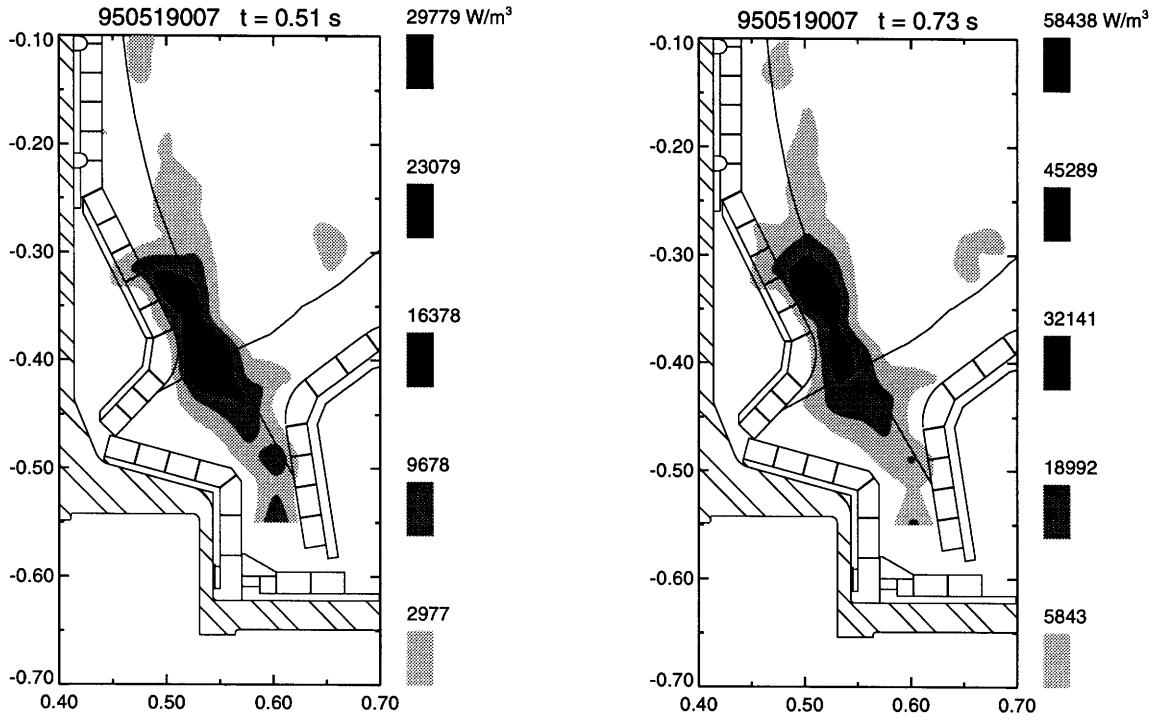

Figure 6-5: H_α tomography for the discharge 950519007 at two different times.

The reasoning presented here can provide a possible explanation for Fig. 6-1: the intensity of the emitted radiation is proportional to the product of neutral and electron density. So lower electron densities measured by the probes tend to correspond to cases of lower emissivities in the divertor slot. In those cases, the signal observed by the *Chromex* system would be more likely to be dominated by contributions from above the slot. From the error analysis performed in chapter 5, it is apparent that the Stark broadening analysis cannot lead to errors of more then 30%, even for very low electron densities. The statistical behavior of the ratio plotted in Fig. 6-1 is thus due to the fact that the radiation used for the electron density calculation via Stark broadening does simply not originate in the divertor slot. The data on the lower A_{bottom} fibers shown in Fig. 6-3 illustrate how vanishing probe results can combine with finite Stark broadening results for the electron density.

6.2 Correlation between *Chromex* Chord Brightnesses and H_α Tomography

This section aims to demonstrate that there is a strong correlation between the H_α tomography and the brightness profiles observed with the K_{bottom} array of the *Chromex* system.

The plasma is viewed by several diode detector arrays filtered with an optical bandpass which is centered at the H_α-transition, each of the arrays consisting of 64 separate chords. One of these diode detector arrays — to be referred to as $K_{bottom,RA}$ — observes the plasma from the same direction as the K_{bottom} array of the *Chromex* system. A routine presented in Ref. [12] is used to invert the absolute brightnesses measured on the diode detector chords into a tomography of the H_α emissivity in the poloidal plane.

It is important to note that the H_α emissivity is *generally not* proportional to the emissivity of the high-n Balmer transitions used for the Stark broadening analysis. According to the calculations presented in Ref. [7], the line intensity ratio H_ϵ/H_α varies between $6.5 \cdot 10^{-4}$ and 10^{-3} within a parameter range given by

$$10^{20}\,\mathrm{m}^{-3} \leq N_e \leq 4 \cdot 10^{21}\,\mathrm{m}^{-3}\,,\;\; 10\,\mathrm{eV} \leq T_e \leq 100\,\mathrm{eV}\,.$$

Even though the line intensity ratios do depend on electron density and electron temperature, the poloidal regions of peaked H_α emission will still be regions of peaked 2–n emission as well. It will still be possible to determine localized high emissivity regions for a high-n Balmer transition by analyzing the H_α emissivity, although a *quantitative* evaluation of the 2–n emissivity from the H_α tomography would require a detailed *a priori* knowledge of electron density and temperature. For our purposes, only a qualitative knowledge about localized high emissivity regions of the high-n Balmer transitions is needed. This information can be extracted from the H_α tomography.

Fig. 6-4 shows the correlation between the brightnesses of the K_{bottom} and the $K_{bottom,RA}$ arrays in a typical discharge. It is apparent that both curves correlate strongly, except for a shift along the z-axis with respect to each other. This effect is

best seen in the time frames [0.532 s, 0.577 s] and [0.757 s, 0.802 s]. The tomography for this discharge is presented in Fig. 6-5, exhibiting a single emissivity peak at 0.51 s and two spatially separated emissivity peaks at 0.73 s, thereby demonstrating that the tomography plots can be used to determine the spatial origin of the brightness observed by the K_{bottom} chords of the *Chromex* system.

The relative vertical shift between the two arrays amounts to about 1.5 cm, corresponding to approximately 1 fiber in the K_{bottom} array. The graphs in the subsequent sections of this thesis will be corrected for this shift. It is important to note that the poloidal pixels underlying the tomographic inversion are squares with a side length of 2.5 cm. The emissivities are calculated for these pixels, which are assumed to cover areas of uniform emissivity and which are distributed uniformly across the poloidal plane. The calculated emissivities are then smoothed on a much finer grid leading to a least curvature contour that appears to be continuously varying on the poloidal plane. Since the smoothing does not eliminate the underlying spatial resolution given by the pixel size, the correspondence between the tomography and the K_{bottom} brightnesses cannot be expected to have an accuracy of better than ± 1 fiber.

Since the line intensity ratios between Balmer series members depend — as discussed above — on electron density and electron temperature, the chord brightnesses of each time frame presented in Fig. 6-4 are scaled separately, in case the plasma parameters are changing over time. The spatial variation of the plasma parameters could still affect the correlation within a given time frame of that figure.

6.3 Electron Density Measurement of a MARFE

The expression 'MARFE' is an acronym for 'Multifaceted Asymmetric Radiation From the Edge'. The physical phenomenon referred to by this expression is discussed in Refs. [14] and [15].

A MARFE is characterized by an increase in the local electron density N_e, the rms fluctuation amplitude $\tilde{N}^2$, the scale length λ_n of the plasma edge density in the scrape-off-layer, and — most important for the analysis here — low-Z, low-ionization-

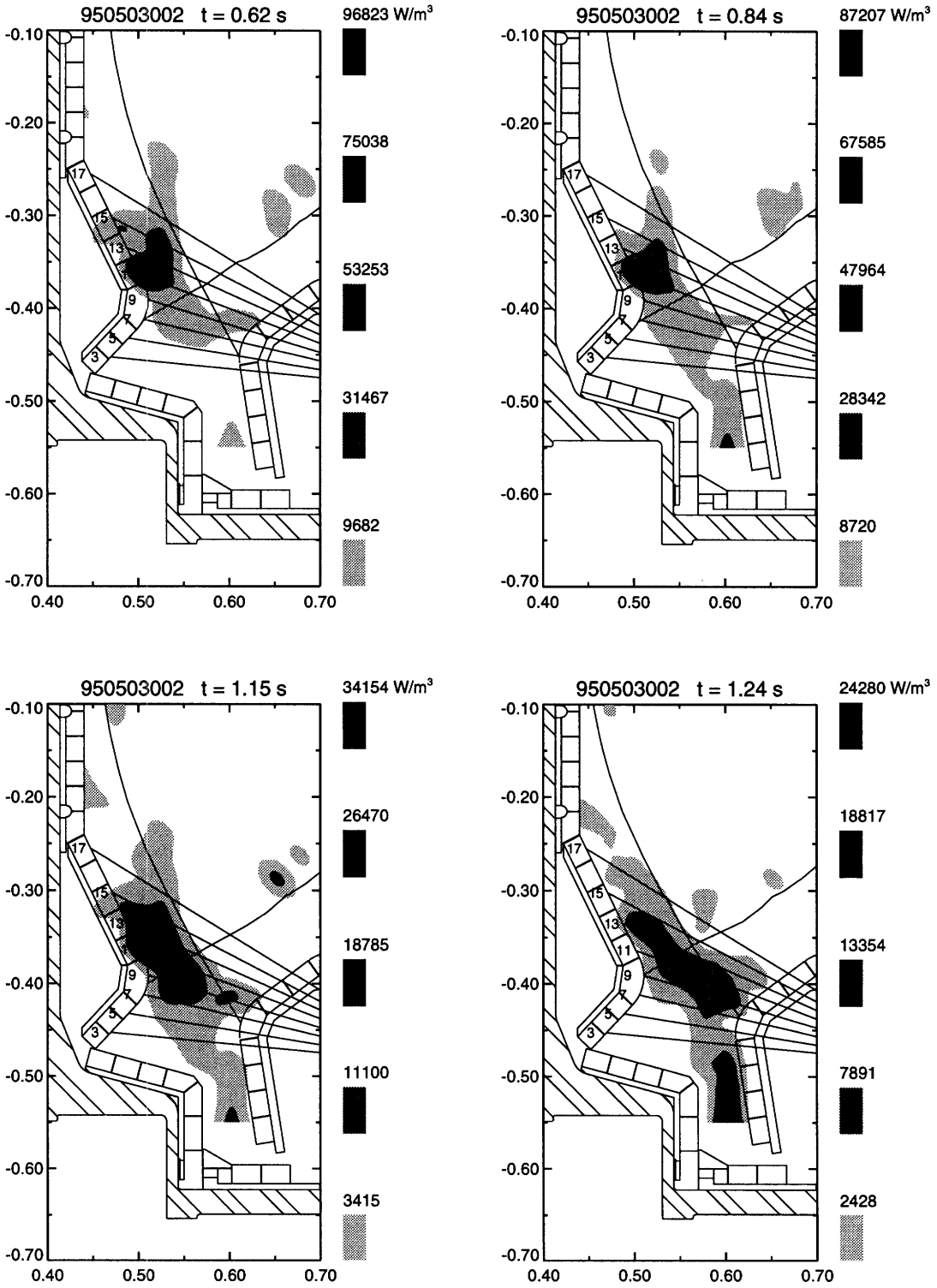

Figure 6-6: H_α tomography of a MARFE at the inner divertor at different times in the same discharge. The approximate chords of the K_{bottom} fibers are drawn into the divertor geometry.

state radiation. The MARFE phenomenon is local, with no measurable effects noted at farther poloidal distances (i.e. larger than $\sim 10\,\mathrm{cm}$). MARFEs exhibit toroidal symmetry and are most commonly confined to the high-field edge of the plasma, with a poloidal extent of typically 30° if viewed from the magnetic axis.

The study of MARFEs is most suited to the Stark broadening method presented in this thesis since a MARFE is a poloidally *localized* phenomenon which can be identified on an H_α tomography as an emissivity peak. Radiation observed by a chord which intersects a MARFE will in many cases be dominated by the MARFE emission. The electron density obtained from the Stark broadening of this radiation will then describe the electron density of the MARFE. So tomography allows us to determine the poloidal region where the main contribution of the analyzed radiation originates, thereby making it possible to assign the Stark broadening electron density to that poloidal region.

6.3.1 MARFE at the Inner Divertor

The tomography of a MARFE at the inner divertor is shown in Fig. 6-6, together with the K_{bottom} chords viewing the inner divertor. Especially the first three tomography frames presented {0.62 s, 0.84 s, 1.15 s} exhibit clearly peaked emissivities. It is essential to note the fact that the tomography graphs are scaled individually.

These peaks can be found in the spatial electron density profiles in Fig. 6-7, which were calculated using the 2–7-transition. The first three frames exhibit an electron density peak near the fibers 10-11 of the K_{bottom} array. The central electron density of the MARFE observed is $N_{e,MARFE} \approx 1.7 \cdot 10^{21}\,\mathrm{m}^{-3}$ for the first three frames.

The half width of the electron density peaks corresponds to about 5.6 fibers or 8 cm of vertical poloidal extent for the first three time frames presented. As can be seen in the tomography, the effect of the MARFE should be restricted to the fibers K_{bottom} 9–16. In the third frame shown, the radial width of the MARFE has increased significantly, an effect which cannot be observable in the Stark broadening data since the relevant K_{bottom} fibers have only a small angle with the horizontal axis.

Between 1.15 s and 1.24 s, the MARFE phenomenon disappears, as can be seen

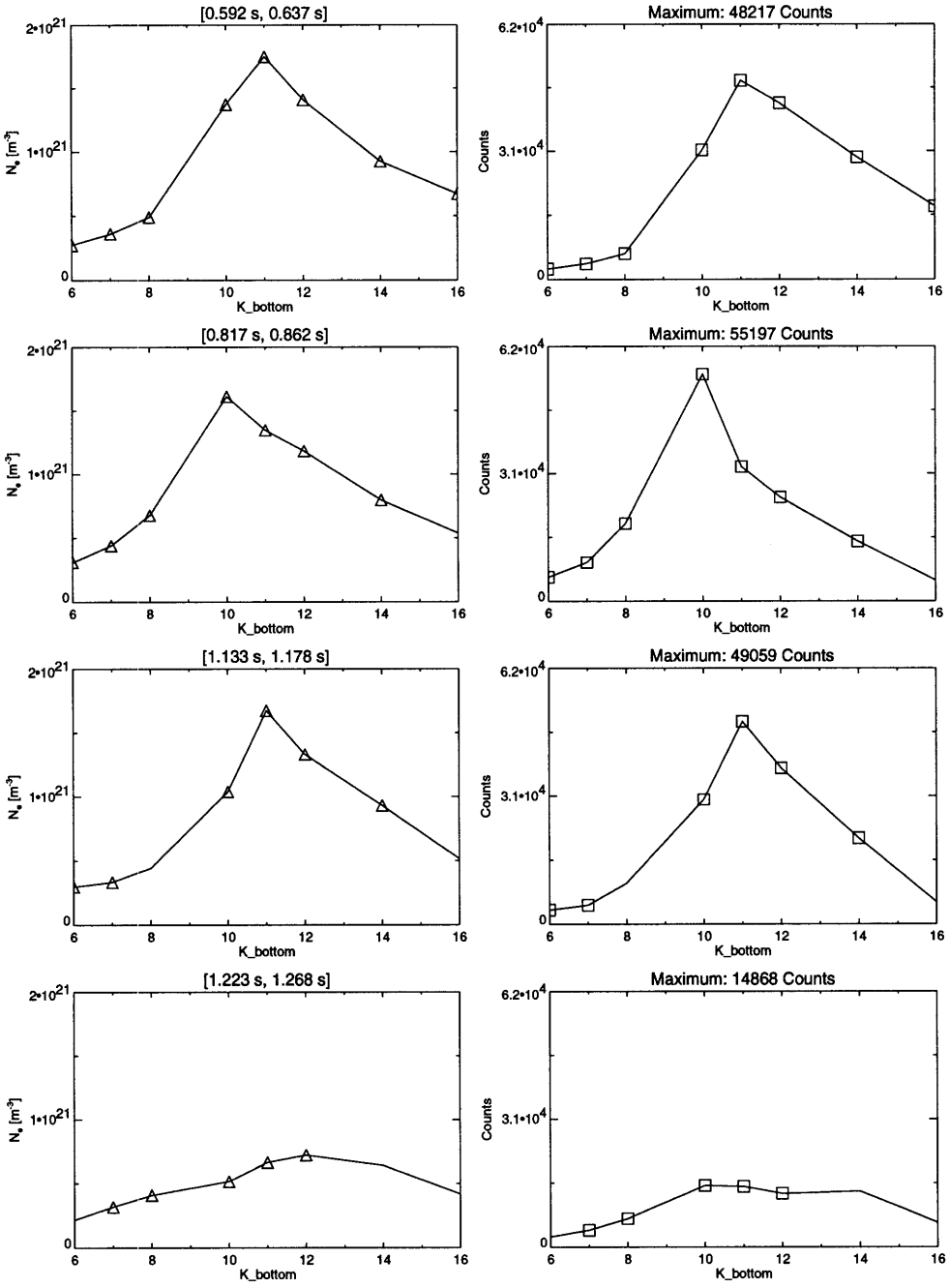

Figure 6-7: Spatial distribution of the electron density for a MARFE at the inner divertor in discharge 950503002. The left column shows the electron density as a function of the K_{bottom} fiber number for different time frames. The electron density was calculated using the 2–7-transition. The right column shows the spectrally integrated count rate of the 2–7-transition as a function of the K_{bottom} fiber number. The presence of a square or a diamond indicates the existence of data for the specific time frame. Its absence indicates that the data point provided is the result of interpolating between neighboring time frames.

in Fig. 6-6. This change is also reflected in the spatial electron density profile of Fig. 6-7. The profile develops a peak value of only $0.7 \cdot 10^{21}\,\mathrm{m}^{-3}$ and becomes broader with a spatial half width of 13.8 cm vertical poloidal extent.

6.3.2 MARFE at the Outer Divertor

The occurrence of a MARFE at the outer divertor allows us to compare the results from the Stark broadening analysis with the interferometer measurements since the vertical interferometer chords cover a region radially outward from the outer nose. The interferometer system is described in Ref. [10].

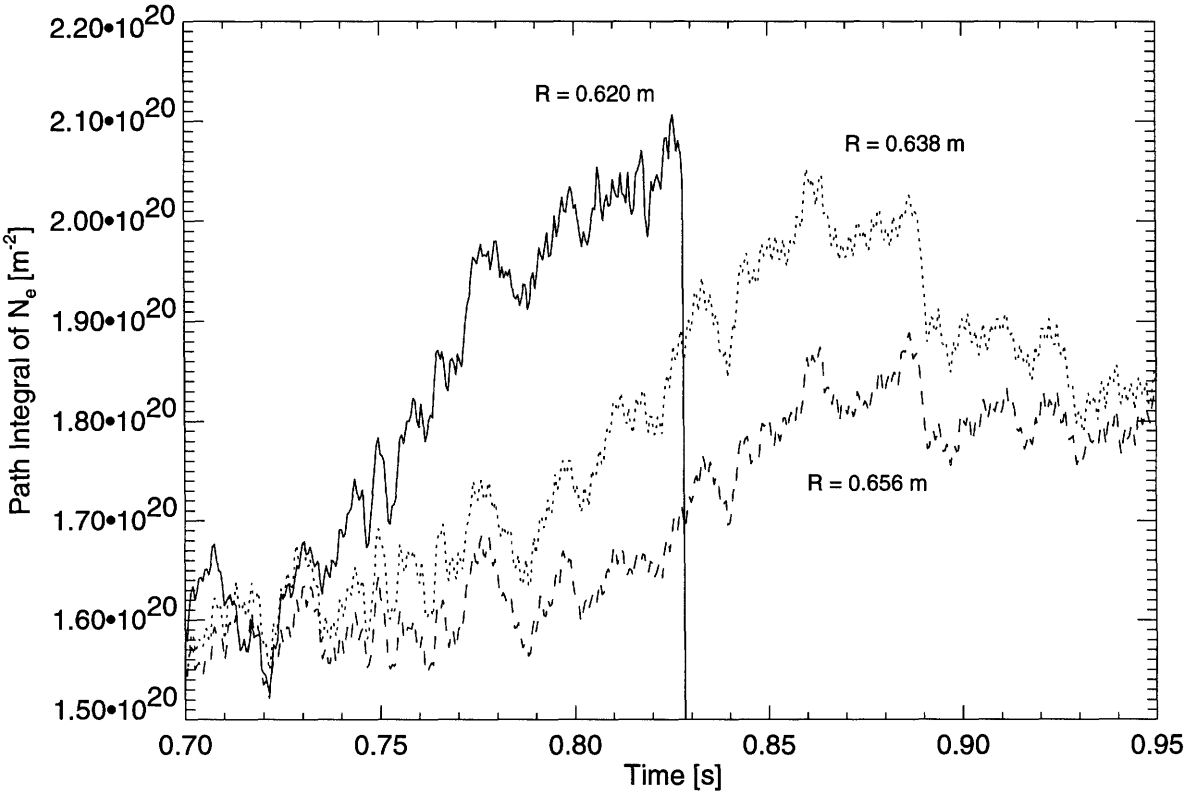

Figure 6-8: Observation of a MARFE at the outer divertor in discharge 950503012 using the interferometer: the path integral of the electron density as a function of time for the three innermost interferometer chords which are specified by their radial position.

Since MARFEs are localized objects of increased electron density, the occurrence of strong electron density gradients is necessarily implied by the existence of a MARFE. The angle of refraction α of an interferometer probing beam is calculated

from (see Ref. [22]) the path integral

$$\alpha = \int_{z_1}^{z_2} \frac{1}{N_e} \nabla N_e \, dz \; . \tag{6.1}$$

As a consequence, the interferometer probing beam can be refracted out of the field of its detector at the onset of a MARFE, as described in Refs. [14] and [15]. This effect can be observed in Fig. 6-8, where the signal of the innermost interferometer chord at $R = 0.62\,\mathrm{m}$ is lost at approximately 0.83 s.

The tomography for the same discharge is presented in Fig. 6-9. It shows a clearly localized high emissivity object intersected by the innermost interferometer chord. The interferometer data indicate the onset of the phenomenon at about 0.75 s. At that time, the tomography exhibits a broad peak at the position where the MARFE will be found later. After the onset of the phenomenon, the nearest neighbor chord is affected by the spatial tails of the localized object, as can be observed on both the emissivity and the interferometer data. From the interferometer data, one can conclude that the MARFE has completely disappeared at 0.95 s when the path integrals for several chords merge into one line. At that time, the tomography of the divertor region is almost identical to the one before MARFE onset.

Fig. 6-10 presents the spatial distribution of the electron densities calculated from Stark broadening and the line intensities on the K_{bottom} array for the same discharge. The data are provided for six time frames, four of which correspond to the tomography plots presented. Only the third and the fourth of the six frames present a physical situation where the MARFE is existent. Those two frames are different from all the others since both the electron density and the brightness profile exhibit two separate peaks. After the MARFE disappears, the profiles resemble closely the situation before its onset.

The spatial brightness profile extends to higher chords in the third and fourth frame, due to the development of a vertically elongated emissivity feature close to the inner divertor surface. The brightness originating from the MARFE at the outer divertor is centered around fiber K_{bottom} 10 within the error limits of the spatial accuracy.

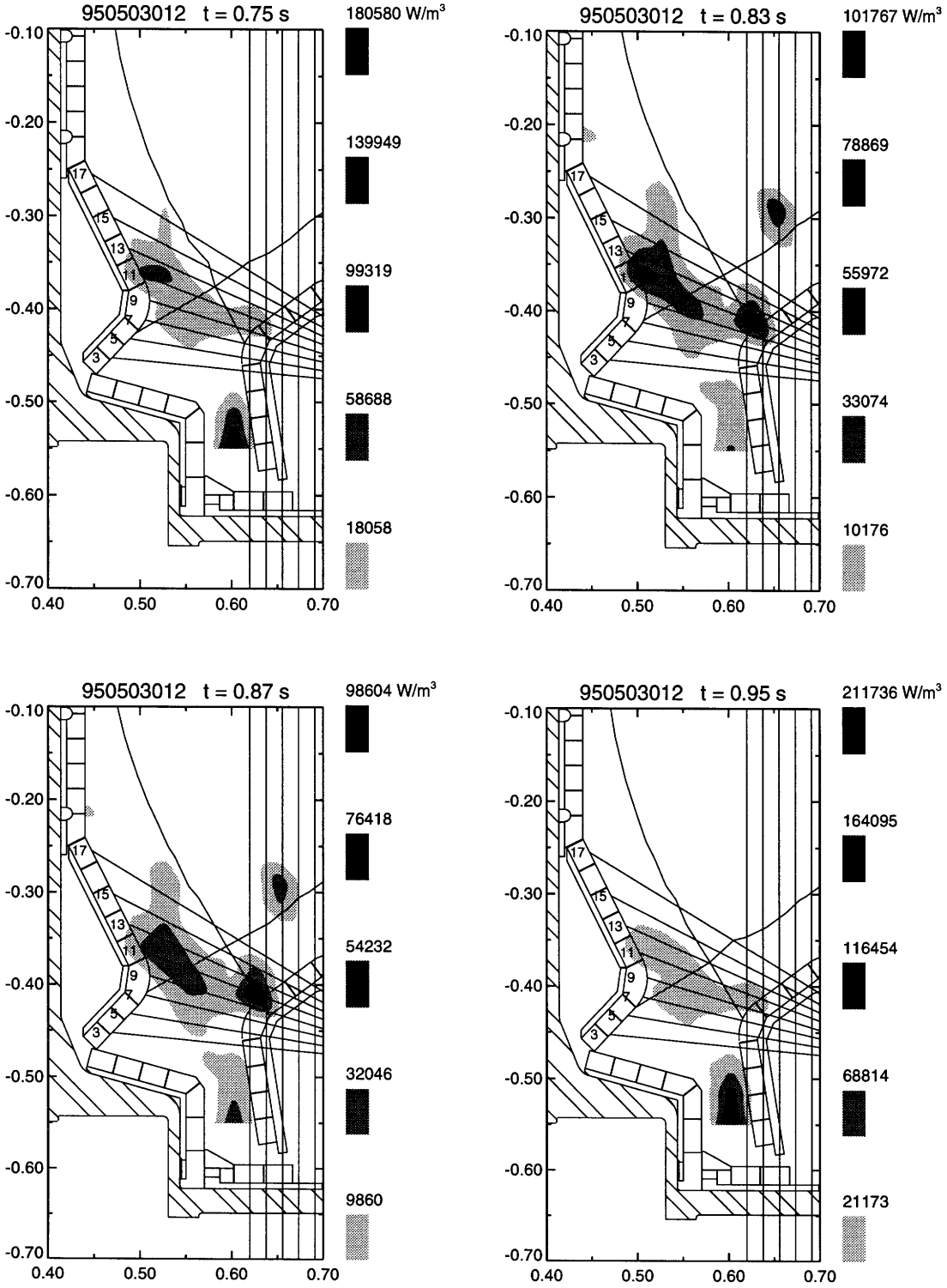

Figure 6-9: H_α tomography of a MARFE at the outer divertor. The approximate chords of the K_{bottom} fibers are drawn into the divertor geometry. The vertical lines indicate the interferometer chords.

Immediately before the loss of the innermost interferometer signal, the difference between the path integral of this chord and the one of its second nearest neighbor is about $0.38 \cdot 10^{20}\,\mathrm{m}^{-2}$. This second nearest neighbor chord is not affected by the MARFE, so the path integral difference can be attributed to the MARFE at the outer divertor. The spatial extent of the high emissivity region along the innermost interferometer path is about 2.5 cm. The average electron density of the MARFE is then approximately

$$N_{e,MARFE,Ifm} \approx 1.5 \cdot 10^{21}\,\mathrm{m}^{-3},$$

according to the combined information from the interferometer and the H_α tomography.

The electron density measurement based on Stark broadening leads to the result

$$N_{e,MARFE,Stark} \approx 1.5 \cdot 10^{21}\,\mathrm{m}^{-3},$$

for the fiber K_{bottom} 10 in the time frame [0.803 s, 0.848 s]. For this measurement, the uncertainties calculated in chapter 5 apply. Interpreting $N_{e,MARFE,Stark}$ as the bulk electron density of the outer divertor MARFE assumes that the dominant contribution to the signal on that fiber is due to the MARFE at the outer divertor.

This assumption is justified since the other radiating regions crossed by that chord — regions close to the inner divertor — are of intermediate emissivity only. In addition, the less peaked MARFE phenomenon occurring simultaneously at the inner divertor exhibits electron densities which differ from $N_{e,MARFE,Stark}$ by less than 15%, as can be seen on the fibers K_{bottom} 10–11 in the time frame [0.713 s, 0.758 s], Fig. 6-10.

6.4 Summary of the Physical Results

This thesis has presented a method for obtaining the electron density from the spectral line shape of high-n Balmer transitions emitted by a hydrogenic plasma. An error analysis has determined the overall uncertainty of the electron density measurement to be smaller than $\pm 19\%$ for electron densities higher than $3 \cdot 10^{20}\,\mathrm{m}^{-3}$, assuming

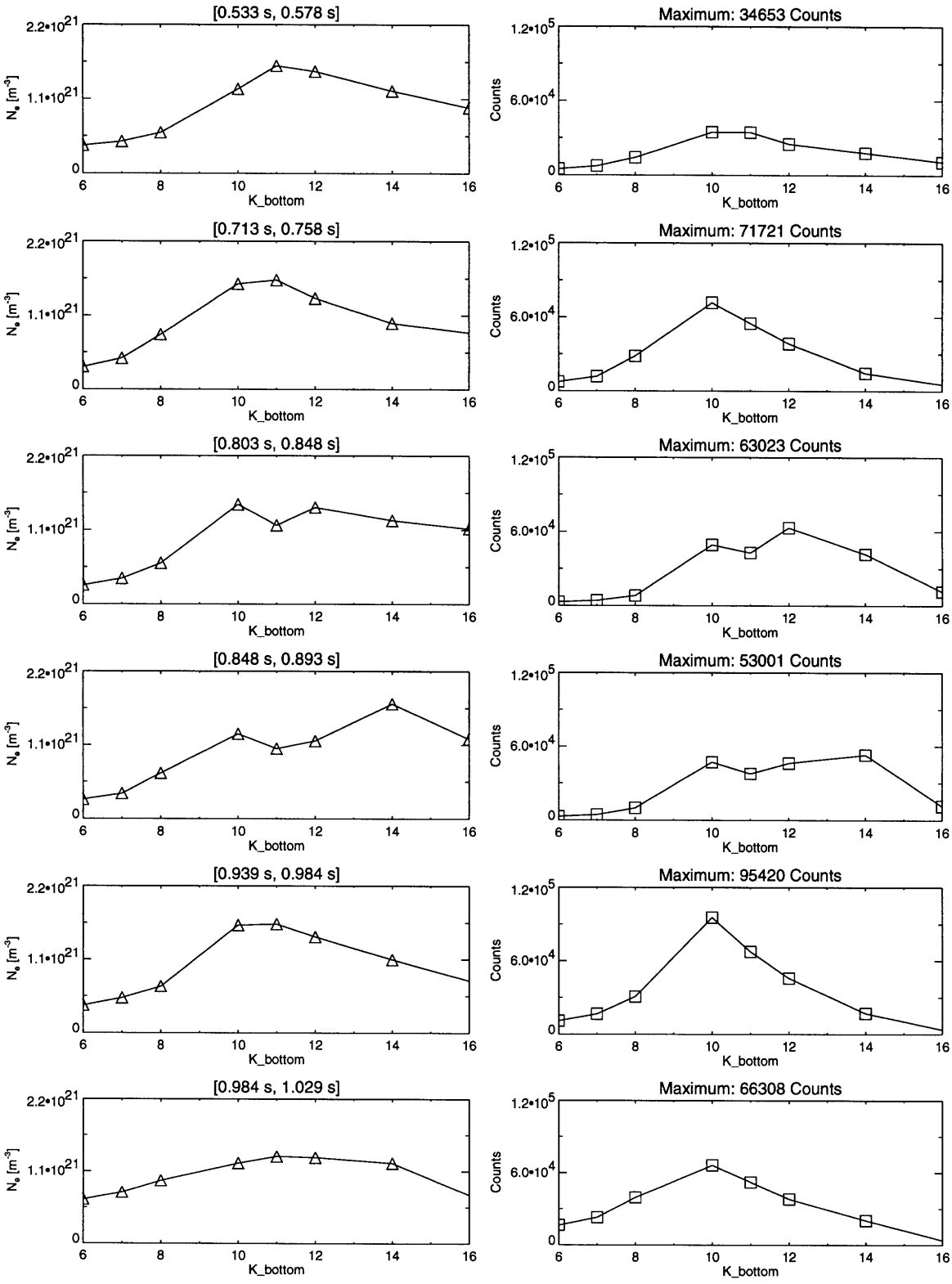

Figure 6-10: Spatial distribution of the electron density for a MARFE at the outer divertor in discharge 950503012. These plots are generated in the same way as the ones in Fig. 6-7.

homogeneous electron and neutral densities along the light path and excluding errors in the theoretical Stark broadening parameter $\alpha_{1/2}$.

A quantitative analysis provided in Appendix C leads to the conclusion that in almost all the cases, the signal on the outer divertor fibers will be dominated by radiative contributions which originate close to the inner divertor and which are reflected into the outer divertor. For this reason, one cannot expect a correlation between the outer divertor probe densities and the electron densities obtained from the Stark broadening analysis of the signal on the outer divertor fibers. The quantitative analysis is based on a measurement of the reflective properties of the divertor surfaces.

It has been demonstrated on the basis of a numerical model that the result obtained by the Stark broadening method is very sensitive to variations of the neutral and the electron density along the light path. In many cases, H_α tomography can be used to determine the dominating emissivity region, thereby allowing the assignment of the electron density obtained from the Stark broadening analysis to a restricted area on the poloidal plane. The diagnostic presented in this thesis can thus be used in combination with H_α tomography for the measurement of the electron density in cases where regions of sharply peaked emissivity, intersected by the spectrometer chords, are present.

Using the Stark broadening analysis together with H_α tomography, spatial electron density profiles of a MARFE at the inner divertor have been presented. A peak electron density of approximately $1.7 \cdot 10^{21}\,\mathrm{m}^{-3}$ and a spatial profile width of about 8 cm were measured. After the MARFE disappears from the tomography, the electron density profile broadens significantly while the maximum density of the profile drops to about $0.7 \cdot 10^{21}\,\mathrm{m}^{-3}$.

The occurence of a MARFE at the outer divertor has made it possible to demonstrate the consistency between the interferometer measurements and the results obtained from the Stark broadening analysis. The peak electron density of a MARFE at the outer divertor was measured to be approximately $1.5 \cdot 10^{21}\,\mathrm{m}^{-3}$, according to both diagnostic techniques.

Appendix A

Notation for Physical Quantities and Mathematical Expressions

This appendix explains the notation which is used in more than one chapter of this thesis. The symbols defined and used in only restricted parts of this thesis are not listed.

A.1 Physical Quantities

a	Form parameter of Voigt profile
B	Magnetic field strength
D	Set of detector bins
$F^{B=0}(\vec{V}, w)$	Profile describing a Stark broadened Balmer transition in w-space in the absence of a magnetic field
$F^{Zeeman}(\vec{V}, w, \Delta w_{Zeeman})$	Profile describing a Stark broadened transition in w-space including Zeeman splitting due to a magnetic field
$\vec{G}$	Vector with free parameters for a preliminary numerical fit to a Gaussian
$\vec{i}$	Vector of count rates on detector bins for data points used by the numerical fitting procedure

I_{fit}	Interval in wavelength space *centered* around a particular transition and enclosing the data used for the numerical fitting
I_{max}	Interval in wavelength space used to determine the actual center of the transition
j	Index counting the number of iterations performed by the numerical fitting procedure; total angular momentum quantum number
l	Path integral parametrization; angular momentum quantum number
n	Principal quantum number of the initial state in a Balmer series transition of deuterium or hydrogen
N_e	Electron density
N_0	Neutral density
$r_{\delta\lambda}$	Indicator of the *maximal* electron density uncertainty due to data scatter in wavelength space around the numerically fitted profile
T	Neutral temperature
T_e	Electron temperature
$\vec{V}$	Free parameters of the function F^{Zeeman}: the form parameter $V_0 = a$, an overall multiplicative scale V_1, a constant term V_2, and the coefficient V_3 of a linear term
w	Frequency scaled by the Doppler width
$\vec{w}$	Vector of w-coordinates for the data used by the numerical fitting procedure
$\vec{W}$	Vector specifying the relative weights of data points during the functional fits

x	Positive non-zero integer referring to the detector bin position along the spectrally resolving dimension of the CCD
y	Positive non-zero integer referring to the detector bin position along the spatially resolving dimension of the CCD
$\alpha_{1/2}$	Theoretical Stark width
Δw_{Zeeman}	Zeeman splitting in w-space
$\vec{\lambda}$	Vector containing wavelengths corresponding to the fitted data points
$\lambda_{cal}(x,y)$	Calibration map predicting the spectral wavelength mapped onto detector bin (x,y)
λ_{chromex}	Spectrograph center wavelength, treated as a hardware setup parameter
$\Delta\lambda_G$	Total Gaussian width in wavelength space
λ_{spec}	Spectral wavelength
$\Delta\nu_{Doppler}$	Gaussian width in frequency space due to Doppler broadening
$\Delta\nu_G$	Total Gaussian width in frequency space
$\Delta\nu_{Instr,G}$	Gaussian width of the instrumental profile in frequency space

A.2 Mathematical Symbols

$\mathcal{N}$	Set of all positive non-zero integers
$\mathcal{R}$	Set of all real numbers
$\mathcal{R}_+$	Set of all positive non-zero real numbers

$\mathcal{Z}$	Set of all integers
$\setminus$	Set algebra: difference
$\{ \quad \}$	Set of elements
$\{x \mid \ldots \}$	Set consisting of all x such that ...
$\in$	Symbol: 'element of'
$\cup$	Symbol: 'union'
$\forall$	Universal quantifier: 'for all'
$[a, b]$	$\{x \in \mathcal{R} \mid a \leq x \leq b\}$

Appendix B

Calibration of the Spectrometer System

The *Chromex* spectrometer system consists of optical fiber connections between the tokamak diagnostic port and the spectrograph entrance slit, the spectrograph itself, and the detector attached to the exit plane of the spectrograph. The calibration process for this system is separable into two parts: wavelength and intensity calibration.

B.1 Wavelength Calibration

During the standard measurement procedure, the entire wavelength configuration is defined by only two hardware parameters: the spectrograph center wavelength λ_{chromex} and the grating that is chosen. On the basis of these two parameters and the calibration data, the analysis software must be able to determine the spectral wavelength corresponding to each bin on the detector plane. In order to fulfill this task, the wavelength calibration must contain information about the absolute wavelength calibration of a reference bin on the detector, the dispersion as a function of the wavelength, and an effect which will be denoted as *aberration*. All these phenomena have to be quantified for each of the three gratings implemented in the spectrograph. A quantitative description of the aforementioned effects is found below.

B.1.1 Terminology for the Wavelength Calibration

The output of the *Chromex* spectrometer system is a digitized signal in the form of a 2-dimensional array of the size $(1242, 14)$. A bin on the detector plane is denoted by a vector

$$(x, y) \in D \equiv \{(a, b) \,|\, a, b \in \mathcal{N};\, 1 \leq a \leq 1242,\, 1 \leq b \leq 14\}\,. \tag{B.1}$$

A *wavelength configuration* Λ consists of a chosen grating and a given spectrograph center setting λ_{chromex}:

$$\Lambda \equiv \{\lambda_{\text{chromex}}, grating\}\,. \tag{B.2}$$

The detector center bin is denoted by the vector $(x_c, y_c) = (621, 7)$. The detector center bin row, given by $(x, 7) \in D$, will be denoted by the shorthand '$y = 7$'. Similarly, '$x = x_0$' shall refer to the detector column $(x_0, y) \in D$.

The spectrograph center wavelength λ_{chromex} will be treated here solely as a hardware parameter with the units of [nm]. It does not correspond to a physical wavelength. In contrast, the spectral wavelength λ_{spec} will denote the actual physical wavelength of a spectral line under observation: λ_{spec} is the wavelength which is mapped onto the detector bin (x_{spec}, y_{spec}) by the optical system for a fixed $\{\lambda_{\text{chromex}}, grating\}$.

Finally, $\lambda_{\text{cal}}(\lambda_{\text{chromex}}, (x, y))$ is the mapping which constitutes the wavelength calibration of the detector. Ideally, we would have

$$\lambda_{\text{spec}} = \lambda_{\text{cal}}(\lambda_{\text{chromex}}, (x_{spec}, y_{spec})). \tag{B.3}$$

B.1.2 Absolute Wavelength Calibration

The center bin of the detector is chosen to be the reference bin for the absolute wavelength calibration. The first step of the calibration is the determination of the actual spectral wavelength λ_{spec} which is mapped onto the detector center bin for a given setting λ_{chromex} of the spectrograph center wavelength and for a fixed grating. This is accomplished by observing a number of spectral lines and choosing the spectrograph center wavelengths λ_{chromex} so that the peaks of these spectral lines appear on the

center bin of the CCD detector. During this procedure, the final spectrograph center wavelength is always approached from an initial spectrograph center wavelength that lies at least 200 nm lower. This constraint ensures that the backlash of the spectrograph mechanics, which leads to a hysteresis of about 3 nm, does not have any effect on the absolute calibration. For the same reason, the destination in wavelength space has to be reached in the same manner during the standard operation of the instrument.

Element	Wavelength [nm]	Order
Hg	253.652	1
Hg	365.015	1
Hg	404.656	1
Hg	435.833	1
H_β	486.133	1
Hg	507.304	2
Hg	546.074	1
H_α	656.279	1
Hg	730.030	2
Hg	809.312	2
Hg	871.666	2
H_β	972.266	2
Hg	1092.148	2
Hg	1213.971	3
H_α	1312.559	2

Table B.1: Spectral lines used for the wavelength calibration.

For the wavelength calibration, low-pressure mercury and hydrogen lamps were used. Table B.1 contains a list of the specific spectral lines of these lamps, including the diffraction order for which the above procedure was performed. For the spectral line information, Refs. [21] and [23] were used.

The absolute wavelength calibration of the detector center bin showed that, for a given grating, the actual spectral wavelength λ_{spec} mapped onto the center bin could approximately be described by a constant offset from the spectrograph center wavelength λ_{chromex}. This can be seen in Fig. B-1. The offset for the different gratings scales approximately as the inverse of the number of grooves per unit length: 4.2 nm for the 600 mm^{-1} grating, 2.1 nm for the 1200 mm^{-1} grating, and 1.3 nm for

the $1800\,\mathrm{mm}^{-1}$ grating. The absolute wavelength calibration was performed down to 253.65 nm for all the gratings, while its limits in the long wavelength region were given by the sensitivity of the different gratings. It proved to be possible to calibrate the $600\,\mathrm{mm}^{-1}$ grating up to 1312 nm, the $1200\,\mathrm{mm}^{-1}$ grating up to 1092 nm, and the $1800\,\mathrm{mm}^{-1}$ grating up to the H_α line at 656 nm. The inversion of Fig. B-1 leads to the function $\lambda_{\mathrm{spec}}(\lambda_{\mathrm{chromex}})|_{x=621,y=7,grating}$, which will be needed for the calculation of the calibration map.

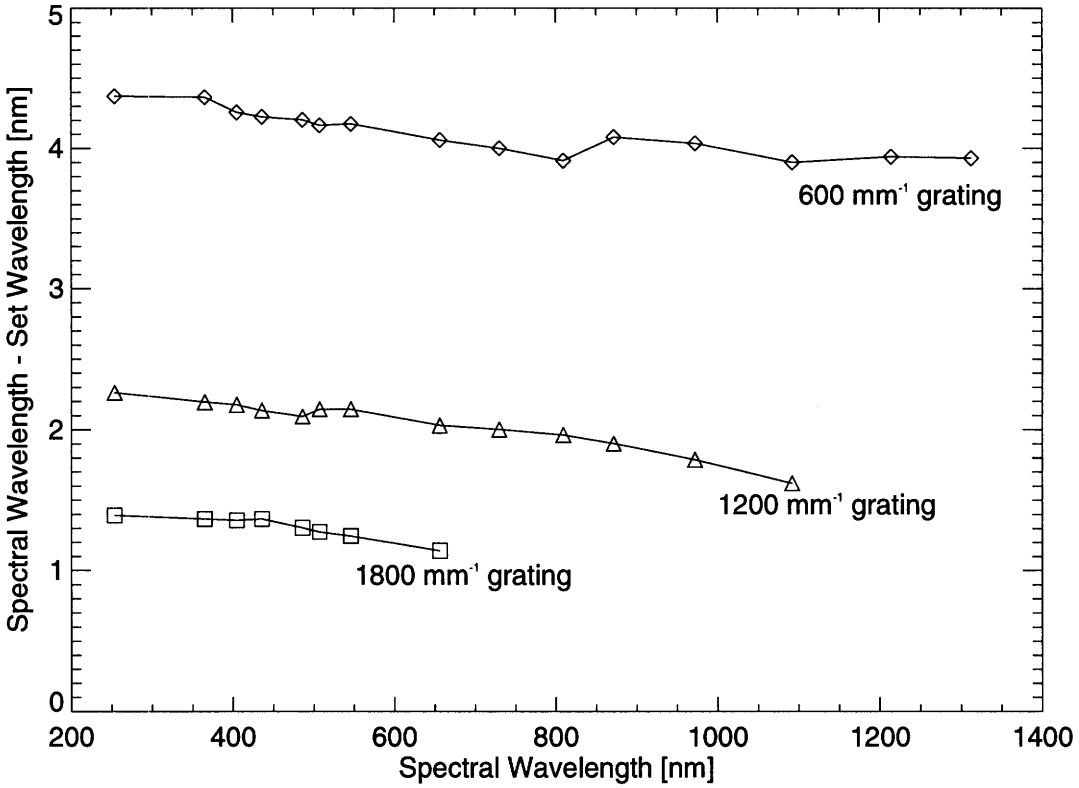

Figure B-1: Absolute wavelength calibration of the detector center bin: The difference $\lambda_{\mathrm{spec}} - \lambda_{\mathrm{chromex}}$ as a function of λ_{spec} for all the three gratings.

B.1.3 Dispersion

As the second step of the absolute wavelength calibration, the dispersion of the different gratings has to be measured on the central $y = 7$ bin row of the detector. In order to predict the spectral wavelength corresponding to each bin on the detector for a given configuration, the dispersion of the instrument must be measured. In principle,

this dispersion can be a function of the spectral wavelength and also of the position on the detector plane. The wavelength calibration performed here assumes that the dispersion of the instrument is constant across the entire CCD detector for a given spectral wavelength and grating. A consistency check of this assumption will be done later in this chapter as part of the aberration analysis.

The dispersion of the instrument is measured as a function of spectral wavelength for all three gratings at the center bin of the detector. In order to measure the dispersion at a specific spectral wavelength λ_{spec}, the spectrograph center wavelength λ_{chromex} is first chosen such that the line peak lies on the bin $(631, 7)$. Let this initial spectrograph center wavelength be denoted by $\lambda_{\text{chromex, initial}}$. Then the spectrograph center wavelength will be continuously increased, using the manual step function of the spectrograph, up to the point where the line peak lies on the bin $(611, 7)$. Denoting this final spectrograph center wavelength $\lambda_{\text{chromex, final}}$, the dispersion Δ at the center bin for the spectral wavelength λ_{spec} will be given by

$$\Delta(\lambda_{\text{spec}})\Big|_{x=621,y=7} = \frac{\lambda_{\text{chr, final}} - \lambda_{\text{chr, initial}}}{20}. \tag{B.4}$$

Here we use that

$$\frac{d\lambda_{\text{spec}}}{d\lambda_{\text{chromex}}} \approx 1\ , \tag{B.5}$$

which can be extracted from Fig. B-1.

The result of the dispersion measurement is shown in Fig. B-2. The dispersions of the different gratings are seen to be constant versus wavelength to a first approximation. The values of these constants scale as the inverse of the number of grooves per unit length, as expected. The dispersion measurement for the different gratings was only done in the same wavelength ranges as the absolute wavelength calibration described above.

Uncertainty of the Dispersion Measurements

For an error analysis of the application presented in this thesis, it will be useful to know the uncertainty in the dispersion measurements.

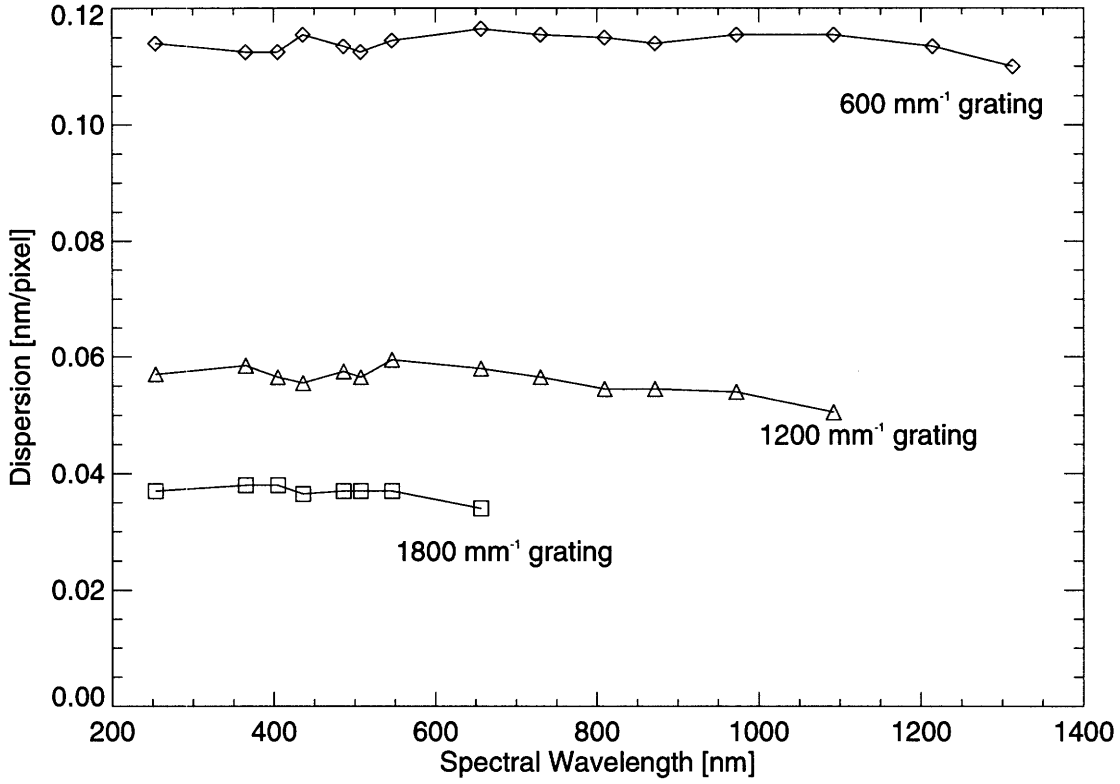

Figure B-2: Dispersion at the detector center bin.

For each grating, the dispersion is roughly constant as a function of wavelength. The uncertainty in the dispersion measurement will thus be of the order of the standard deviation of the measurements over wavelength. The relative uncertainty of the measurement is then taken to be the ratio between this standard deviation and the average dispersion.

The average dispersion $\overline{\Delta}$, the standard deviation σ_Δ of the dispersion, and the relative uncertainty are listed in table B.2 for all the three gratings.

Grating [mm^{-1}]	$\overline{\Delta}$ [nm / pixel]	σ_Δ [nm / pixel]	Relative Uncertainty [%]
600	0.114	0.00163	1.4
1200	0.056	0.00224	4.0
1800	0.037	0.00117	3.2

Table B.2: The estimated uncertainty in the dispersion measurements presented in Fig. B-2. Listed are the average dispersion $\overline{\Delta}$, the standard deviation σ_Δ, and the relative uncertainty of the dispersion for all the three gratings.

B.1.4 Mapping of Spectral Wavelengths onto Detector Pixels

Using the two wavelength calibration measurements and the information contained in the wavelength configuration, it is possible to calculate the spectral wavelength corresponding to every bin on the $y = 7$ bin row of the CCD detector. I will assume that the dispersion for a specific grating is only dependent on the observed spectral wavelength λ_{spec} and independent of the detector bin (x, y) onto which this spectral wavelength is mapped:

$$\begin{aligned} &\forall \lambda_{\text{spec}} \in \{\lambda | 200\,\text{nm} \leq \lambda \leq 1400\,\text{nm}\} \\ &\forall x \in \{1, \ldots, 1242\} \quad \forall y \in \{1, \ldots, 14\} : \\ &\qquad \Delta(\lambda_{\text{spec}})\big|_{x,y} = \Delta(\lambda_{\text{spec}})\big|_{x=621,y=7} \,. \end{aligned} \tag{B.6}$$

We want to calculate the function $\lambda_{\text{cal}}(\lambda_{\text{chromex}}, (x, y = 7))$ for a fixed λ_{chromex} and for a chosen grating. To first order in x, one can write a linear approximation:

$$\begin{aligned} \lambda_{\text{linear}}(\lambda_{\text{chromex}}, (x, y = 7)) \;=\; & \lambda_{\text{spec}}(\lambda_{\text{chromex}}, (x = 621, y = 7)) \\ & + (x - 621)\, \Delta(\lambda_{\text{spec}})\big|_{x=621,y=7} \,, \end{aligned} \tag{B.7}$$

where $\lambda_{\text{linear}}(\lambda_{\text{chromex}}, (x, y = 7))$ denotes a first approximation of the desired calibration map $\lambda_{\text{cal}}(\lambda_{\text{chromex}}, (x, y = 7))$ for a specific grating.

All quantities on the right hand side of equation B.7 have been measured in the wavelength calibration process: $\lambda_{\text{spec}}(\lambda_{\text{chromex}}, (x = 621, y = 7))$ is the result of the absolute wavelength calibration of the center bin, given for all three gratings in Fig. B-1; $\Delta(\lambda_{\text{spec}})|_{x=621,y=7}$ is the wavelength dependent dispersion at the center bin of the detector, given in Fig. B-2 for all three gratings.

Using the linear approximation and the assumption B.6, the wavelength calibration map can be calculated with yet higher precision:

$$\begin{aligned} \lambda_{\text{cal}}(\lambda_{\text{chromex}}, (x, y = 7)) \;=\; & \lambda_{\text{spec}}(\lambda_{\text{chromex}}, (x = 621, y = 7)) + \\ & \int_{621}^{x} \Delta\left(\lambda_{\text{linear}}(\lambda_{\text{chromex}}, (x', y = 7))\right)\big|_{x=621,y=7} dx' \,. \end{aligned} \tag{B.8}$$

Thus, the calibration data taken are sufficient to predict the correspondence between the spectral wavelength and the bin $(x, 7)$ of the detector.

B.1.5 Aberration

The CCD detector of the *Chromex* system is planar. In addition, the entrance slit of the spectrograph is a line, not the section of a circle, so that the spectrograph optics maps a *linear* entrance slit onto an exit *plane*. Using an optical system such as the one described in chapter 2, the image of the slit will generally appear as a section of a circle on the exit plane, not as a straight line. The smaller the instrument, the stronger this effect will be. Therefore, a quarter-meter instrument such as the one used here will be particularly affected by this phenomenon.

Due to this effect, the wavelength calibration of the $y = 7$ center bin row does not, in principle, apply to the other rows. The deviation of the wavelength calibration for the $y = 7$ row from the calibrations for the $y \neq 7$ rows will be referred to as *aberration* below. It should be understood that the aberration of the instrument optics affects both the absolute wavelength calibration of the $y \neq 7$ rows and the dispersion of those rows. So in principle, all the above measurements which were carried out for the $y = 7$ detector row would have to be done for the other rows as well.

In the following, it is to be understood that we keep the grating unchanged. Let us define λ_{spec} to be the spectral wavelength that is mapped onto the detector bin $(x, y = 7)$ for the spectrograph center wavelength λ_{chromex}. We can only have two independent variables among the three parameters: detector position $(x, y = 7)$, spectrograph center wavelength λ_{chromex}, and spectral wavelength λ_{spec}. For the purposes of the aberration analysis, λ_{spec} and $(x, y = 7)$ will be treated as the independent variables. We then write

$$\lambda_{\text{chromex}} \equiv \lambda_{\text{chromex}}(\lambda_{\text{spec}}, (x, y = 7), grating). \tag{B.9}$$

The constraint that λ_{spec} is mapped onto bin $(x, y = 7)$ implicitly defines the spectrograph center wavelength λ_{chromex} uniquely.

Let us consider two different wavelength configurations:

$$\begin{aligned} \Lambda_{center} &= \{\lambda_{\text{chromex}}(\lambda_{\text{spec}}, (x, y_{center} = 7)), grating\}, \\ \Lambda_{aberration} &= \{\lambda_{\text{chromex}}(\lambda_{\text{spec}}, (x, y_{aberration})), grating\}. \end{aligned}$$

Here we are stipulating that, for the same grating, the spectral wavelength λ_{spec} is mapped onto the $(x, y_{center} = 7)$ bin in the configuration Λ_{center} and onto the $(x, y_{aberration})$ bin in the configuration $\Lambda_{aberration}$.

These two configurations will in general not have the same λ_{chromex}, even though one does observe identical spectral wavelengths on the same bin column x with the same grating. This is the case because the angular geometry of the system {slit - grating - bin} can vary considerably between Λ_{center} and $\Lambda_{aberration}$ if $y_{aberration} \neq 7$. The aberration will then be defined as

$$\begin{aligned} \vartheta(\lambda_{\text{spec}}, (x, y_{aberration}), grating) \equiv \\ \lambda_{\text{aberration}}(\lambda_{\text{spec}}, (x, y_{aberration}), grating) - \\ \lambda_{\text{cal}}\left(\lambda_{\text{chromex}}(\lambda_{\text{spec}}, (x, y = 7), grating), (x, y = 7), grating\right), \end{aligned} \tag{B.10}$$

where $\lambda_{\text{aberration}}(\lambda_{\text{spec}}, (x, y_{aberration}), grating)$ is the spectral wavelength that is mapped onto detector bin $(x, y_{aberration})$ by the same wavelength configuration which maps the spectral wavelength λ_{spec} onto detector bin $(x, y_{center} = 7)$. From this definition, it is evident that a complete knowledge of the aberration's functional and quantitative behavior within its parameter space allows one to calculate, for any row y, which spectral wavelength $\lambda_{aberration}$ is mapped onto which x-coordinate of that bin row.

The aberration ϑ is thus a variable in a 3-dimensional parameter space for each grating. ϑ has been measured for the $600\,\text{mm}^{-1}$ grating on a rectangular grid of 180 points in parameter space: for the 15 values of λ_{spec} given in table B.1, for $x \in \{10, 621, 1230\}$, and for $y_{aberration} \in \{1, 4, 11, 14\}$.

The measurement of ϑ is done by choosing the value for the spectrograph center wavelength $\lambda_{\text{chromex, center}}$ so that the peak of the spectral line at λ_{spec} lies on the detector center bin $P_1 = (x, y_{center} = 7)$. In a second procedure, using the manual step function of the spectrograph, the spectrograph center wavelength is changed to $\lambda_{\text{chromex, aberration}}$ so that the peak of the line at λ_{spec} lies on the center of the detector bin $P_2 = (x, y_{aberration})$. Then the aberration will be given by

$$\vartheta(\lambda_{\text{spec}}, (x, y_{aberration}), grating) = \lambda_{\text{chromex, aberration}} - \lambda_{\text{chromex, center}}. \tag{B.11}$$

The aberration measurements performed on the $600\,\mathrm{mm}^{-1}$ grating lead to two results:

- The absolute value of the aberration is always less than 0.25 nm. It therefore lies within the inaccuracy of the absolute wavelength calibration.
- It does not seem to be possible to find a theoretically predictable pattern for the aberration.

Since the aberration ranges within the uncertainties of the absolute wavelength calibration, it is legitimate to assume that it is zero without affecting the absolute wavelength calibration significantly. With this choice, the relative wavelength calibration is not affected. The small absolute value of the aberration across the detector also confirms the correctness of the previous assumption that the dispersion is solely a function of the spectral wavelength and not of the detector position.

In addition, a *recalibration* procedure is implemented by the data viewing and analysis software, which allows one to assign exact absolute spectral wavelengths to spectral line peaks. From the wavelength calibration of the center row, given by $\lambda_{\mathrm{cal}}\left(\lambda_{\mathrm{chromex}}, (x, y = 7), grating\right)$, and from the newly provided calibration data point, the software is able to extract a value for the aberration for each detector bin row. These 14 new calibration points are inserted into a data structure that is called each time data are viewed. Thereby, the entire wavelength calibration improves since the aberration data grid becomes less coarse.

B.1.6 Nominal Resolution

As the final part of the wavelength calibration, the nominal relative wavelength resolution of each grating is calculated. The results are given in Table B.3.

Grating [mm^{-1}]	W_{spec} [nm]	Nominal Resolution [Å]
600	141.0	2.68
1200	72.8	1.29
1800	45.5	0.79

Table B.3: Spectral band width and nominal resolution at 546 nm for the three gratings. The slit width was chosen to be $20\,\mu\mathrm{m}$.

In order to calculate the nominal resolution, the very bright visible mercury line at 546.074 nm was chosen. The light was provided by a mercury lamp. Accordingly, the spectrograph center wavelength was chosen to be $\lambda_{\text{chromex}} = 546\,\text{nm}$. Using the center bin row of the detector for this measurement, one can calculate the spectral band width W_{spec} from the wavelength calibration by taking the difference between the spectral wavelength mapped onto pixel $(x = 1242, y = 7)$ and the spectral wavelength mapped onto pixel $(x = 1, y = 7)$. The slit width was chosen to be $20\,\mu\text{m}$, the choice also used during the plasma operation of the instrument.

In order to determine the instrumental width, a raw count spectrum is taken using the $y = 7$ detector bin row. From that spectrum, the full width at half maximum δx of the spectral line in bin space is determined. The nominal resolution of the system is then calculated using

$$\rho_{nominal} = \frac{W_{spec}\,\delta x}{1242}. \tag{B.12}$$

This procedure is carried out for all three gratings.

Pressure and Doppler broadening of the mercury line were negligible effects in comparison to the instrumental broadening since a low-pressure and low-temperature lamp was used. The natural width of the line is negligible even compared to its Doppler broadening. Using a fixed slit width of $20\,\mu\text{m}$, the nominal width calculated is a grating specific characteristic of the *Chromex* instrument.

B.2 Intensity Calibration

The intensity calibration provides the means to convert a raw detector count rate for a detector bin (x, y) to a physical brightness, given a wavelength configuration and a measurement of the background count rate.

Just as for the wavelength calibration, the first part of the intensity calibration involves the absolute calibration of the detector center bin. For this measurement, we will first be constrained to work with a fixed fiber optical reference connection between the tokamak diagnostic port and the spectrograph entrance slit. Initially, we will only consider a system consisting of this reference connection, the spectrograph itself, and

the detector center bin. λ_{spec} will again denote the spectral wavelength which is mapped onto the center bin by the optical system, consistent with the calibration map derived on the previous pages. This part of the calibration will be wavelength dependent, and it will result in the first order sensitivity curves of the system.

In addition, second and third order diffractions will be accounted for by measuring the wavelength dependent sensitivity of the system with respect to higher order diffractions. This will lead to an improvement of the sensitivity calculation for the three gratings.

This analysis must be repeated if any wavelength dependent optical device — such as a lens in the present case — is inserted into the optical path. Furthermore, a set of relative fiber attenuations must be measured for the fibers which are part of the bundle connecting the port window to the spectrograph input fiber bundle. These relative attenuation measurements were performed at one spectral wavelength only. Their spectral dependence is assumed to be identical since the fibers have the same length and are manufactured identically. Finally, a measurement of the relative sensitivity of detector bin (x, y) with respect to the center bin will allow one to generalize the intensity calibration to the whole detector plane.

B.2.1 Terminology for the Intensity Calibration

The background count rate $I_{background}(x, y)$ is measured before the beginning of the plasma discharge. For the detector temperature adjustment to $-25°$ Celsius, one finds an approximately constant background count rate of about 120 counts per bin per 45 ms. The noise on this signal is characterized in chapter 5 of this thesis. The array of background count rates is subtracted from all the raw data frames $I_{raw,frame}(x, y)$ taken at later times during the measurement. The remaining difference $I_{counts,frame}(x, y)$ constitutes an array that contains only count rates due to the incoming radiation.

The intensity calibration software generates a conversion array $R(x, y)$ whose elements are in units of $[\,\mathrm{mW\,s/\,cm^2\,sterad\,counts}\,]$. $R(x, y)$ is the inverse sensitivity that applies to the detector bin (x, y), and it is strongly dependent on the wavelength

configuration. The brightness $B_{frame}(x,y)$ of the signal is then calculated using

$$B_{frame}(x,y) = R(x,y)\,[I_{raw,frame}(x,y) - I_{background}(x,y)]\ . \qquad \text{(B.13)}$$

The brightness has units of $[\,\mathrm{mW/\,cm^2\,sterad}\,]$. The intensity calibration is thus reduced to the measurement and calculation of $R(x,y)$.

B.2.2 Calibration Source

The light source for the intensity calibration is provided by a six inch uniform source, model US-060-SF produced by Labsphere, Inc. It is a 45 Watt halogen lamp located in a sphere with a circular opening and with a spatially uniform output radiance.

The phototopic uniformity mapping of the circular sphere output area is provided by the manufacturer of the calibration source. The output is spatially uniform over the aperture within the range between 99.5% up to 100.1% of the center luminance. Therefore, the source output can be regarded as uniform for the given purposes, although an angular dependence of the radiance within the sphere is not specified.

The light source is driven by a halogen lamp power supply produced by the same company, model LPS-045-H. It is a precision regulated DC current source of 2.780 A with an error of 0.1% + 0.5 mA.

The spectral radiance of the continuum light source is calibrated between 300 nm and 2400 nm. This calibration is given in Fig. B-3 for the wavelengths in the range of interest. This function will be denoted by

$$\frac{dB_{source}(\lambda_{\mathrm{spec}})}{d\lambda}$$

in the following paragraphs. Its values are given in units of $[\,\mathrm{mW/\,cm^2\,sterad}\ \mu\mathrm{m}\,]$.

The spectral radiance of the light source decreases strongly below 400 nm. The detector count rates due to the incoming radiation in this region will become comparable to the background count rates. Due to the low radiance of the light source for spectral wavelengths below 400 nm, the intensity calibration for these short wavelengths is expected to be less reliable.

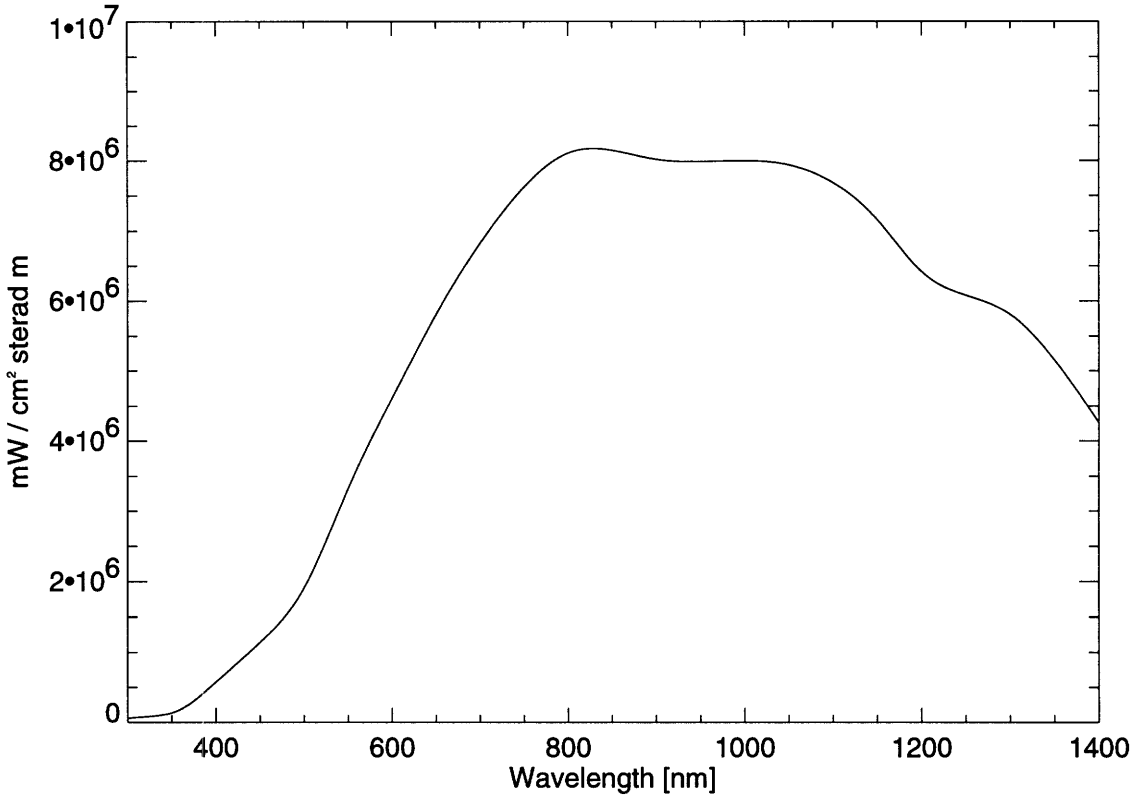

Figure B-3: Spectral radiance of the halogen lamp used for the absolute intensity calibration of the detector center bin: $\frac{dB_{source}}{d\lambda}$ as a function of λ_{spec}.

B.2.3 Sensitivity

As the first step in the absolute intensity calibration for the detector center bin, the inverse spectral sensitivity of the system has to be measured for each of the three gratings. Only taking the first order diffraction into account, the inverse spectral sensitivity is given by:

$$\frac{dR_{first}(\lambda_{\text{spec}})}{d\lambda} = \frac{dB_{source}(\lambda_{\text{spec}})}{d\lambda}\left[I_{counts}(\lambda_{\text{spec}})\right]^{-1}. \tag{B.14}$$

In order to get a quantitative result for this curve, one has to measure the quantity $I_{counts}(\lambda_{\text{spec}})$, which is the count rate on the detector center bin solely due to the external radiation influx. We assume a wavelength configuration such that the spectral wavelength λ_{spec} is mapped onto the detector center bin. The quantity $\frac{dB_{source}}{d\lambda}$ is given in Fig. B-3 as a function of spectral wavelength.

The measurement of $I_{counts}(\lambda_{\text{spec}})$ is performed by positioning the fiber bundle

input in the center of the calibration source output area. A reference connection between the periscope bundle and the spectrograph input bundle is chosen, and all other optical inputs are kept dark. The reference bin is chosen to be the detector center bin. The entire setup of the calibration source with the fiber bundle input is covered with black cloth so as to prevent room light from affecting the measurement.

To achieve a precision as high as possible, the effective integration time of the detector is increased to its sensitive maximum. The sensitive maximum is defined by the constraint that none of the detector pixels is allowed to be saturated.

At this point, it is essential that a distinction between a detector *pixel* and a detector *bin* be made. The optically sensitive area of the detector has 1242x576 pixels, but only 1242x14 bins in the measurement configuration currently used. A detector bin is a hardware average over 41 detector pixels along the spatially resolving dimension of the detector. The bin width of 41 pixels was chosen such that the mapping of fiber signals onto nearest neighbor positions on the detector does not lead to more than 1% of intensity overlap. The ranges of both the detector pixels and detector bins lie between zero counts and $(2^{16}-1)$ counts. Since the single detector pixels are averaged into bins, it is not immediately apparent from looking at the bin count rates when the pixel saturation level is reached. One can check whether the saturation is reached by switching off the hardware binning option and digitizing the whole detector screen of 1242x576 pixels.

The count rate on the center pixel is then measured for different spectrograph center wavelengths λ_{chromex}, first with the calibration lamp switched off in order to measure the background count rate, and then with the source turned on. The effective detector exposure time was set to the wavelength dependent sensitive maximum. These three data points then allow an immediate calculation of

$$I_{counts}(\lambda_{\text{spec}}(\lambda_{\text{chromex}})|_{x=621,y=7}) .$$

Armed with this result, the function

$$\left[\frac{dR_{first}(\lambda_{\text{spec}})}{d\lambda}\right]^{-1}$$

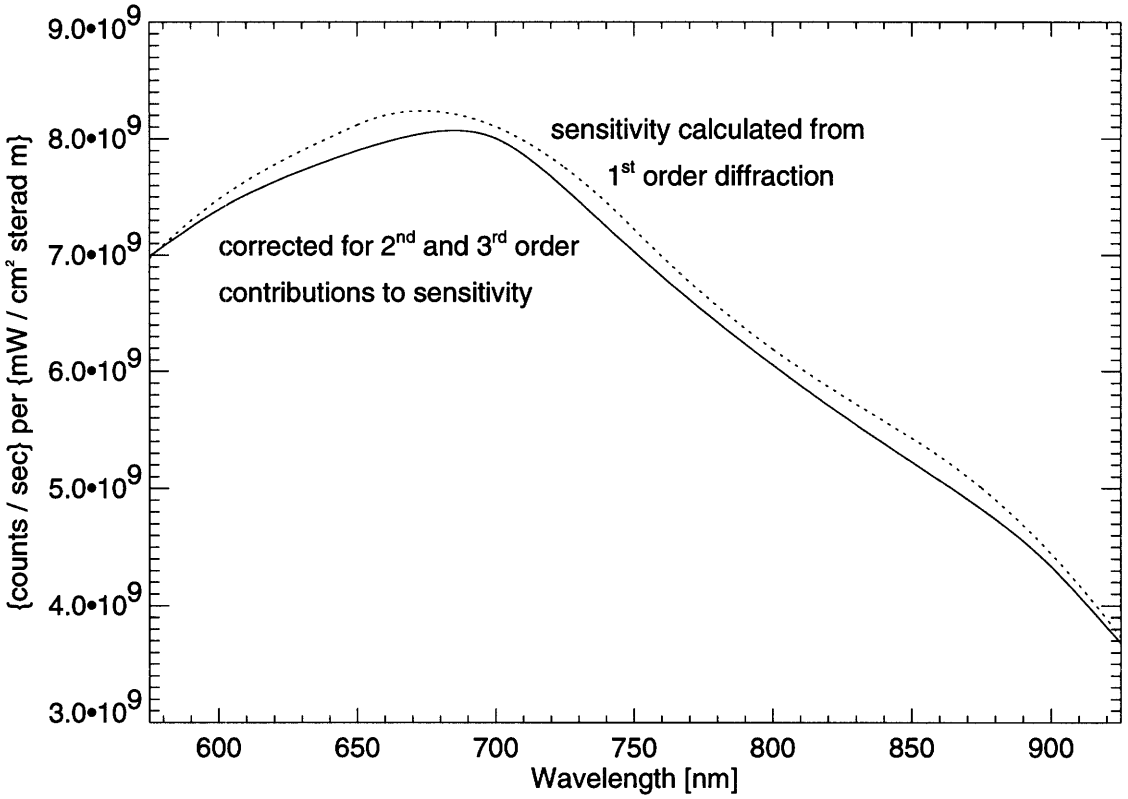

Figure B-4: Effect of 2^{nd} and 3^{rd} order diffractions on the sensitivity of the system {Reference Connection - Slit - Optics - Detector} for the $600\,\mathrm{mm}^{-1}$ grating: $\left[\frac{dR_{first}(\lambda_{\mathrm{spec}})}{d\lambda}\right]^{-1}$ and $\left[\frac{dR(\lambda_{\mathrm{spec}})}{d\lambda}\right]^{-1}$ as a function of spectral wavelength.

can be calculated. The result for the $600\,\mathrm{mm}^{-1}$ grating within a particular wavelength region is graphed as the dashed curve in Fig. B-4.

The range of the intensity calibration is determined by three considerations:

- The output of the calibration source has to be finite. This effect leads to limits in the short wavelength region.
- The optical sensitivity of the system has to be finite. This effect results in long wavelength limits.
- The range of the intensity calibration has to be a subspace of the range of the wavelength calibration.

As a result, an intensity calibration can be provided within the wavelength range

of [300 nm, 1400 nm] for the $600\,\mathrm{mm}^{-1}$ grating, within [400 nm, 1100 nm] for the $1200\,\mathrm{mm}^{-1}$ grating, and within [400 nm, 700 nm] for the $1800\,\mathrm{mm}^{-1}$ grating.

B.2.4 Higher Diffraction Orders

Assuming the spectral wavelength λ_{spec} is mapped onto the detector bin (x, y) by the spectrograph, the spectral wavelengths $\lambda_{\mathrm{spec}}/n$, with n an integer, will also be mapped onto the same detector bin (x, y). This is a direct effect of the grating equation leading to the dispersion of the instrument.

These higher diffraction orders have to be taken into account for the intensity calibration. The count rate measured on bin (x, y) will in principle be due to contributions from all diffraction orders. Practically, the first order dominates. For the given calibration, contributions up to the third order will be taken into account. The corrections will again be measured using the detector center bin and the calibration source. Then, up to third order, the inverse spectral sensitivity of the system can be calculated as follows:

$$\frac{dR(\lambda_{\mathrm{spec}})}{d\lambda} = \left[\frac{dB_{source}(\lambda_{\mathrm{spec}})}{d\lambda} + s_{21}(\lambda_{\mathrm{spec}})\frac{dB_{source}(\lambda_{\mathrm{spec}}/2)}{d\lambda} + s_{31}(\lambda_{\mathrm{spec}})\frac{dB_{source}(\lambda_{\mathrm{spec}}/3)}{d\lambda}\right][I_{counts}(\lambda_{\mathrm{spec}})]^{-1}\,. \quad \text{(B.15)}$$

Here, $s_{n1}(\lambda_{\mathrm{spec}})$ is the relative sensitivity of the nth diffraction order with respect to the first diffraction order, evaluated at the spectral wavelength λ_{spec} which is mapped onto the detector center bin. $s_{n1}(\lambda_{\mathrm{spec}})$ is the ratio between the count rate on the center bin due to $\lambda_{\mathrm{spec}}/n$ observed in nth order and the count rate due to λ_{spec} observed in first order.

For all measurements leading to $s_{n1}(\lambda_{\mathrm{spec}})$, only the detector center bin was of interest, and the reference connection was used. In a first measurement, the spectrograph center wavelength $\lambda_{\mathrm{chromex}}$ was chosen such that the first order peak of a spectral line at λ_{line} was mapped onto the center of the detector. After setting the detector exposure time to the sensitive maximum for λ_{line}, the center bin count rates were measured with and without radiation influx. Their difference yields $I_{count,1}$. In

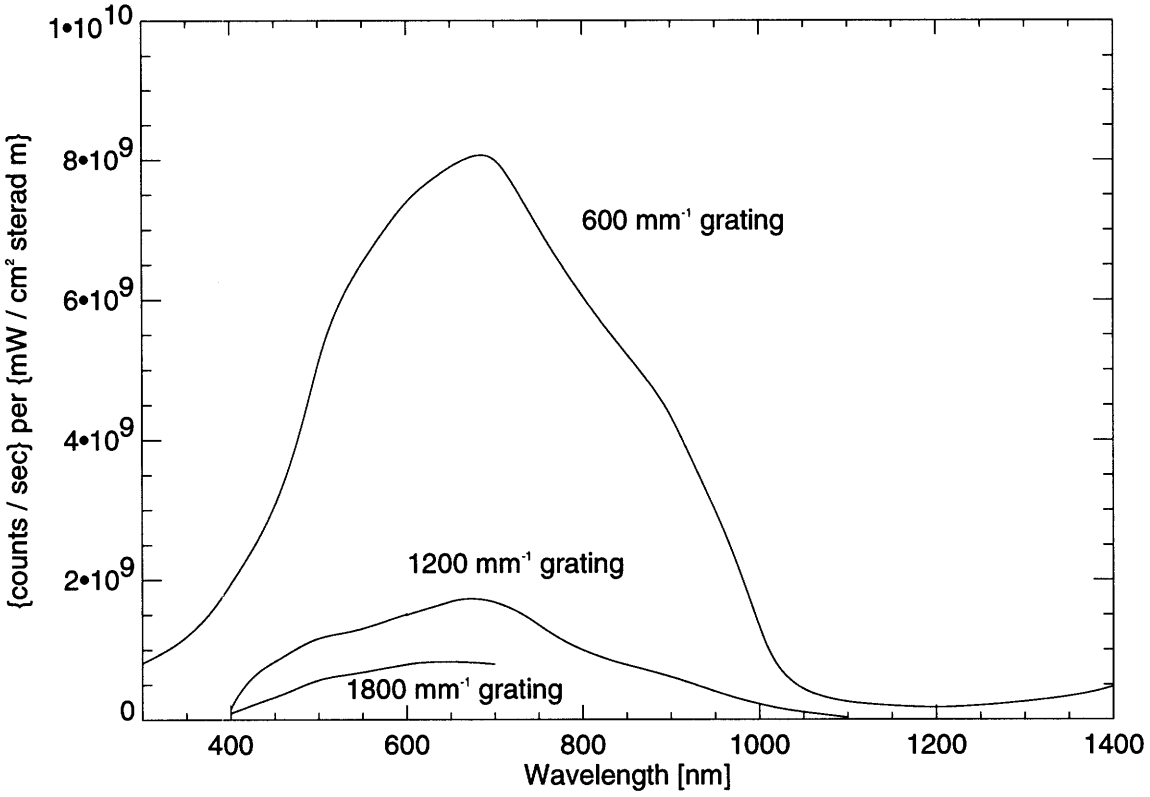

Figure B-5: Sensitivity of the system {Reference Connection - Slit - Optics - Detector} for the three gratings: $\left[\frac{dR_{grating}(\lambda_{\text{spec}})}{d\lambda}\right]^{-1}$ as a function of spectral wavelength.

a second measurement, λ_{chromex} was chosen such that the nth order peak of the same spectral line at λ_{line} was mapped onto the detector center. Again, after setting the detector exposure time to the sensitive maximum for $n\lambda_{\text{line}}$, the center bin count rates were measured with and without radiation influx, leading to $I_{count,n}$. These measurements then give:

$$s_{n1}(\lambda_{\text{spec}} = n\lambda_{\text{line}}) \equiv \frac{I_{count,n}}{I_{count,1}} \,. \tag{B.16}$$

For example, $s_{21}(871.67\,\text{nm}) = 0.0224$ for the $600\,\text{mm}^{-1}$ grating.

By definition, $s_{n1}(\lambda_{\text{spec}})$ is a non-negative quantity. Therefore:

$$\frac{dR(\lambda_{\text{spec}})}{d\lambda} \geq \frac{dR_{first}(\lambda_{\text{spec}})}{d\lambda} \Rightarrow \left[\frac{dR(\lambda_{\text{spec}})}{d\lambda}\right]^{-1} \leq \left[\frac{dR_{first}(\lambda_{\text{spec}})}{d\lambda}\right]^{-1} \,.$$

So the sensitivity curve of the system decreases after including the higher diffraction contributions to the detector count rate.

The effects of the higher order diffractions on the sensitivity can be seen in Fig. B-4 for the $600\,\mathrm{mm}^{-1}$ grating. The dashed curve is the first order sensitivity, the full curve includes higher order contributions. Both curves merge for $\lambda_{\mathrm{spec}} \leq 600\,\mathrm{nm}$ since the calibration source radiance approaches zero below that wavelength, so that the first order approximation is almost exact. For long wavelengths, the relative sensitivities $s_{n1}(\lambda_{\mathrm{spec}})$ are negligible, so that the two curves practically merge for $\lambda_{\mathrm{spec}} > 900\,\mathrm{nm}$.

The corrected sensitivities have been measured and calculated for the three gratings implemented in the spectrograph. The results can be found in Fig. B-5. The sensitivity curves share the feature of a global peak at approximately 675 nm.

B.2.5 Modifications in the Light Path

The absolute intensity calibration for the detector center pixel can be provided for the system {Reference Connection - Slit - Optics - Detector} as a function of wavelength. Any change in the light path will unavoidably lead to a correction factor in the intensity calibration.

Lenses

When a lens is inserted into the light path, the correction factor will become wavelength dependent. Since the lens is opaque for certain wavelength regions, the entire intensity calibration has to be repeated. Also, a lens introduces a specific wavelength dependent absorption coefficient into the system, so the sensitivity of the system will decrease. This can be seen in Fig. B-6, which allows a comparison between the spectral sensitivity of a particular grating with and without a lens in the light path.

Fiber Connections

When changing to a fiber connection differing from the reference connection used so far, the correction factor will be merely a constant overall factor. The assumption of wavelength independence is justified by the fact that the corresponding fibers have

the same length and are manufactured identically, implying the same wavelength dependent material properties. The correction factor is the relative attenuation of the new fiber connection with respect to the old one.

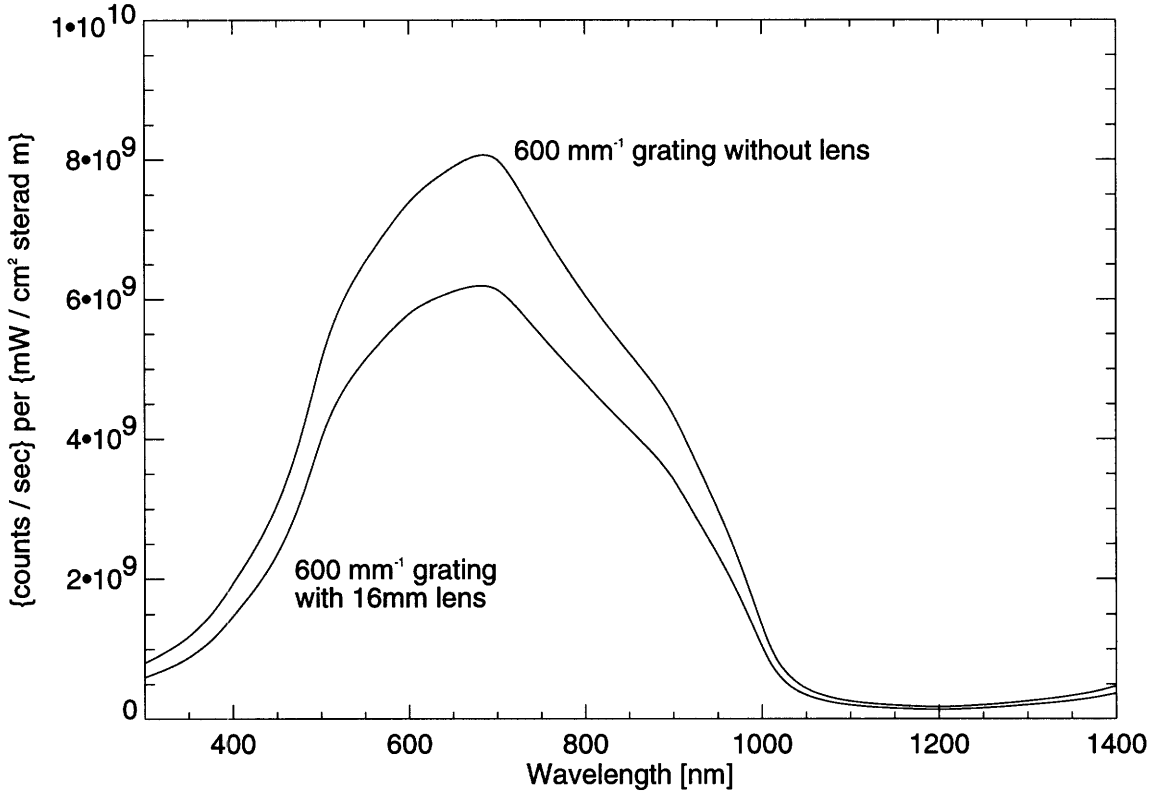

Figure B-6: Effect of inserting a lens on the sensitivity of the system {Reference Connection - Slit - Optics - Detector} for the 600 mm^{-1} grating: $\left[\frac{dR_{600}(\lambda_{\mathrm{spec}})}{d\lambda}\right]^{-1}$ as a function of spectral wavelength with and without the 16 mm lens.

The entire light path ending at a certain detector bin row $b \in \{1, 2, ..., 14\}$ is uniquely defined by specifying four parameters:

- The periscope view: $V_b \in \{A_{bottom}, K_{bottom}\}$
- The fiber i within the periscope bundle: $i_b \in \{1, 2, ..., 20\}$. It corresponds to an overall fiber specific attenuation factor A_{i_b}.
- The neutral density factor associated with the connection: n_b
- The spectrograph slit width w_{slit}.

Except for the slit width, which affects the signal on all bins equally, these parameters have to be specified for all 14 bins. The choice of the periscope view cannot affect the calibration since both periscopes are manufactured identically, so that the differences regarding their optical properties can be neglected for the given purposes. The choice of the periscope fiber can influence the calibration since the different fibers have different positions on the bundle input area. The positions of the detector bins have a strong influence on the calibration since the spectrograph optics tends to suppress the signal near the detector edges.

Different bins can have different neutral density filters, which reduce the signal and help avoid detector saturation. The factor n_b is the factor by which the signal on bin b is reduced due to this filter. It may be slightly wavelength dependent, but is usually constant versus wavelength to a very good approximation. $n_b(\lambda_{\text{spec}})$ is usually provided by the manufacturer of the filter.

Let us denote the reference connection for the intensity calibration by

$$\Gamma_{ref} \equiv \left\{ b_{ref} = 7, V_{b_{ref}} = A_{bottom}, i_{b_{ref}}, n_{b_{ref}} = 1 \right\} . \tag{B.17}$$

In addition, let the 3x14 array Φ describe the totality of all connection parameters $\{V, i, n\}$ for the 14 separate spatial bin rows. For the relative intensity calibration to be introduced later, one also needs to define a standard for these 3x14 connection parameters:

$$\Phi_{standard} \equiv \begin{pmatrix} V_{1,standard} & \cdots & V_{ref} & \cdots & V_{14,standard} \\ i_{1,standard} & \cdots & i_{ref} & \cdots & i_{14,standard} \\ n_{1,standard} & \cdots & n_{ref} & \cdots & n_{14,standard} \end{pmatrix} . \tag{B.18}$$

In general, an array describing the total set of connection parameters, structured like the one given here, will be denoted by Φ and will be referred to as the *intensity configuration*.

The attenuation factor A_i is defined to give the relative attenuation of fiber i in the periscope V_i with respect to the fiber $i_{b_{ref}}$ in the periscope $V_{b_{ref}}$. A_i is measured with the same experimental setup as the one used for the sensitivity measurements. The 20 count rates for all the connections $\Gamma_i = \{b_{ref} = 7, V_{b_{ref}} = A_{bottom}, i, n_i = 1\}$

must be measured. The measurements were performed on the detector center bin using the $600\,\mathrm{mm}^{-1}$ grating, a slit width of $20\,\mu\mathrm{m}$, and $\lambda_{\mathrm{chromex}} = 800\,\mathrm{nm}$. The exposure time is set to its sensitive maximum. From the count rates I_{ref} and I_i, A_i is calculated via:

$$A_i \equiv \frac{I_i}{I_{ref}} \; ; \; i \in \{1, \ldots, 20\} \; . \tag{B.19}$$

These measurements yield the result that

$$\forall i \in \{1, 2, ..., 20\} : 0.9805 \leq A_i \leq 1.0118 \; ,$$

implying that the assumption of identical fibers is completely justified. These relative attenuations have to be measured again for the case that a lens is inserted into the light path since the lens changes the spatial imaging of the light onto the different fibers.

After defining the intensity configuration, the analysis software is able to provide an intensity calibration for all wavelength configurations within the spectral ranges specified earlier. In fact, the intensity configuration is read by the analysis software from three nodes which are part of a database structured in the form of a hierarchical tree. These three nodes resemble the ordered structure of Φ.

B.2.6 Relative Sensitivity

The intensity calibration performed so far allows us to determine the inverse spectral sensitivity

$$\frac{dR(\lambda_{\mathrm{spec}})}{d\lambda}(\lambda_{\mathrm{spec}}) \tag{B.20}$$

at the detector center bin as a function of the spectral wavelength λ_{spec} for all three gratings. For a given wavelength configuration, we know the spectral band width W_{spec} defined in section B.1.6. Dividing W_{spec} by the number of detector bins along the spectrally resolving detector dimension, we obtain the width of one bin in wavelength space for the given wavelength configuration. We can then calculate the inverse sensitivity at the detector center:

$$R(\lambda_{\mathrm{spec}}) = \frac{dR(\lambda_{\mathrm{spec}})}{d\lambda} \frac{W_{spec}}{1242} \; . \tag{B.21}$$

For the discussion in this chapter, the spectral wavelength λ_{spec} and the detector bin (x, y) onto which it is mapped will be treated as independent parameters. The spectrograph center wavelength λ_{chromex} is then an implicitly dependent variable with a fixed value.

It is the aim of this section to generalize the applicability of the intensity calibration to the whole detector plane. This will be done by introducing the array $s(x, y)$ with $(x, y) \in D$. $s(x, y)$ is the relative sensitivity of detector bin (x, y) with respect to the center bin $(621, 7)$. This approach rests on the underlying assumption that there is a relative sensitivity function which is only dependent on the position on the detector plane, but independent of the wavelength configuration Λ.

The sensitivity array should ideally be determined by illuminating all fibers with the same optical input, by measuring the detector count rates on all the bins, and by normalizing. But the sensitivity of a detector bin is certainly dependent on the quantum efficiency of the detector pixels, which is inherently wavelength dependent. Hence, for this measurement, the spectral band width of the wavelength configuration has to be as small as possible so that the quantum efficiency shows only a small variation over the spectral band. Therefore, the $1800\,\text{mm}^{-1}$ grating is used for this measurement.

In addition, the center of the spectral band has to be chosen such that the continuum light source has an almost constant output over the spectral band. Based on Fig. B-3, the spectrograph center wavelength is then taken to be $\lambda_{\text{chromex}} = 910\,\text{nm}$.

With this wavelength configuration, the quantum efficiency is assumed to be constant for all detector bins (x, y). Furthermore, it is assumed that the spectral wavelengths mapped onto these bins are emitted with equal spectral radiance. Therefore, the count rate $I_{s,count}(x, y)$ will be a function characteristic for the properties of the optical system and the detector pixels averaged to the bin (x, y).

For this measurement, the same experimental setup as for the sensitivity measurements is chosen, except that the intensity configuration $\Phi_{standard}$ (see equation B.18) is applied, leading to a defined light input on all detector bin rows. Increasing the exposure time to its sensitive maximum and subtracting the background count rate,

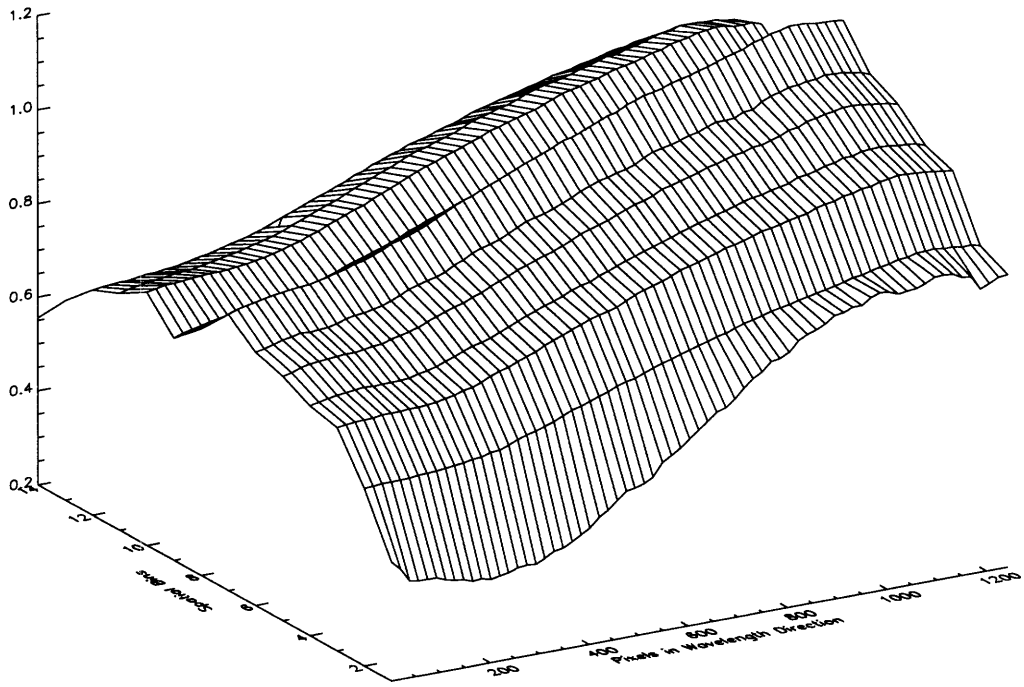

Figure B-7: The shape of the sensitivity factor: $s(x,y)$ as a function of the detector bin position (x,y).

one then obtains $I_{s,count}(x,y)$. The relative sensitivity results from normalization:

$$s(x,y) \equiv \frac{I_{s,count}(x,y)}{I_{s,count}(621,7)} \frac{1}{A_{i_y}} \Bigg|_{\Phi_{standard}} . \tag{B.22}$$

Thereby, $s(x,y)$ is normalized to unity for the reference bin $(621,7)$. Since corrections due to the relative fiber attenuations are also taken into account, $s(x,y)$ is solely a function characteristic for the system {Optics - Detector}.

A surface plot of the sensitivity factor can be seen in Fig. B-7. It is apparent that the sensitivity drops by factors up to three at the edges of the detector plane.

B.2.7 Overall Intensity Calibration

The entire intensity calibration is summarized by showing how the array $R(x,y)$, used for the conversion of raw data into calibrated data, can be calculated for a given specific wavelength configuration Λ (definition B.2) and for a specific intensity

configuration Φ (generalization of definition B.18). The raw count rates are converted to brightness values by equation B.13. The conversion array is given by

$$R_{\Lambda,\Phi}(x,y) = R_{lens,grating}\left(\lambda_{\text{cal}}\left(\lambda_{\text{chromex}}, (x,y), grating\right)\right) \frac{n_y}{A_{i_y}\, s(x,y)} \frac{20\,\mu\text{m}}{w_{slit}}\,, \quad \text{(B.23)}$$

where $\lambda_{\text{cal}}\left(\lambda_{\text{chromex}}, (x,y), grating\right)$ is provided by the wavelength calibration, n_y is a neutral density coefficient, and A_{i_y} is given in equation B.19. The inverse sensitivity $R_{lens,grating}(\lambda_{\text{spec}})$ can be calculated from equation B.21. The correction factor

$$\frac{20\,\mu\text{m}}{w_{slit}}$$

represents the fact that all calibration measurements were taken with 20 μm slit width. During the standard data acquisition procedure, the slit width is usually set to the same value.

Appendix C

Calculation of the Inner Divertor Contribution to the Signal on the Outer Divertor Fibers

In this appendix, the inner divertor contribution to the outer divertor fiber inputs will be calculated, based on the measurement presented in Fig. 6-2. For this calculation, only the reference point in the divertor slot and the data points from the inner divertor surface will be relevant. The following calculations are strictly valid only for the outer divertor fiber A_{bottom} 12 since the measurements on which they are based used that fiber exclusively.

C.1 Quantifying the Reflective Properties of the Divertor Surface

The position of the reference point on the poloidal plane will be denoted by (r_{ref}, z_{ref}), whereas the positions on the inner divertor surface will be referred to by the vectors

$$(r_1, z_1), (r_2, z_2), \ldots, (r_{10}, z_{10}) \ .$$

Given a point (r, z) on the inner divertor surface, the path P will be defined as the linear connection between this inner divertor point and the reference point (r_{ref}, z_{ref}) on

the poloidal plane. We will define β to be the *clockwise* angle between the horizontal radial axis and the linear path P in the same poloidal plane:

$$\beta = \arctan \left| \frac{z - z_{ref}}{r - r_{ref}} \right| . \tag{C.1}$$

Using this definition, the path P is uniquely specified by choosing β.

Positioning the light source at the point (r_{ref}, z_{ref}), the power P_{direct} entering the optical system can be expressed as

$$P_{direct} = \frac{1}{4\pi} \epsilon_{source} \frac{V_{source}\, A_{lens}}{{l_{direct}}^2} , \tag{C.2}$$

where V_{source} is the volume of the light source, ϵ_{source} is the emissivity of the light source in units of [J / s m^3], A_{lens} is the acceptance area of the lens in front of the fiber bundle, and l_{direct} is the length of the light path between the lens and the reference point denoted by (r_{ref}, z_{ref}).

Positioning the light source at the point (r_i, z_i); $i \in \{1, \ldots, 10\}$ on the inner divertor surface, the power $P_{reflected,i}$ entering the optical system can be expressed as

$$P_{reflected,i} = \frac{1}{4\pi} \gamma_P \, \epsilon_{source} \frac{V_{source}\, A_{lens}}{{l_{reflected,i}}^2} , \tag{C.3}$$

where $l_{reflected,i}$ is the length of the light path between the lens and the point at the inner divertor; and where γ_P contains the reflective properties of the divertor surface for the specific path P between the reference point and the inner divertor surface point.

The ratio between equations C.2 and C.3 is given by

$$\frac{P_{reflected,i}}{P_{direct}} = \gamma_P \frac{{l_{direct}}^2}{{l_{reflected,i}}^2} . \tag{C.4}$$

The measured numerical values for these ten ratios are given in Fig. 6-2. From the divertor geometry, we know that

$$l_{direct} = 0.335\,\mathrm{m} .$$

The distance between the lens and an inner divertor point used for the reflection measurement is then given by

$$l_{reflected,i} \approx l_{direct} + L_P , \tag{C.5}$$

where L_P denotes the path length between the reference point and the point (r_i, z_i) on the inner divertor surface. It is calculated from

$$L_P = \sqrt{(r_i - r_{ref})^2 + (z_i - z_{ref})^2} \,. \tag{C.6}$$

Both γ_P and L_P are only dependent on the path P.

The angle dependent reflection coefficients can then be calculated from

$$\gamma_P = \frac{P_{reflected,i}}{P_{direct}} \left(\frac{l_{direct} + L_P}{l_{direct}} \right)^2 , \tag{C.7}$$

where P is the linear path connecting the reference point with the point (r_i, z_i) on the inner divertor surface.

Using the unique correspondence between the path P and the angle β, one obtains the two continuous functions

$$\gamma(\beta) \equiv \gamma_P \quad \text{and} \tag{C.8}$$

$$L(\beta) \equiv L_P \tag{C.9}$$

from interpolation in β. The only purpose of performing the reflection measurements was the calculation of the function $\gamma(\beta)$.

C.2 Relative Contributions to the Outer Divertor Fiber Signal

Based on the two functions $\gamma(\beta)$ and $L(\beta)$, it will be possible to make a statement about the origin of the signal on the outer divertor fibers, assuming a homogeneous emissivity throughout the poloidal region where more than 90% of the total H_α emission in the divertor originates.

The power entering the outer divertor fiber due to radiation from the outer divertor can be expressed as

$$P_{outer} = \epsilon_0 \frac{\Delta V_0 \, A_{lens}}{l_{direct}^{\,2}} \,, \tag{C.10}$$

where ϵ_0 is the emissivity in the divertor slot, and ΔV_0 is the divertor slot volume emitting the radiation.

The radiative power entering the outer divertor fiber due to reflected contributions from the inner divertor region can be expressed by the sum

$$P_{inner} = \sum_{P,j} \gamma_P \, \epsilon_{P,j} \, \frac{\Delta V_{P,j} \, A_{lens}}{(l_{direct} + l_{P,j})^2} \; . \tag{C.11}$$

We sum the contributions over 3-dimensional pixels which are identified by the path P on which they lie. The different pixels on the same path P can be distinguished from each other via the index j. All pixels are understood not to exhibit any overlap with any other pixel, and the totality of all pixels is assumed to cover the entire divertor volume which emits radiation into the outer divertor fiber. The variable $l_{P,j}$ denotes the distance between the reference point and the pixel position, $\Delta V_{P,j}$ refers to the pixel volume, and $\epsilon_{P,j}$ denotes the emissivity of the plasma contained in the pixel volume.

The ratio between the equations C.10 and C.11 is given by

$$\frac{P_{inner}}{P_{outer}} = \sum_{P,j} \gamma_P \, \frac{\epsilon_{P,j}}{\epsilon_0} \, \frac{\Delta V_{P,j}}{\Delta V_0} \, \frac{{l_{direct}}^2}{(l_{direct} + l_{P,j})^2} \; . \tag{C.12}$$

Since the plasma regions where more than 90% of the total H_α emission in the divertor originates are assumed to be of homogeneous emissivity, the emissivity ratio in this expression is equal to unity. We will split the volume elements into a product of a poloidal area and a toroidal extent:

$$\Delta V_{P,j} = \Delta A_{poloidal,P,j} \, \Delta l_{toroidal,P,j} \; , \tag{C.13}$$

$$\Delta V_0 = \Delta A_{poloidal,0} \, \Delta l_{toroidal,0} \; . \tag{C.14}$$

The toroidal extent of the plasma cone emitting radiation into the outer divertor fiber increases linearly with the distance from the lens:

$$\Delta l_{toroidal,P,j} = \Delta l_{toroidal,0} \, \frac{l_{direct} + l_{P,j}}{l_{direct}} \; . \tag{C.15}$$

The ratio which we want to calculate can then be expressed by

$$\frac{P_{inner}}{P_{outer}} = \frac{{l_{direct}}^2}{\Delta A_{poloidal,0}} \sum_{P,j} \gamma_P \, \frac{\Delta A_{poloidal,P,j}}{l_{direct} \, (l_{direct} + l_{P,j})} \; . \tag{C.16}$$

The sum over discrete pixels on the poloidal plane will now be transformed into an integral over the polar coordinates β and l. β denotes the angle specifying the path as defined above, and l is the parametrization along the path, in units of [m]. Instead of summing over the paths P, we will integrate over the continuous angle β. The poloidal area elements transform as follows:

$$\Delta A_{poloidal,P,j} \mapsto l\, dl\, d\beta\ . \tag{C.17}$$

This leads to a new expression for the ratio to be calculated:

$$\frac{P_{inner}}{P_{outer}} = \frac{{l_{direct}}^2}{\Delta A_{poloidal,0}} \int_{\beta_{min}}^{\beta_{max}} d\beta\, \gamma(\beta) \int_{L_0}^{L(\beta)} \frac{l\, dl}{l_{direct}(l_{direct}+l)}\ . \tag{C.18}$$

The poloidal area of the inner divertor region appropriate for this calculation is described by the integration limits

$$\beta_{min} = 25^\circ\ ,\ \beta_{max} = 55^\circ\ ,\ \text{ and }\ L_0 = 0.05\,\text{m}.$$

The integral over path length can be carried out analytically.

The final expression for the relative contributions of the inner and outer divertor regions to the signal on an outer divertor fiber is then found to be:

$$\frac{P_{inner}}{P_{outer}} = \frac{{l_{direct}}^2}{\Delta A_{poloidal,0}} \int_{\beta_{min}}^{\beta_{max}} d\beta\, \gamma(\beta) \left(\ln \frac{l_{direct}+L_0}{l_{direct}+L(\beta)} + \frac{L(\beta)-L_0}{l_{direct}} \right)\ . \tag{C.19}$$

The remaining integral over the angle was performed numerically, leading to the value 0.0432. The length l_{direct} is defined above, and the poloidal divertor slot area emitting radiation into the outer divertor fiber is estimated to be $\Delta A_{poloidal,0} \approx 4 \cdot 10^{-4}\,\text{m}^2$. These values result in

$$\frac{P_{inner}}{P_{outer}} \approx 12.1\ . \tag{C.20}$$

Assuming a constant plasma emissivity in the poloidal region where more than 90% of the total H_α emission in the divertor originates, the signal on the outer divertor fibers will be dominated by the reflected radiation originating in inner divertor regions.

Bibliography

[1] R. D. Bengtson, J. Tannich, and P. Kepple. Comparison between Measured and Theoretical Stark-Broadened Profiles of H_6 – H_{12} Emitted from a Low-Density Plasma. *Physical Review A*, 1(2), February 1970.

[2] H. A. Bethe and E. E. Salpeter. *Quantum Mechanics of One- And Two-Electron Atoms.* Springer-Verlag, Berlin · Göttingen · Heidelberg, 1957.

[3] P. R. Bevington. *Data Reduction and Error Analysis for the Physical Sciences.* McGraw-Hill, New York, 1969.

[4] Chromex. *Grating Selection Parameters*, September 1991. Technical Report 3.

[5] Chromex. *250IS Imaging Spectrograph Users Manual*, April 1993. Version 4.10.

[6] O. Forster. *Analysis 3, Integralrechnung im $\mathcal{R}^n$ mit Anwendungen.* Vieweg Verlag, Braunschweig, 3rd edition, 1984.

[7] T. Fujimoto *et al.* New density diagnostic method based on emission line intensity ratio of neutral hydrogen in an ionizing phase plasma. *Nuclear Fusion*, 28(7): 1255 – 1263, 1988.

[8] H. R. Griem. *Spectral Line Broadening by Plasmas.* Academic Press, New York and London, 1974.

[9] D. R. Inglis and E. Teller. Ionic depression of series limits in one-electron spectra. *The Astrophysical Journal*, 90: 439 – 448, 1939.

[10] J. H. Irby *et al.* Two-color interferometer system for Alcator C-Mod. *Review of Scientific Instruments*, 59(8): 1568 – 1570, August 1988.

[11] P. Kepple and H. R. Griem. Improved Stark Profile Calculations for the Hydrogen Lines H_α, H_β, H_γ, and H_δ. *The Physical Review*, 173: 317 – 325, 1968. Ser. 2.

[12] C. Kurz. *Tomography of Light Emission from the Plasma Edge of Alcator C-Mod.* PhD thesis, Massachusetts Institute of Technology, June 1995.

[13] B. LaBombard *et al.* Scaling and transport analysis of divertor conditions on the Alcator C-Mod tokamak. *Physics of Plasmas*, 2(6): 2242 – 2248, June 1995. part 2.

[14] B. Lipschultz. Review of MARFE phenomena in tokamaks. *Journal of Nuclear Materials*, 145 – 147: 15 – 25, 1987.

[15] B. Lipschultz *et al.* MARFE: an edge plasma phenomenon. *Nuclear Fusion*, 24(8): 977 – 988, 1984.

[16] B. Lipschultz *et al.* Dissipative divertor operation in the Alcator C-Mod tokamak. *Journal of Nuclear Materials*, 220 – 222: 50 – 61, 1995.

[17] G. V. Marr. *Plasma Spectroscopy*, chapter X: The Shape and Width of Spectral Lines, pages 244 – 266. Elsevier Publishing Company, Amsterdam – London – New York, 1968.

[18] Nguyen-Hoe, H.-W. Drawin, and L. Herman. Effet d'un champ magnetique uniforme sur les profils des raies de l'hydrogene. *Journal of Quantitative Spectroscopy & Radiative Transfer*, 7: 429 – 474, 1967.

[19] Princeton Instruments. *ST-138 Controller Operations Manual*, April 1993. Version 1, Revision B.

[20] J. J. Sakurai. *Modern Quantum Mechanics.* Addison-Wesley Publishing Company, 1985.

[21] A. R. Striganov and N. S. Sventitskii. *Tables of Spectral Lines of Neutral and Ionized Atoms.* IFI/Plenum Data Corporation, 1968.

[22] D. Véron. *Infrared and Millimeter Waves*, chapter 2: Submillimeter Interferometry of High-Density Plasmas, pages 69 – 135. Academic Press, New York, 1979. K. J. Button, ed.

[23] R. C. Weast, editor. *CRC Handbook of Chemistry and Physics.* CRC Press, 61st edition, 1980 – 1981.

[24] W. L. Wiese. *Plasma Diagnostic Techniques*, chapter 6: Line Broadening, pages 268 – 317. Academic Press, New York, 1965. R. H. Huddlestone and S. L. Leonard, eds.